A Mass Measurement of the Short-lived Halo Nucleus ^{11}Li with the TITAN Penning Trap Spectrometer

by

Mathew Jonathon Smith

B.Sc., The University of York, 2001
M.Sc., The University of British Columbia, 2005

A THESIS SUBMITTED IN PARTIAL FULFILMENT OF
THE REQUIREMENTS FOR THE DEGREE OF

Doctor of Philosophy

in

The Faculty of Graduate Studies

(Physics)

The University Of British Columbia

(Vancouver)

April, 2008

Abstract

New measurements of the masses of the isotopes ^{8,9,11}Li were made using the recently commissioned TITAN Penning trap mass spectrometer at TRIUMF. The measurement of the halo nucleus ^{11}Li represents a new standard in Penning trap mass spectrometry, as it is the shortest lived, $t_{1/2} = 8.8$ ms, isotope ever weighed using this technique. Low energy, $E = 20$ keV, beams of these radioactive isotopes were produced using the ISAC facility. These were subsequently cooled and bunched using a square-wave-driven Radio-Frequency Quadrupole (RFQ) ion guide, which was filled with hydrogen gas. The cooled ion bunches were then passed into a Penning trap where the mass measurements were made.

A description of the RFQ in the ISAC hall is given along with some results from the commissioning of the device. A new set of harmonic deceleration optics is presented which have been successfully used to inject ions into the RFQ. Cooling of lithium ions with high DC efficiencies of 20%, in helium, and 40%, in hydrogen, are shown. Extraction of extremely short ion bunches, 30 ns FWHM, is also demonstrated. Storage times for stable lithium ions in helium and hydrogen were investigated. It was found that lithium ions could be cooled in hydrogen for up to 30 ms without significant losses whereas cooling in helium lead to exponential losses with a half-life of 5.7(1) ms.

The TITAN Penning trap is described and the ^{8,9,11}Li data presented. Final values for the mass excess of $\Delta(^8\text{Li}) = 20945.70(38)$ keV, $\Delta(^9\text{Li}) = 24954.80(60)$ keV and $\Delta(^{11}\text{Li}) = 40728.1(12)$ keV are obtained. The ^{9,11}Li results are then used to obtain a new value for two neutron separation energy of ^{11}Li, $S_{2n} = 369.3(1.3)$ keV. This agrees with the recent measurement from the MISTRAL spectrometer, 376(5) keV, at the two sigma level, but shows over three standard deviations from the most recent atomic mass evaluation, 300(20) keV.

Table of Contents

Appendices

List of Tables

List of Figures

Acknowledgements

I should first like to thank my supervisor, Jens Dilling, for his continued support throughout the work that culminated in this thesis. A number of other TRIUMF staff have also helped with the design and testing of the system. Special thanks to Matthew Pearson, Dave Lunney, Pierre Bricault and Friedhelm Ames.

Next come all the other post docs and graduate students that have worked alongside me to help make this experiment a reality; Joe Vaz, Ryan Ringle, Maxime Brodeur, Vladimir Rijkov, Thomas Brunner (and his friend Ricky), Christian Champagne and Alain Lapierre as well as all the summer students we burnt through along the way.

I should also thank the TRIUMF support staff especially Mel Good for always holding Thomas accountable for the mistakes I made. The electronics group Don Dale, Hubert Hui, Rolf Keitel, Kevin Langton, Mike Leross and Klara Pelzer for always be happy to help. The design office; Stu Austin, Zlatko Bjelic and Dan Rowbotham. Thanks to Rick Baartman for designing the beam line and Mike McDonald, Ray Dube and Tim Stanford for putting it all together. Thanks to ISAC operations for providing the beams.

Finally I should like to thank all those who have provided support outside the lab especially my wife Masumi and my daughter Emiko to whom this thesis is dedicated.

Dedication

To my wife Masumi and my daughter Emiko. Thanks for staying together
long enough for me to finish this thesis.

I don't think having a Ph.D makes any difference.
—Steve Siu

It would have been better if he had done something useful like
being a Doctor or a Lawyer.
—Phyllis Siu

You can't hide in academia your whole life. It is about time
you faced the real world.
—Jane Smith

Opinions are the result of self argument and as most people
can't argue with anybody and especially with themselves,
opinions are bloody awful.
—Dylan Thomas

Chapter 1

Introduction

In 1985 I. Tanihata et al. performed a series of experiments, using radioactive ion beams produced via the process of projectile fragmentation, at the Lawrence Berkley National Laboratory in the USA [1, 45]. These experiments were designed to measure interaction cross sections, the combined cross section for any event that changed either the proton or the neutron number of the incident ions, and were carried out on the known isotopes of Helium, Lithium and Beryllium as they impinged on Beryllium, Carbon and Aluminium targets. It was shown empirically that these measurements could be used to deduce the interaction radii of the nuclei; these in turn were used to find their Root-Mean-Squared (RMS) matter radii using Glauber type calculations [46]. The results of these experiments are shown in figure 1.1. Prior to this experiment it had been observed that nuclear matter had a uniform density and as such the radii of nuclei could be well described by the empirical Fermi model:

$$r = r_0 A^{\frac{1}{3}}, \tag{1.1}$$

where $r_0 \approx 1.2$ fm and A is the mass number of the nucleus. However, the ^{11}Li matter radius was found to be much larger than predicted by this simple model.

The first theoretical explanation for this observation was published a year later by P.G. Hansen and B. Jonson [2]. They suggested that ^{11}Li could be modelled as a two particle system which could be thought of semi-classically as a ^{9}Li core orbited by a di-neutron. The large observed radius of ^{11}Li could then be described by the well known quantum mechanical problem of a particle in a spherically symmetric square well, see figure 1.2. Key to this picture of ^{11}Li was the energy required to remove the di-neutron. This determined how much of the di-neutron's wave-function leaked out of the potential well and hence the amplitude of the RMS matter radius. In the semi-classical picture of this system the di-neutron forms a halo of nuclear matter, hence ^{11}Li is now known as a halo nucleus.

This theoretical picture was validated in 1988 by T. Kobayashi et al., also at the Lawrence Berkley National Laboratory, when they studied the
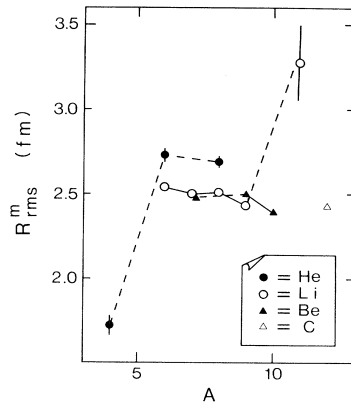
Figure 1.1: The now famous third figure from the 1985 paper by Tanihata et al. [1]. The figure shows the RMS matter radii for the isotopes of Helium, Lithium, Beryllium and Carbon. As shown the RMS matter radius of ^{11}Li is much larger than its neighbouring nuclei.
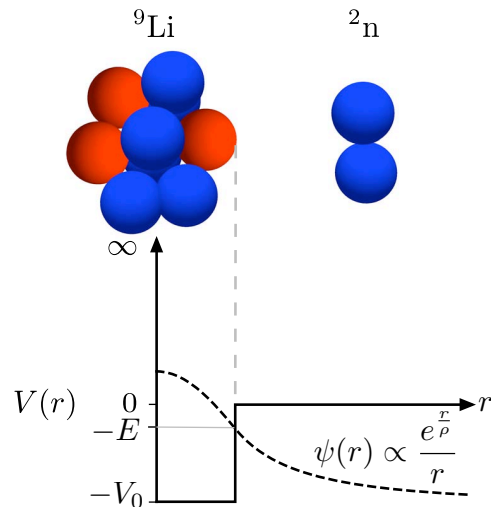
Figure 1.2: A simple model to explain the large observed radius of ^{11}Li as proposed by Hansen and Jonson [2]. The decay length of the wavefunction outside the potential well is given as $\rho = \sqrt{\frac{2\mu|E|}{\hbar^2}}$, where r is the radius of the ^{9}Li core, μ is the reduced mass of the ^{9}Li - ^{2}n system and E is the energy of the bound state.

2

projectile fragmentation of ^{11}Li [47]. It had previously been observed that the transverse momentum distribution of the fragments of stable nuclei had a Gaussian distribution in the projectile's rest frame and that the width of this Gaussian was independent of both the target mass and the projectile beam energy [48]. Such a momentum distribution had been predicted by a number of models and could be considered to arise due to the Fermi motion of the fragments inside the projectile nucleus before fragmentation [49]. The observed transverse momentum distribution for the fragmentation of ^{11}Li is shown in figure 1.3. It is different from that of the stable case in that it has two Gaussian peaks, one wide with a width comparable to fragments from similar mass projectiles and one narrow with a width approximately four times smaller than the first. This can be interpreted by considering the uncertainty principle which relates the width of the momentum distribution Δp to the size of the nucleus Δx, $\Delta p \Delta x \geq \frac{\hbar}{2}$. The narrower Gaussian, in momentum space, corresponds to processes that remove the two loosely bound neutrons which in Hansen and Jonson's simple two body model have a larger spatial extent than the ^{9}Li core. The wider Gaussian thus corresponds to processes involving the ^{9}Li core itself.
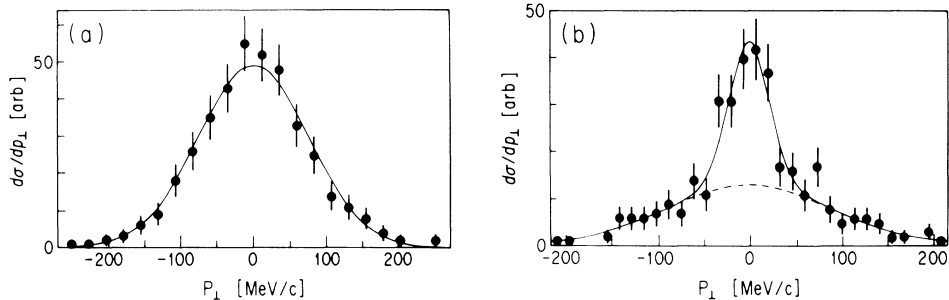
Figure 1.3: Figure 1 from T. Kobayashi et al. showing the transverse momentum distributions of (a) ^{6}He fragments from ^{8}He + C and (b) ^{9}Li fragments from the reaction ^{11}Li + C. As expected the ^{6}He fragments show a Gaussian distribution. However, the ^{9}Li fragments show a double Gaussian suggesting that the ^{11}Li nucleus has two components to its spatial distribution.

A definition of a halo nucleus is one that has a significant proportion in a classically forbidden region due to low nucleon binding energy. Examples have been found of nuclei with one neutron halos e.g. ^{11}Be, two neutron halos e.g. ^{6}He,^{14}Be and ^{17}B and even a four neutron halo, ^{8}He, as well as some candidates for nuclei with proton halos e.g. ^{8}B and ^{13}N. However,

[11]Li remains one of the best studied halo nuclei in part due to its historical significance, but also because it is a relatively simple nuclear system for which high precision few-body calculations can be carried out and because it can be produced cleanly, in relatively large quantities, at both ISOL and projectile fragmentation facilities.

Nuclei with two neutron halos, such as [11]Li, are especially interesting because they form three body systems, e.g. [9]Li + n + n, where none of the composite two body systems, i.e. [9]Li + n and n + n, are themselves stable. Such nuclei were dubbed Borromean by M.Zhukov et al. in a 1993 review paper on the properties of [11]Li and [6]He (see figure 1.4) [50]. A large amount of work, both experimental and theoretical, has been carried out on Borromean nuclei, see e.g. [51, 52] for other reviews on the subject. This is because such nuclei are so weakly bound their properties provide stringent tests for nuclear models.
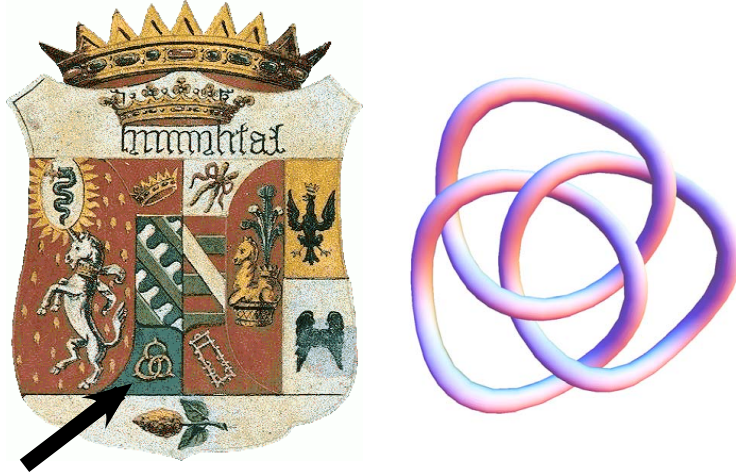
Figure 1.4: The crest of the Borromean family circa 1450 shows a symbol consisting of three interlocked rings (left) and a more modern rendering of these "Borromean" rings (right). The rings are linked together in such a way that removal of any one ring leaves the other two disconnected. This is analogous to the three body system formed by [9]Li + n + n. Together the three body system is stable. However, removal of any one particle leaves the other two unbound.

In this thesis I describe some of the first online measurements made using the TITAN (TRIUMF's Ion Trap system for Atomic and Nuclear science) Penning trap mass spectrometer; the masses of some isotopes of Lithium including ^{11}Li and ^{9}Li. These masses in turn can be used to calculate the binding energy of the ^{11}Li two neutron halo (see section 1.1). In its final configuration the spectrometer will use a total of four ion traps (see chapter 2) in order to carry out high accuracy ($\delta m/m \approx 1 \times 10^{-8}$) mass measurements on the short-lived ($t_{\frac{1}{2}} < 50$ ms) radioactive ions produced by the ISAC (Isotope Separator and ACcelerator) facility at TRIUMF (TRI-University Meson Facility) in Vancouver, Canada. The work of this thesis used only two of the four traps namely the RFQ (Radio-Frequency Quadrupole) and the precision Penning trap, the development of the first of which has been my primary responsibility during my time working on the TITAN project. I will also give results from the online and off-line testing of this device as a continuation of the work in my Master's thesis which described the design and simulation of the RFQ [53]. However, in this first chapter I will review the motivation for the measurement of the mass of ^{11}Li itself.

1.1 Previous Measurements of the ^{11}Li Mass and Good Metrology

There have been previous attempts to measure the mass of ^{11}Li, with two high precision, $\delta m < 50$ keV, results to date. As we saw in the simple two-body model of Hansen and Jonson the size of a Borromean halo nucleus is highly dependent on the energy of the bound state of the last two neutrons, this will also be true for any more sophisticated model. This negative energy, E, is equal but opposite to the two neutron separation energy S_{2n} where:

$$E = -S_{2n} \tag{1.2}$$

$$S_{2n} = M(Z, N-2) + 2M_n - M(Z, N) \tag{1.3}$$

Here Z and N are proton and neutron numbers respectively and M_n is the mass of the neutron. In the case of ^{11}Li the two neutron separation energy depends both on the mass of ^{11}Li and ^{9}Li.

Two neutron separation energies, based on the experimental values for the mass of ^{11}Li, are shown in figure 1.1. The 2003 Atomic Mass Evaluation value for the mass of ^{9}Li has been used which has an uncertainty of 1.935 keV/c^2 [24]. The error bars shown are all predominantly due to the uncertainty in the mass of ^{11}Li. The first measurement by C. Thibault et al. in

1975, made directly using a magnetic mass spectrometer [54], can now be seen to sit below the 2003 AME value and seems to be in poor agreement with all subsequent measurements. The next three measurements, the first carried out directly with a time-of-flight mass spectrometer [55], and the second and third derived indirectly from reaction studies [56, 57], all seem to be in agreement within experimental errors. The latest result by Bachelet et al., measured using the MISTRAL transmission mass spectrometer [25], is in agreement with both Wouters and Kobayashi. However, it shows greater than two sigma deviation from the measurement from Young et al. The 2003 AME value was obtained by taking a weighted average of the results prior to the MISTRAL experiment. Hence, it agrees with the Young et al. result and has an even smaller error bar. The MISTRAL result is 76 eV higher than the AME value i.e. greater than three standard deviations.

Reference	Year	Method	S_{2n} (keV)
Thibault et al. [54]	1975	Mass Spec.	170 ± 80
Wouters et al. [55]	1988	TOF	320 ± 120
Kobayashi et al. [56]	1991	$^{11}\text{B}(\pi^-, \pi^+)^{11}\text{Li}$	340 ± 50
Young et al. [57]	1993	$^{14}\text{C}(^{11}\text{B},^{11}\text{Li})^{14}\text{O}$	295 ± 35
AME 2003 [24]	2003	Mass Evaluation	300 ± 20
Bachelet et al. [25]	2005	Mass Spec.	376 ± 5

Figure 1.5: Values from previous experiments for the two neutron separation energy of ^{11}Li as compared to the 2003 AME value.

This picture is clearly unsatisfactory. The two results with the best precision do not seem to agree with each other suggesting some unknown systematic in either one of them. As such, it is impossible to say from this whether or not either result is really accurate. A second measurement at least on the same level of precision of the MISTRAL experiment, $\delta m \leq 5$ keV/c^2, is clearly desirable. Our first motivation for this new measurement

is thus simply that of good metrology.

1.2 Other Experimental Results that Depend on the Mass of ^{11}Li

There have been recent experiments on ^{11}Li published recently one to measure its charge radius and one to measure the strength of the electric dipole (E1) transition from the ground state. Interpretation of both these experimental results relies on the mass of ^{11}Li.

1.2.1 Measurement of the E1 Transition Strength at RIKEN

Collective motion of the nucleus under the application of an electric dipole excitation has long been know to lead to the so called Giant Dipole Resonance (GDR) at energies of $10 \rightarrow 20$ MeV in typical nuclei. A dipole resonance is also expected in halo nuclei however at lower energies of $1 \rightarrow 2$ MeV, resulting from a slow oscillation of the core against the halo neutrons. This effect is known as a Soft Dipole Resonance (SDR) because it occurs at lower energies than the GDR. A large amount of theoretical work has been carried out on understanding this problem and it has been shown that the E1 excitation spectrum places significant restraints on a number of key properties of ^{11}Li [58–69]. These include correlations between the two halo neutrons, the reaction mechanism between the nucleus and the exciting photon, the effects of shell gap melting and correlations between the neutrons in the ^{9}Li core.

A number of previous attempts had been made to measure the strength of this E1 transition, all of which used the invariant mass spectroscopic method [4–7]. These results all showed strong evidence for an SDR however there was poor agreement between the results as to the exact energy at which it occurred. In invariant mass spectroscopy a beam of ions is fired into a thick target of heavy ions. The ions undergo a Coulomb interaction with the target and can have a E1 transition into an excited state. If the ground state of the incident ion is loosely bound, as in ^{11}Li, the ion will have no bound excited states and so breaks up into a number of outgoing particles. This process is known as Coulomb dissociation. The mass of this unbound excited state is then reconstructed kinematically by careful measurements of the momentum vectors of the incoming and the outgoing particles. This mass is then converted to the relative energy, E_{rel}, of the outgoing particles

which is equal to the excitation energy of the nucleus, E_X, less the energy required to break the nucleus apart. In the case of ^{11}Li the nucleus breaks into three outgoing particles ^{9}Li + n + n and so:

$$E_X = E_{rel} + S_{2n}. \tag{1.4}$$

Experimentally the relative energy of all dissociation events is measured and then processed to give a differential cross section for Coulomb dissociation, $d\sigma_{cd}/dE_{rel}$. The center of mass scattering angle, θ_{cm} is also obtained to give a second differential cross section, $d\sigma_{cd}/d\Omega_{cm}$. These are then combined to give the transition probability, $dB(E1)/dE_{rel}$, using [70]:

$$\frac{d^2\sigma_{cd}}{d\Omega_{cm}dE_{rel}} = \frac{16\pi^3}{9\hbar c}\frac{dN(E_X,\theta_{cm})}{d\Omega_{cm}}\frac{dB(E1)}{dE_{rel}}, \tag{1.5}$$

where $N(E_X,\theta_{cm})$ is the number density of virtual photons produced for a given photon energy and center of mass angle. This quantity can be calculated analytically [71]. However, to use formula 1.5 it is necessary to convert the measured relative energy into an excitation energy using equation 1.4. The final value obtained for the strength of the E1 transition is dependent on the value for S_{2n} and thus the mass of ^{11}Li.

The most recent measurement of the E1 transition strength of ^{11}Li using invariant mass spectrometry was carried out by T. Nakamura et al. at the RIKEN accelerator facility in Tokyo, Japan [3]. This experiment had increased sensitivity at low excitation energies compared to previous attempts due to a novel neutron detection system. By using two walls of plastic scintillators, one behind the other, they were able to eliminate so called cross talk events whereby scattering of a single neutron inside the detector would produce two independent signals. Their final result is shown in figure 1.6 . This result was calculated using the AME value for S_{2n} and gives a energy-integrated B(E1) strength of $1.42 \pm 0.18\,e^2$fm^3. Using the more recent MISTRAL result enhances this value by about 6%.

1.2.2 The ToPLIS Experiment at TRIUMF

A interesting question to consider about ^{11}Li is whether or not the ^{9}Li core can be considered to be completely independent of the two neutron halo. One way this could manifest itself is as a difference between the charge radius of ^{9}Li and that of ^{11}Li. Efforts were made to try and detect a difference through variances in the charge-changing cross sections of ^{9,11}Li [72]. No variance was seen; however, interpretation of the results was dependent
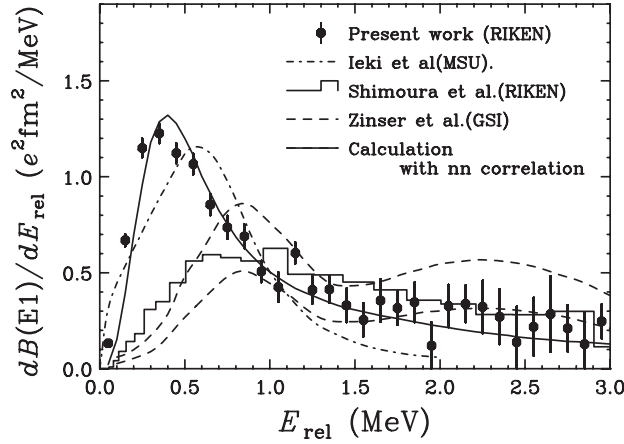
Figure 1.6: The B(E1) distribution as obtained by T. Nakamura et al. (solid circles) [3], compared to the previous measurements at MSU, RIKEN and GSI [4–7]. The distribution shows significant strength at $E_X \approx 0.6$ MeV and is strong evidence for a SDR in ^{11}Li.

on nuclear models. Another experiment was carried out to measure the quadrupole moment of ^{11}Li which was then compared to that of ^{9}Li [73]. This again showed that the core was, "essentially unaffected" by the di-neutron halo. In 2000 Z. -C. Yan and G. W. F. Drake showed that it would be possible to measure the charge radii of light nuclei, in a nuclear model independent way, by looking at isotope shifts [74]. Recently at TRIUMF the Two Photon Lithium Spectroscopy (ToPLiS) experiment determined the charge radius of ^{11}Li using this method [8]. The experiment was sensitive enough to resolve a difference between ^{9}Li and ^{11}Li and hence to discriminate between the results of different nuclear models. However, the interpretation of their results depends on QED and relativistic corrections, a source of uncertainty in which comes from the the mass of ^{11}Li.

An isotope shift, $\delta\nu^{A,A'}$, is the small shift in atomic energy levels caused by adding an extra neutron to a nucleus. This shift has two components [75]:

1. The Mass Shift, $\delta\nu_{MS}^{A,A'}$. The addition of an extra neutron changes the reduced mass of the system which results in the so called normal mass shift, $\delta\nu_{NMS}^{A,A'}$. Correlations in the motions of the electrons can also cause a shift in the center of mass known as the specific mass shift,

$\delta\nu_{SMS}^{A,A'}$. The total mass shift is thus:

$$\delta\nu_{MS}^{A,A'} = \delta\nu_{NMS}^{A,A'} + \delta\nu_{SMS}^{A,A'} = (K_{NMS} + K_{SMS})\frac{M_A - M_{A'}}{M_A M_{A'}}, \quad (1.6)$$

where K_{NMS} and K_{SMS} are known as the coefficients of the normal and the specific mass shift respectively.

2. The Field Shift, $\delta\nu_{FS}^{A,A'}$. The change in the nuclear charge density, caused by the addition of an extra neutron, changes the electrostatic potential that the electrons see, and hence perturbs the atomic energy levels. The magnitude of this shift is proportional to the difference in the mean square charge radii of the two isotopes, $\delta\langle r_c^2\rangle^{A,A'}$.

$$\delta\nu_{FS}^{A,A'} = F\delta\langle r_c^2\rangle^{A,A'}. \quad (1.7)$$

Experimentally the total isotope shift is measured. The value of the mass shift, which is calculated theoretically, is then subtracted from this to yield the field shift. The magnitude of the mass shift can be seen to be approximately proportional to one over the mass of the nucleus squared and thus its influence increases greatly as mass decreases. So, for example, when measuring the isotope shift between ^{208}Bi and ^{209}Bi the mass shift is negligible, whereas, for ^{11}Li the mass shift is approximately $10,000$ times bigger than the field shift. Hence, it must be known very well to extract meaningful information about the field shift from an ^{9}Li $\rightarrow^{11}$Li isotope shift measurement.

The field shift only gives information on the relative difference in charge radius; absolute values for the charge radii can only be found if the radius of one of the isotopes has been measured directly. For stable isotopes it is possible to measure charge radii using elastic electron scattering and this has been done for Lithium, ^{6,7}Li [76]. The ToPLiS collaboration has measured the isotope shifts for ^{6,8,9,11}Li with respect to ^{7}Li [8, 77].

For ^{11}Li the mass shift is calculated by first solving the Schrödinger equation for the three electrons orbiting a point like nucleus. A number of corrections are then applied to account for the finite volume of the nucleus as well as QED and relativistic effects. Calculations of these corrections have been carried out with enough accuracy to allow the mean square charge radii of ^{11}Li to be found from isotope shift measurements, see figure 1.7 [74] [78]. This has shown that there is indeed a difference in the charge radii of ^{9}Li and ^{11}Li and is sensitive enough to discriminate between different nuclear models. However, the mass of ^{11}Li enters into these calculations. The
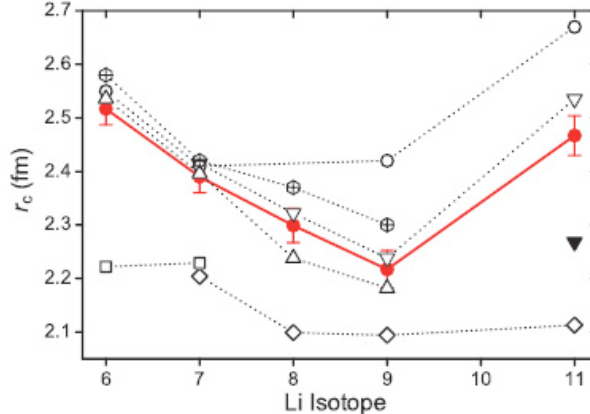
Figure 1.7: The experimental results for the charge radii of some Lithium isotopes as obtained by Sánchez et al. (●) [8]. Theoretical predictions. for these radii from the GFMC model △ [9, 10], the SVMC model with (▼) and without (▽) a frozen core [11, 12], the FMD model (⊕) [13], the DCM model (○) [14] and the NCSM (□,◇) [15, 16]. See section 1.3.3 for a description of some of these calculations

mass shift used by the ToPLis group was calculated using the MISTRAL measurement of the mass of ^{11}Li. The effect of using the AME2003 value for the mass would be to reduce the given value for the ^{11}Li charge radius. In figure 1.7 we see that ToPLiS result for the charge radius sits between two theoretical values calculated using the Stochastic Variation Multi-Cluster Model (SVMC) [11, 12]. In one calculation the core is assumed to be frozen and cannot be excited by the two neutrons, in the second the effects of such excitations are taken into account. The conclusion reached from the data as presented is that the observed charge radius cannot be simply accounted for by correlations between the two neutrons. However, use of the AME value for the ^{11}Li mass value would move the observed radius toward the calculation with the frozen core.

We have now seen two examples of how the mass of ^{11}Li can affect the results of other experiments. In both cases the precision of the MISTRAL ^{11}Li mass measurement is good enough to allow for meaningful comparison between the data and theory, although a measurement with uncertainty on the order of $1\,\mathrm{keV/c^2}$ will be necessary to remove the mass as a significant source of error in the ToPLiS result [79]. A problem arises however due to the inconsistencies in the current status of the mass of ^{11}Li, whereby the

two groups have adopted different values in order to analyse their data. A good test for a nuclear theory would be its ability to reproduce both of these results. However, in order for this to be consistent both the B(E1) and the isotope shift measurements should be reanalysed using the same result for the ^{11}Li mass. Our second motivation for this new measurement is then really the same as our first; good metrology.

1.3 The ^{11}Li Mass and Nuclear Theory

Due to the halo structure of ^{11}Li there has been a large amount of theoretical work carried out in trying to understand this nucleus. A full review of all such theories is well beyond the scope of this thesis. However, it is still instructive to look at the predictions of such models to see if theory can help furnish a clearer picture of the nature of the ^{11}Li two neutron separation energy. Good knowledge of the mass itself can also prove an important test for nuclear theory, and as such it is useful to ask what level of experimental accuracy is needed to differentiate between different models.

1.3.1 Traditional Mass Models

Theoretical nuclear physics is inherently difficult. The scale of the problem ranges from few to many body physics with a large number of effects (e.g. pairing, deformation, shape coexistence) that must be taken into account. With this in mind it seems that trying to find a universal formula that can accurately predict the ground state energies, i.e. the masses, of all the known nuclei, would be a difficult, if not impossible task. However, a number of mass models do exist which work surprisingly well when applied to stable nuclei. It is well known that the predictions of these models do diverge when extrapolated to nuclei far from the valley of stability. A comprehensive guide to different mass models can be found in a recent review article by D. Lunney et al. [80].

The first mass model was that of C. F. Von Weizsäcker [81]. In 1935 he used a liquid drop model to predict the binding energies of all nuclei. Such a model assumes that the nucleus can be modeled as a incompressible fluid with constant density. In the simplest version of this model each nucleon is assumed to feel a constant force from every other nucleon. As every nucleon in the nuclear volume has the same number of neighbours they all feel the same forces and hence have the same binding energy. The total binding energy is then proportional to the number of nucleons, i.e. to the mass number A. However, the nucleons at the surface of the nucleus have fewer

neighbours and are hence less tightly bound. Therefore a term proportional to the surface area, $A^{2/3}$, of the nucleus is then subtracted from the total binding energy:

$$BE = a_V A - a_S A^{2/3}, \qquad (1.8)$$

where a_V and a_S are constants to be determined by fitting the model to experimental data for the binding energies of known nuclei. This simple model can be improved by adding a Coulomb term, a_C, to take into account the reduction in binding energy caused by the electrostatic repulsion between protons in the nucleus, and an asymmetry term, a_A, as nuclei with equal numbers of protons and neutrons appear to be more tightly bound:

$$BE = a_V A - a_S A^{2/3} - a_C \frac{Z^2}{A^{1/3}} - a_A \frac{(A - 2Z)^2}{A} \qquad (1.9)$$

This Weizsäcker equation is a macroscopic mass formula as it ignores microscopic, i.e. quantum mechanical, effects inside the nucleus. As the existence of halo nuclei is a purely quantum mechanical phenomena it is to be expected that such a formula will be unable to predict a sensible value for the binding energy of ^{11}Li.

At the other end of the spectrum of mass models are fully microscopic formulas which use a mean field approach. At the heart of such methods is the variational principle:

$$E_0 = \frac{<\psi_0|H|\psi_0>}{<\psi_0|\psi_0>} \leq E_v = \frac{<\psi_v|H|\psi_v>}{<\psi_v|\psi_v>} \qquad (1.10)$$

This states that the true ground-state energy, E_0, of any Hamiltonian is always less than or equal to the expectation value of the Hamiltonian evaluated with any wavefunction. The equality is only fulfilled when the wavefunction equals the true ground-state wavefunction, ψ_0. Hence, an approximation to the ground state energy of any nuclear system can be found by taking a suitable form for the ground state wavefunction and varying its parameters until a minimum energy is found. A well-known technique for solving this problem was developed by Hartree and Fock in the late 1920s using a trial wavefunction known as a Slater determinant [82–84]. This method assumes that all the nucleons in the nucleus can be treated independently, and that they move in a phenomenological mean-field potential created by the nucleus itself. This kind of approach is computationally very intensive but a mass table has recently been calculated using a zero-range Skyrme interaction using a variant of the Hartree-Fock method, Hartree-Fock-Bogoliubov (HFB), which also includes an effect known as pairing [85–87]. A mass table

has also been produced using a Relativistic Mean Field (RMF) approach where the interaction potential was assumed to arise from relativistic meson exchange between nucleons [88].

Bridging the gap between these two approaches are hybrid microscopic-macroscopic (mic-mac) approaches which start with the liquid drop model and add in extra terms to phenomenologically account for microscopic effects such as pairing and deformation. Such formulas can be quite complicated with a large number of parameters to fit. However, they are still far less computationally intensive than a fully microscopic approach.

It has been observed that the masses of nuclei can be predicted by using algebraic relationships between the known masses of neighboring nuclei. For example in the late sixties Garvey and Kelson developed a number of such relationships, the best known of which is the transverse relation [89]:

$$
\begin{aligned}
M(N+2, Z-2) + M(N, Z-1) - M(N+1, Z-2) \\
- M(N, Z) + M(N+1, Z) - M(N+2, Z-1) = 0
\end{aligned}
\tag{1.11}
$$

These types of relationships result in what are known as local mass formulae because they can only be used to predict the masses of nuclei in the location of other well known masses.

Predictions, for both the mass excess of ^{11}Li and the two neutron separation energy from a number of mass formulas, are shown in figure 1.8. The mass excess, Δ, is defined as the difference between the ions mass in atomic mass units and its mass number. There is quite a large spread in the mass predictions made by the various models, although some seem to make reasonable predictions for the ^{11}Li mass. The predictions for the S_{2n} also show a large spread, approximately $1000 \, \text{keV/c}^2$, with two of the models predicting that the system should be unbound. It is clear that the predictions of these models are not accurate enough to differentiate between the AME value and the MISTRAL result.

1.3.2   Three Body Calculations

Although the simple two-body model of Hansen and Jonson can be used to easily understand how the halo phenomenon arises, it is clearly incomplete. One method to improve this model is to include a more realistic nuclear potential, this also necessitates consideration of the interaction between the two halo neutrons. A two neutron halo nuclei can thus be considered as a three-body system. Such a model in itself is still incomplete as it assumes that the halo neutrons have no effect on the core. However, these models are computationally less intense than the full microscopic models described
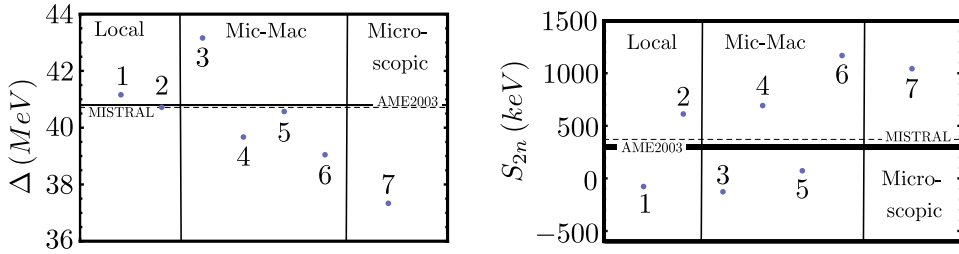
Figure 1.8: Predictions for the mass excess, Δ, and the two neutron separation energy of ^{11}Li due to various mass models. The mass excess is defined as the difference between the actual mass (in atomic mass units) and the mass number of the atom in question. Predictions are taken from 1) E. Comay, I. Kelson and A. Zidon [17], 2) J. Janecke and P. J. Mason [18], 3) H. von Groote et al.[19], 4) H. Koura et al. [20], 5) H. Koura et al. revised [21], 6) J. Duflo and A. P. Zuker [22] and 7) X. Bai and J. Hu [23]. Also shown are the AME2003 [24] (Solid Line) and MISTRAL [25] (Dashed Line) values, the thickness of the lines is representative of the associated error in each.

in the next section, and can be used to make useful predictions about the excitation spectrum and break-up properties of halo nuclei. These properties are essential for understanding the results of experiments such as the invariant mass spectrometry described in section 1.2.1.

A quantum mechanical three body system can be fully described using the Faddeev equations [90]. These equations require the two body interaction potential as an input, and can then be solved iteratively to give the wavefunctions of the three body system. However, because the ^{9}Li core is a composite system the form of the interaction between the core and the halo neutrons is not known. These calculations therefore use phenomenological approximations to the true force which are then adjusted so as to reproduce some of the known experimental properties of ^{11}Li. A number of such calculations have been carried out using different potentials. Results for the two neutron separation energy of ^{11}Li are shown in figure 1.9. Because the two neutron separation energy is an important experimental observable some of the models were actually tuned so as to reproduce it.

The results all seem to show reasonably good agreement with the AME2003 value and could naively be said to favour it, although it is well known that such three body calculations tend to under-bind a system without the inclusion of a three body force. The spread in the calculated values is smaller than the experimental discrepancy between the MISTRAL and the AME2003
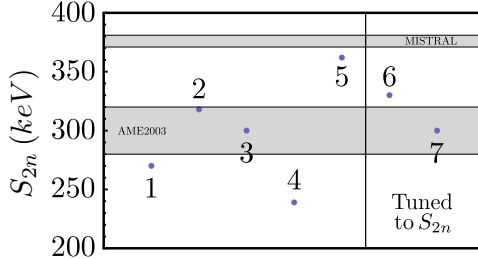
Figure 1.9: Values for the two neutron separation energy of ^{11}Li due to various three-body models. Values are taken from 1) N. Vinh Mau and J. C. Pacheco [26], 2) H. Esbensen et al. [27], 3) A. Cobis et al. [28] , 4) K. Ueta et al. [29], 5) M. A. Khan et al. [30] 6) M. Hesse et al. [31] and 7) E. Garrido et al. [32]. Also shown are the AME2003 [24] and the MISTRAL [25] values for comparison. Models 6 and 7 were tuned so as to try to reproduce experimental values for the two neutron separation energy.

value, therefore a resolution of the current experimental situation is needed to be able to truly differentiate between these different models. The calculation by M. Hesse et al. claims to be tuned so as to reproduce the experimental binding energy with an error of 0.01 MeV. This parameter should presumably be known experimentally to at least this level of accuracy for this claim to be meaningful.

1.3.3 Full Microscopic Calculations

The goal of nuclear physics is to understand nuclear matter and its interactions. The ultimate nuclear theory would use the known theory of the strong force, Quantum ChromoDynamics (QCD), to carry out calculations of nuclear properties from first principles. However, it is currently impossible to carry out such calculations in the non-pertubative limit, i.e. at the low energies associated with nuclear phenomenon.

Traditionally there have been two approaches to solving problems in theoretical nuclear physics. The first, the liquid-drop model (see section 1.3.1), is said to be a fully collective as the nucleus is modeled as a single entity with the individual motion of the composite nucleons ignored. The second, the shell model, assumes the complete opposite. Each nucleon is modeled as an independent particle moving in a mean field created by the nucleus itself. The Hartree-Fock method described in section 1.3.1, is an example of a mean field theory. Quantum mechanically a mean field potential will have

discrete energy levels which the nucleons can occupy. Because nucleons are fermions they cannot all occupy the same eigenstate, so the ground state energy of a nucleus is determined by the filling of the mean field potential.

A true description of nuclear matter lies somewhere between these two extremes. The nucleus is not fully collective, yet nucleon-nucleon interactions cannot be completely ignored. Modifications to the Hartree-Fock theory can be made to try and include some effects of collective motion. A key phenomena that must be accounted for is that of pairing whereby nuclei with an even number of protons or neutrons are systematically more bound than those with an odd number. In the shell model this is understood by two nucleons collectively forming a Cooper pair, analogous to electrons in the BCS (Bardeen, Cooper, and Schrieffer) theory of superconductivity. The resulting boson can then have an energy lower than that allowed for two independent fermions. It is observed that there is no bound state of ^{10}Li, which has a odd number of neutrons, whereas ^{11}Li is bound. The effect of pairing is therefore potentially important in a mean field description of ^{11}Li. There are two well known methods for taking this effect into account inside the framework of the Hartree-Fock method, Hartree-Fock-Bogoliubov and Tamm-Dancoff (a subset of the technique known as the Random Phase Approximation). Both have been applied to ^{11}Li nucleus. Figure 1.10 shows the results of a fully relativistic version of the first method and three calculations using the second method with different potentials. The Tamm-Dancoff calculations all seem to predict a higher two neutron separation energy than the AME2003 whereas the Relativistic-Hartree-Bogoliubov calculation significantly over-binds the system.

The shell model can also be extended to include residual two body interactions between the nucleons, and hence collective behaviour. The No Core Shell Model (NCSM) and the Gamow Shell Model (GSM) are both examples of these kinds of theory. In the NCSM all nucleons are treated as active and calculations are performed on a large but finite basis of harmonic oscillator states. Predictions for the charge radius and two neutron separation energy have been made using this model [15, 16], both of which seem to be in poor agreement with the experimental data. The Gamow shell model works in a basis of Gamow states. This model gives a result that is in perfect agreement with the AME2003 value for the two neutron separation energy of ^{11}Li [37].

With the advent of modern computing a third method for carrying out nuclear calculations has been developed, effective field theory. These ab-initio models attempt to calculate nuclear properties using realistic nucleon-nucleon interactions based on meson exchange. The current state of the
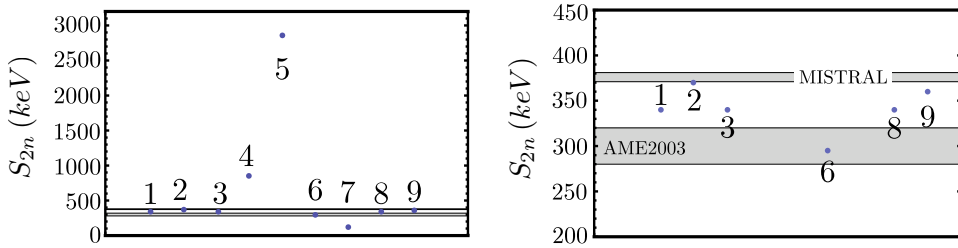
Figure 1.10: Values for the two neutron separation energy of ^{11}Li due to various microscopic models (left). The same data but with the scale adjusted to only show those values that fall close to the AME2003 value (right). These theoretical results were calculated using: 1) Rotating Phase Approximation [33], 2) Tamm-Dancoff with a Gogny Force [34] , 3) Tamm-Dancoff with a δ force [34] , 4) Relativistic-Hartree-Bogoliubov [35, 36], 5) No Core Shell Model [15, 16], 6) Gamow Shell Model [37], 7) Multi-cluster model with a frozen core [11, 12], 8) Multi-cluster model with a dynamic core [11, 12] and 9) Nuclear Field Theory [38]. Also shown are the AME2003 [24] and the MISTRAL [25] values for comparison.

art calculations use the Green's Function Monte Carlo (GFMC) approach where all the protons and neutrons in a nucleus are treated as point particles interacting with realistic two-nucleon and three-nucleon potentials. This method has been successfully implemented for most nuclei with $A < 12$ [9, 10], and results for the charge radii of some isotopes of lithium were shown in figure 1.7. However, this method hasn't been successfully applied to ^{11}Li because of problems arising due to the small value of S_{2n}.

The Stochastic Variational Multi-Cluster Model (SVMC) simplifies the problem further by grouping the nucleons into clusters. ^{9}Li was modeled as a grouping of one alpha particle, one triton particle and two neutrons. ^{11}Li was then modeled as this ^{9}Li core plus an extra two neutrons [11, 12]. The results from this calculation, which seemed to give the best agreement with the ToPLiS measurement of the ^{11}Li charge radius, predict a two neutron separation energy slightly higher than the AME2003 value.

A result has also been published for S_{2n} calculated using so called Nuclear Field Theory (NFT) [38]. This approach solves the nuclear three-body problem in a manner similar to the calculations described in the previous section. However, it also allows for excitations to the ^{9}Li core. This model gives a prediction for the mass that is in good agreement with the MISTRAL result for the ^{11}Li mass.

Figure 1.10 shows the results for S_{2n} calculated with the models described above. Again we see that these models are unable to satisfactorily resolve the current experimental situation. Although some of the calculations make predictions that lie well outside the current experimental uncertainty, most do make predictions that lie between the AME2003 and MISTRAL results. Another mass measurement with at least the same level of precision as the MISTRAL result is therefore required to help differentiate between the results of these models.

1.4 Summary

The motivation for a new measurement of the mass of ^{11}Li with $\delta m < 5\,\text{keV/c}^2$ was presented. It was shown that this measurement is needed to help resolve the current discrepancy between two previous high precision measurements. The impact of the value of the mass on the results of other experiments was also demonstrated. The results from a number of mass models were given along with predictions of the two neutron separation energy from number of nuclear models. These models were not seen to favour one experimental result over the other; rather, good knowledge of the mass would serve as a stringent test for the predictions of these models.

Chapter 2

Penning Trap Mass Spectrometry

We have now seen strong motivation for a new measurement of the mass of
^{11}Li with a precision at least equal to the MISTRAL result, $\delta m = 5 \, \text{keV/c}^2$.
In this thesis I present new measurements of the masses of ^{8,9,11}Li with re-
spect to the well know mass of ^{6}Li [91, 92]. The radioactive lithium ion
beams were produced using the ISAC facility (see appendix B). The beam
was then cooled and bunched using a gas filled Radio-Frequency Quadrupole
(RFQ) before injection into a Penning trap where the measurements were
made. Although it is an important case, it could be argued that the mea-
surement of ^{11}Li is not sufficient justification for the construction of a multi-
million dollar mass spectrometer. In this chapter I present a more general
motivation for building this device at TRIUMF. The principles of Penning
trap mass spectrometry will then be shown followed by a brief review of
other such devices that are already in use around the world today. Finally
a general overview of the TITAN experiment will be given.

2.1 Motivation for High Precision Mass Measurements

2.1.1 Nuclear Structure

One of the most important concepts in nuclear physics is that of binding
energy, B, defined as the difference between the mass of the nucleus and its
constituent parts:

$$B = ZM_H + NM_n - M(Z, N), \tag{2.1}$$

where Z is the number of protons, N the number of neutrons, M_n is the
neutron mass and M_H is the mass of hydrogen. According to Einstein's
famous equation, $E = mc^2$, mass can be considered equivalent to energy
and so this mass difference/binding energy is equal to the energy required

to completely disassemble the nucleus. This energy is dependant on the nature of the strong interaction inside the nucleus. Thus a measurement of one of a nucleus' most fundamental properties, its mass, gives a direct probe of the nuclear Hamiltonian.

One of the big successes of the nuclear shell model, described in section 1.3.3, was an explanation of the so called magic numbers $N = 2, 8, 20, 28,$ $50, 82, 126$. It had been observed that nuclei with magic numbers of either protons or neutrons had a high binding energy compared to that predicted by the semi-empirical mass model. In the shell model these numbers correspond to the numbers of nucleons required to completely fill each shell. The relatively large energy spacing between the shells, or shell gap, then explained the strong binding of the "magic nuclei". One of the key pieces of evidence for the existence of magic numbers were plots of two neutron separation energies versus nucleon number. The magic numbers where shown as sharp breaks from the otherwise smooth trends in these plots.

An open question is that of what happens to these nuclear shells in regions that are far from the so called valley of stability. Evolution of this shell structure is predicted by nuclear models that include such exotic phenomenon as shape co-existance, deformations and variations in the strength of the spin-orbit coupling. One way in which this evolution can be probed experimentally is through measurements of the two-neutron separation energy for unstable nuclei. For example early evidence of shell gap melting for the $N = 20$ magic number was seen in the 1970's by C. Thibault et al. through measurements of the masses of some neutron rich sodium isotopes [54]. Testing predictions for the onset of shell melting and the emergence of new magic numbers continues to be of great importance in nuclear physics and so further mass measurements on short lived-isotopes are required. One proposed set of measurements with the TITAN spectrometer is of the masses of the neutron rich nuclei $^{40-53}$K, $^{51-53}$Ca and $^{51-52}$Sc which will give information about shell effects around the $N = 28$ magic number.

We have already seen the importance of masses in the description of halo nuclei. Alongside ^{11}Li it is also planned to make mass measurements on a number of other halos including ^{19}C, ^{14}Be and the proton halo candidate ^{17}Ne. In addition the mass of the four neutron halo nucleus ^{8}He has already been measured with the spectrometer.

2.1.2 Weak Interaction Physics and Tests of the Standard Model

The Standard Model of particle physics has been enormously successful in describing the interactions of fundamental particles with each other. Apart from recent modifications needed in the neutrino sector every experimental test of the Standard model to date has been in complete agreement with theoretical predictions. One very precise method to test the standard model is to look at the unitarity of the Cabibbo-Kobayashi-Maskawa (CKM) matrix. The matrix links the weak eigenstates of the quarks to their mass eigenstates. In the Standard Model, all matter is composed of twelve basic building blocks known as the fermions. The fermions can be further divided into two groups of six particles, namely the quarks, which feel the strong nuclear force, and the leptons, which do not. The twelve fermions can also be separated into three generations, each with two quarks and two leptons (see table 2.1). The up, charm and top quarks have identical properties except for their masses and so called flavour quantum numbers; the same is true for the down, strange and bottom quarks. The strong and electromagnetic forces are said to conserve flavour, meaning that a quark from one generation cannot decay into a quark from another generation via these types of interaction. However, the weak interaction violates flavour conservation meaning that it is possible for a quark in one generation to decay into a quark of another generation via this interaction. Quantum mechanically the weak interaction has a different basis, the weak eigenstates, than that of the electromagnetic and strong interactions, the mass eigenstates. The CKM matrix describes the mixing of weak and the mass eigenstates [93]:

$$
\begin{pmatrix} d_w \\ s_w \\ b_w \end{pmatrix} = \begin{pmatrix} V_{ud} & V_{us} & V_{ub} \\ V_{cd} & V_{cs} & V_{cb} \\ V_{td} & V_{ts} & V_{tb} \end{pmatrix} \cdot \begin{pmatrix} d_m \\ s_m \\ b_m \end{pmatrix}, \tag{2.2}
$$

where V_{ud} etc are the so called mixing angles between the mass and the weak bases. The Standard Model puts certain constraints on this matrix. One constraint is that the sum of the squares of the elements in any given row should be equal to one. This can easily be understood as the modulus of the square of each of the mixing angles is the probability that one particle will decay to another via the weak interaction *e.g.* $|V_{ud}|^2$ is the probability for a down quark to decay into an up quark. If the Standard Model accounts for all existing quarks we would expect that the sums of the probabilities for the down, strange and bottom quarks to decay into an up quark be equal to one i.e. for $|V_{ud}|^2 + |V_{us}|^2 + |V_{ub}|^2 = 1$.

	Generation 1	Generation 2	Generation 3
Quarks	Up	Charm	Top
	Down	Strange	Bottom
Leptons	Electron	Muon	Tau
	ν_e	ν_μ	ν_τ

Table 2.1: The fermions of the standard model.

Nuclear physics is concerned with systems of protons and neutrons which are themselves composed of up and down quarks. Hence, experimentally the value for V_{ud} can be obtained through studies of nuclear beta decay. The values of the other two terms in the top row of the CKM matrix can be obtained through high energy particle physics experiments; V_{us} is derived from studies of Kaon decays and V_{ub} from the decay of the B meson. Until very recently the experimental result for this sum showed a 2σ deviation from unitarity. However, a recent revaluation of the V_{us} and V_{ud} terms now gives a result that is consistent with unity at the 0.1% level [40]. The re-evaluation of V_{ud} was prompted by recent measurements of the mass of ^{46}V [94, 95].

In the Fermi theory of beta decay the relative strength of a decay is described using the statistical weight function or ft-value, where f is the energy dependant Fermi integral (or phase space factor) and t is the half-life of the decay. In practice f is determined by measuring the Q-value for the decay (i.e. the masses of the parent and daughter nuclei). This ft-value is solely dependent on the nuclear matrix element M_{fi} [96]:

$$ft = \frac{K}{G_F^2 |M_{fi}|^2},$$

(2.3)

where G_F is the weak coupling constant and K is a numerical constant. M_{fi} is dependant on the overlap of the initial and final nuclear wavefunctions.

A superallowed beta decay is defined as one in which the spin-parity of the initial and final state wave function is $J^\pi = 0^+$. In such a process both the spin-parity, J^π, and isospin, I, of the mother and daughter nuclei are the same ($\Delta I = \Delta J = 0$). This means that the total spin of the emitted electron and neutrino must be equal to zero, *i.e.* their spins are aligned anti-parallel. Fermi's original theory of beta decay (1934) only considered the possibility of a vector perturbation to the nuclear hamiltonian, this lead to the selection rule that the total change in spin, ΔJ, must equal zero [97]. In 1936 Gamow and Teller modified Fermi's theory to include the effects of nuclear spin such that $\Delta J = 0, 1$ could be considered where $J = 0 \rightarrow 0$ transitions are not

allowed [98]. This is now understood as the perturbing potential in nuclear beta decay having both a vector and an axial-vector component where the vector component is responsible for the Fermi type transitions ($\Delta J = 0$) and the axial-vector component is responsible for Gamow-Teller type transitions ($\Delta J = 0, 1$ and $J = 0 \nrightarrow 0$). The $0^+ \rightarrow 0^+$ superallowed beta decay is therefore a pure Fermi transition and can be described by considering only the vector component of the weak interaction:

$$ft = \frac{K}{G_V^2 |M_{fi}|^2}. \tag{2.4}$$

The value of V_{ud} can then be extracted by comparing the relative strength, G_V, of the superallowed beta decay with the strength of the weak interaction G_F, which can be obtained through studies of muon decays [99]:

$$G_V = |V_{ud}| G_F. \tag{2.5}$$

In a superallowed decay the initial and final wavefunctions have the same quantum numbers. Thus, the initial and final nuclear states are completely superimposed. If we assume that the nuclear matrix elements are independent of the nuclear composition then the ft-values for all these decays should be the same. This is known as the Conserved Vector Current (CVC) hypothesis. It assumes that there is no coupling between the vector component of the weak interaction and the strong interaction. Thus it is possible to determine V_{ud} by measuring ft-values for a number of superallowed beta emitters.

This theory, however, is not correct in that it assumes that the nuclear matrix elements are completely nucleus independent, which they are not. It is necessary to apply corrections to measured ft-values in order to obtain G_V such that [100]:

$$\mathscr{F}t = ft(1 + \delta_R)(1 - \delta_C) = \frac{K}{G_V^2(1 + \Delta_R^V)|M_{fi}|^2}, \tag{2.6}$$

where δ_R and Δ_R^V are nucleus-dependent and nucleus-independent radiative corrections respectively and δ_C is a charge dependant correction due to isospin symmetry breaking.

$\mathscr{F}t$ values for thirteen $J^\pi = 0^+ \rightarrow 0^+$ transitions have been measured to high accuracy. The results of which are summarized in Figure 2.1 and give the result [40]:

$$\overline{\mathscr{F}t} = 3071.4(8), \tag{2.7}$$

leading to:

$$|V_{ud}| = 0.97418(26) \tag{2.8}$$

These results appear to be in good agreement with each other and provide verification of the CVC hypothesis. When taken with the 2006 particle data group values for $|V_{us}|$ and $|V_{ub}|$ the final result of [40, 101]:

$$|V_{ud}|^2 + |V_{us}|^2 + |V_{ub}|^2 = 1.0000 \pm 0.0011, \tag{2.9}$$

is obtained.
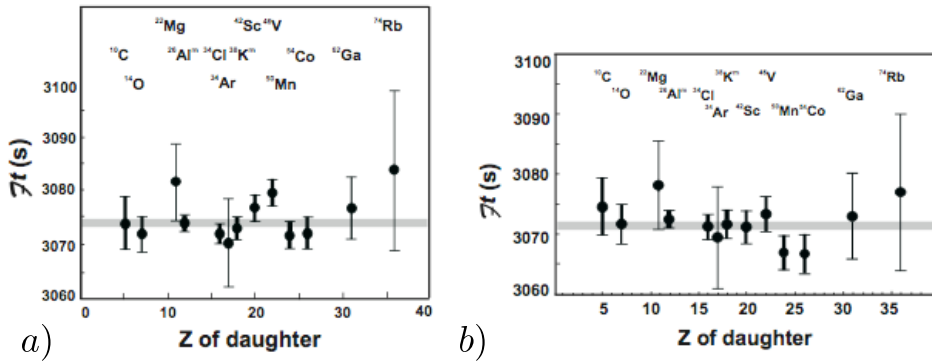
Figure 2.1: a) Corrected $\mathscr{F}t$ values from the 2005 evaluation of V_{ud} [39]. b) Corrected $\mathscr{F}t$ values from the 2007 evaluation of V_{ud} [40]. The 2007 evaluation includes a new mass values for ^{46}V as well as improved calculations for the isospin symmetry breaking corrections, δ_C.

The majority of the error in the value for V_{ud} isn't in fact due to experiment. It instead comes from uncertainties in the calculations of Δ_R^V and δ_C. Although the value of Δ_R^V can only be improved by better understanding of theory, the value of δ_C can be improved with the aid of experiment. This was the case with ^{46}V. The new value of $\mathscr{F}t$ derived from the measurement initially showed a two sigma deviation from the old data. This lead to a re-examination of the calculated δ_C corrections for all the thirteen of the ft values and to the realisation that the calculations had been carried out on too small of a model space. Thus a change in the value of a single mass lead to a complete revision of the calculations of V_{ud}. There are a number of super-allowed beta emitters whose masses are currently not known with the required precision for inclusion in the current evaluation which will be accessible to TITAN e.g. ^{62}Zn and ^{26}Si . There are also a number of cases, e.g. ^{74}Rb and ^{62}Ga, which could potentially be measured with up to

an order of magnitude better precision ($\delta m/m < 1 \times 10^{-8}$) than currently known. Combined with other planned measurements at TRIUMF to obtain even more precise half-life and branching ratio values [102], these masses will help to furnish an even more stringent test of the standard model.

2.1.3 Stellar Processes and Element Nucleosynthesis

Production of all the heavy elements (A $\geq$ 7) take place via nuclear reactions in the stars. In order to understand the complex chains of nuclear reactions that can take place, *e.g.* the *s*-, *p*-, *r*- and the *rp*- processes (for an overview of these processes see [103] or [104]) knowledge of nuclear masses is required.

As an example we consider the *rp*- process whereby nuclei are synthesised by the rapid capture of protons via (p, γ) reactions. This process, which starts with seed nuclei produced during the hot CNO cycle, moves up the proton rich side of the chart of nuclides. The rate of progress of the synthesis is dependant both on the rate of proton capture and on the rate of the inverse process, photo-dissociation. So called waiting points in the process can occur when these two rates are equal but opposite. For the proton capture to continue the waiting point nuclei must β decay to produce a new seed for the process. Because the rate of weak beta decays is much slower than that for proton capture the existence of such waiting points effectively sets the time-scale for this process of nucleosynthesis. A good understanding of the rates of proton capture and photo-dissociation is thus very important for models of these complex reaction chains, especially around the waiting points. In some cases these rates have been measured directly using high energy radio-active ion beams. However, for most nuclei the measurements have not been carried out and so the rates are calculated using either theoretical or experimental values for the proton separation energies. As we shall see in the next section mass models are not always reliable far from stability and so experimentally measured masses are always preferred.

A recently proposed extension to the *rp*- process is the νp- process where the waiting points can be bypassed via fast (n, p) reactions which have the same net effect as a slow β decay [105, 106]. A possible site for this is in the proton rich neutrino driven winds following a core collapse supernova. Here the neutrons required for the (n, p) reactions can be created via the process $p(\overline{\nu}_e, e^+)n$. Recent models of this process showed that it could by-pass the ^{64}Ge waiting point and successfully synthesise the p- nuclei ^{84}Sr, ^{96,98}Ru and ^{102}Pd. These nuclei have long been of interest as no previous model could explain their high relative abundances. However, the model still underproduces the p- nuclei ^{92,94}Mo. At this time it is not known if

this is a true feature of the model or to the poor knowledge of masses in the region of interest. Measurement of the masses of $^{91-93}$Rh and $^{90-92}$Ru can be carried out with TITAN which could greatly influence the predicted production rates in these models.

2.1.4   Mass Models

As we saw in section 1.3.1 a number of models for the prediction of nuclear and atomic masses exist (for a detailed summary see [80]). Such models are needed when experimental results can't be obtained, either because the element under consideration can't be produced in large quantities or because the element has such a short lifetime it is impossible to carry out any kind of precise measurement on it. All of these models give good agreement when applied to nuclei with known masses. However, when using each model to predict the experimentally unknown masses of nuclei close to the proton or neutron drip lines, results are obtained which diverge (see figure 2.2). Extending the range of known masses close to the drip lines, *i.e.* for nuclei with extreme isospin which are usually short-lived, will help to constrain these models and hence improve their accuracy. As an example the masses of the doubly-magic nuclei ^{78}Ni and ^{100}Sn could be measured with TITAN.

2.2   Mass Measurements with a Precision Penning Trap

2.2.1   Penning Trap Principles

Particles that carry electric charge feel forces due to electromagnetic fields. This fact is the underlying principle behind ion traps (devices that use electromagnetic fields to trap charged particles in two or three spatial dimensions). Such traps allow for the study of charged particles in a well defined environment, making them ideal for precision measurements.

There are basically two different kinds of ion trap, both of which have been used to carry out the work described in this thesis:

1. The Penning trap. This trap, developed by Hans Dehmelt on a Penning pressure gauge principle, uses a combination of static electric and magnetic fields in order to confine particles spatially.

2. The Paul trap. This trap provides confinement using electrodynamic fields. It is named after its inventor Wolfgang Paul who along side Hans Dehmelt won the 1989 Nobel prize in physics for their work with
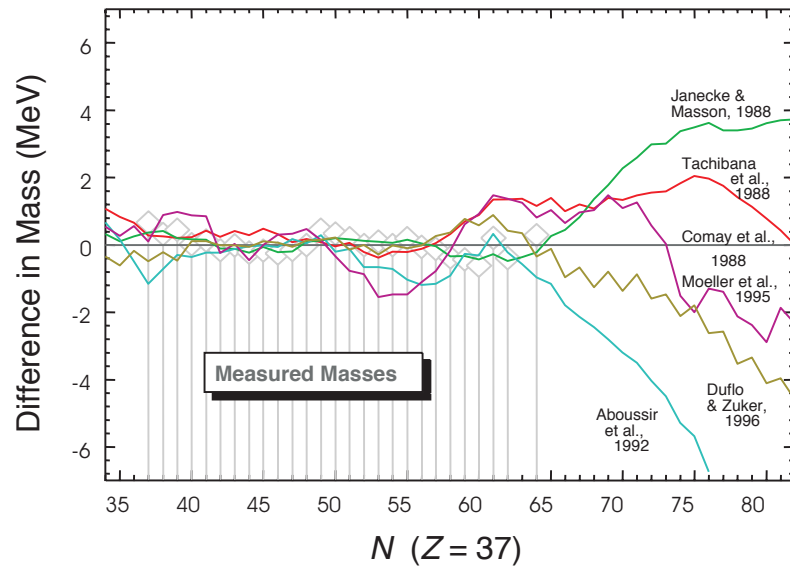
Figure 2.2: Difference in the mass predicted by different theoretical models for the mass of the isotopes of rubidium. For N $\leq$ 64 experimental masses are known and the agreement between models is good, for N > 64 the models diverge. Courtesy of D. Lunney.

ion traps. The RFQ described in the next chapter is an example of
Paul trap.

Consider an ion moving under the influence of a homogeneous magnetic
field with its velocity perpendicular to the magnetic field lines. The Lorentz
force law, $F = q(\vec{E} + \vec{v} \times \vec{B})$, tells us that the ion will feel a force that will
cause it to move on a circular path around the field lines. We can say that
the effect of the homogeneous magnetic field is to confine the ion in the two
dimensional plane perpendicular to the field.
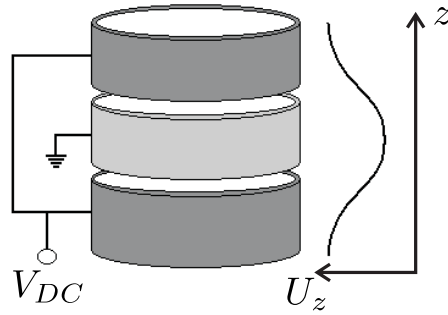
Figure 2.3: A simple cylindrical electrode geometry which can be used to
trap ions in one dimension.

Now consider a singly charged positive ion inside the simple three elec-
trode geometry shown in figure 2.3 with its velocity parallel to the z- axis.
By the application of a positive potential, $+V_{DC}$, to the two end electrodes
a one dimensional potential well can be formed. Positive ions placed at the
center of the trap will be confined along the z- axis as long as their kinetic
energy is less than $+V_{DC}$. This is an example of a simple one dimensional
electrostatic trap. It is possible to imagine any number of electrode geome-
tries that will provide a similar trapping potential, but it is of note that
Gauss' law, $\vec{\nabla} \cdot \vec{E} = 0$, tells us that it is not possible to trap ions in more
than one dimension electrostatically (see figure 2.4).

The Penning trap uses the combination of a magnetic and an electro-
static field to trap ions in all three spatial dimensions. Although the elec-
trode geometry used to provide the necessary electrostatic field is in theory
somewhat arbitrary, in practice it is useful to choose a geometry which pro-
vides a field which can be easily analysed. Modern Penning traps are in
general categorized into two groups:

- Hyperbolic or Precision Penning Traps. These traps use a hyperbolic
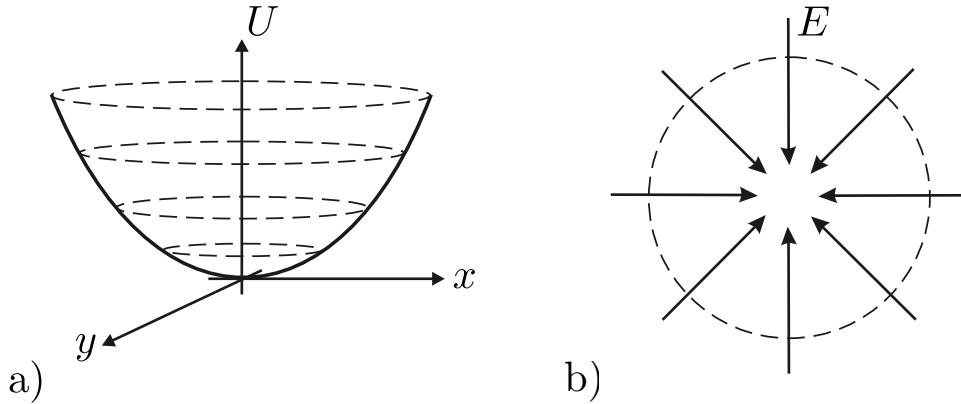
Figure 2.4: A typical two dimensional trapping potential (a) and the corresponding electric field lines (b). In order to obtain such a field it would be necessary to have a charge distribution at the potential minimum, however when trapping ions this is undesirable as the ions will be lost via collisions with the distribution.

electrode configuration to form a harmonic potential such that the electrostatic force exerted on the trapped ions is proportional to the distance from the center of the trap (see figure 2.5). They are used in high precision experiments due to the mathematical simplicity of the fields produced inside.

- Cylindrical or Penning-Malmberg Traps. These traps use some variant on the cylindrical electrode geometry shown in figure 2.3. They offer the advantage that the cylindrical geometry is much easier to machine than the electrodes of the hyperbolic trap. The harmonic fields of the hyperbolic trap can be recreated by the use of compensation electrodes.

2.2.2   Ion Motion in a Penning Trap

The electrostatic potential produced by an ideal hyperbolic Penning trap can be written in the form [107]:

$$V(z, r) = \frac{V_{DC}}{2d_0^2}(z^2 - \frac{r^2}{2}),$$ (2.10)

where d_0, known as the characteristic length of the trap, is given as:

$$d_0 = \sqrt{\frac{z_0^2}{2} + \frac{r_0^2}{4}},$$ (2.11)
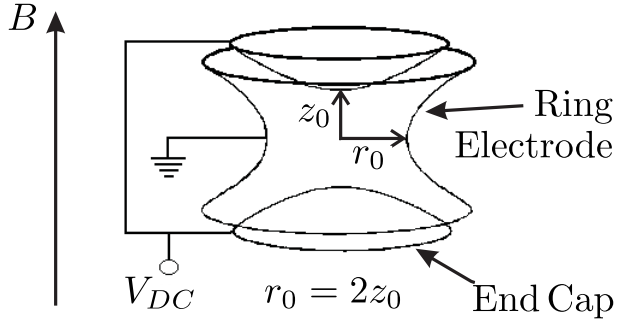
Figure 2.5: This hyperbolic electrode geometry very closely approximates the ideal harmonic potential along the z- axis.

and r_0, z_0 and V_{DC} are as defined in figure 2.5. Using the Lorentz force law and Newton's second law the equation of motion of an ion in the trap in standard cylindrical co-ordinates is then:

$$F = m\vec{a} = -\frac{qV_{DC}}{d_0^2}(\vec{z} - \frac{\vec{r}}{2}) - qB\dot{\vec{r}} \times \hat{z}, \qquad (2.12)$$

where B is the magnetic field strength. This can be separated into axial and radial parts:

$$\ddot{z} = -\frac{qV_{DC}}{md_0^2}z, \qquad (2.13)$$

$$\ddot{\vec{r}} = \frac{qV_{DC}}{2md_0^2}\vec{r} - \frac{qB}{m}\dot{\vec{r}} \times \hat{z}. \qquad (2.14)$$

The axial equation of motion is simply that of an ion in a simple harmonic potential oscillating with frequency:

$$\omega_z = \sqrt{\frac{qV_{DC}}{md_0^2}}. \qquad (2.15)$$

The cyclotron frequency of an ion in a homogeneous magnetic field is given as:

$$\omega_c = \frac{q}{m} \cdot B. \qquad (2.16)$$

Using equation 2.15 and 2.16 we can re-write the radial equation of motion as:

$$\ddot{\vec{r}} = \frac{\omega_z^2}{2}\vec{r} + \omega_c\dot{\vec{r}} \times \hat{z}, \qquad (2.17)$$

which can be written as a pair of coupled equations in Cartesian co-ordinates:

$$\ddot{x} - \omega_c \dot{y} - \frac{\omega_z^2}{2} x = 0, \tag{2.18}$$

$$\ddot{y} - \omega_c \dot{x} - \frac{\omega_z^2}{2} y = 0. \tag{2.19}$$

This can be further simplified by introducing the general co-ordinate u where:

$$u = x + iy. \tag{2.20}$$

This can be used to de-couple the equations of motion giving a single equation:

$$\ddot{u} = -i\omega_c \dot{u} + \frac{\omega_z^2}{2} u, \tag{2.21}$$

which can be solved with the ansatz:

$$u \propto \exp\left(-i\omega_\pm t\right). \tag{2.22}$$

This describes a pair of harmonic oscillations with eigen-frequencies:

$$\omega_\pm = \frac{\omega_c}{2} \pm \frac{\omega_c}{2} \sqrt{1 - \frac{2\omega_z^2}{\omega_c^2}}. \tag{2.23}$$

From this we can derive the useful relationships:

$$\omega_c = \omega_+ + \omega_- \tag{2.24}$$

$$\omega_c^2 = \omega_+^2 + \omega_-^2 + \omega_z^2 \tag{2.25}$$

$$\omega_z^2 = 2\omega_+\omega_- \tag{2.26}$$

For typical values of magnetic and electric field strength $\omega_z << \omega_c$, because the axial frequency, ω_z, is proportional to the square root of the charge to mass ratio whereas the cyclotron frequency is directly proportional to the charge to mass ratio. Hence, $\omega_z^2/\omega_c^2 << 1$ and we can take a Taylor series expansion of 2.23 to get:

$$\omega_+ \approx \omega_c - \frac{\omega_z^2}{2\omega_c} \tag{2.27}$$

$$\omega_- \approx \frac{\omega_z^2}{2\omega_c} \tag{2.28}$$

The motion of an ion in a Penning trap is shown in figure 2.6. Alongside the usual fast cyclotron motion of an ion in a magnetic field the ions undergo a

slow oscillatory motion caused by the perpendicular electric and magnetic fields. Equations 2.27 and 2.28 show that the cyclotron frequency is slightly reduced from that of an ion in a pure magnetic field. Hence, ω_+ is known as the reduced cyclotron frequency. The reduction in frequency, ω_-, is known as the magnetron frequency and is equal to the frequency of the slower $\vec{E} \times \vec{B}$ drift motion.
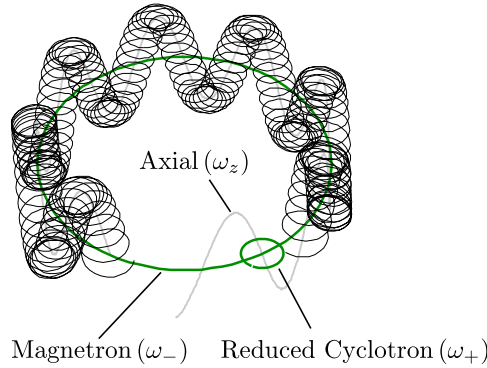
Figure 2.6: The three harmonic eigen-motions of an ion in a Penning trap.

2.2.3   Mass Measurement Techniques

A Penning trap mass measurement involves a determination of the true cyclotron frequency of an ion in the trap:

$$\omega_c = \frac{q}{m} \cdot B. \tag{2.29}$$

This frequency is then combined with the known magnetic field and charge of the ion to give a value for the mass. There exist two well known methods by which the cyclotron frequency of a single ion held in a Penning trap can be measured:

- The Time of Flight (TOF) method [108]. The magnetron and reduced cyclotron motions of an ion in a Penning trap can be coupled via the application of a quadrupolar electric potential of maximum amplitude V_{rf}. If the potential is applied on a ring electrode of radius, a, then the field has components [109]:

$$E_x = \frac{2V_{\mathrm{rf}}}{a} \; y \; \cos(\omega_{\mathrm{rf}} t),$$

$$E_y = \frac{2V_{\mathrm{rf}}}{a} \; x \; \cos(\omega_{\mathrm{rf}} t), \tag{2.30}$$

When applied at the resonance frequency $\omega_{\mathrm{rf}} = \omega_c$ such a field causes an oscillatory conversion of the low radial energy magnetron motion into the high radial energy cyclotron motion and back again, with periodicity T_r, where:

$$T_r = \frac{a^2}{2V_{\mathrm{rf}}} \frac{m}{q} \pi (\omega_+ - \omega_-), \tag{2.31}$$

and m and q are the ion's mass and charge respectively.

If an ion is prepared in a state such that it is initially in a pure low energy magnetron motion and then a quadrupolar field is applied, at the resonant frequency, for a time $T_{\mathrm{rf}} = (2n - 1)T_r$, where n is an integer, then the pure magnetron motion will be converted into a pure reduced cyclotron motion. It can be shown that the radius of the ion's cyclotron motion after the conversion is identical to the radius of the ion's magnetron motion before the conversion [110]. The angular frequency of the reduced cyclotron motion is typically much larger ($\omega_+ \gg \omega_-$) than that of the magnetron motion and as such the ion has a higher radial energy after the conversion. However, if the frequency of the applied quadrupolar field is slightly shifted from that of the resonant frequency the conversion will not be complete and the final radial energy will be less than that for a full conversion.

The radial energy of the ion after the conversion is given as:

$$E_r(\omega_{\mathrm{rf}}) = E_{max} \frac{\sin^2(\frac{\pi}{2}\sqrt{(2\Delta\nu_{\mathrm{rf}}T_{\mathrm{rf}})^2 + 1})}{(2\Delta\nu_{\mathrm{rf}}T_{\mathrm{rf}})^2 + 1}, \tag{2.32}$$

where:

$$\Delta\nu_{\mathrm{rf}} = \frac{\omega_{\mathrm{rf}} - \omega_c}{2\pi}. \tag{2.33}$$

Here, E_{max} is the maximum energy the ion can obtain in the conversion process:

$$E_{max} = \frac{1}{2}m(\rho_-(0)\omega_+)^2, \tag{2.34}$$

where $\rho_-(0)$ is the initial amplitude of the magnetron motion. The form of equation 2.32 is shown in figure 2.7. The function has at peak in radial energy when $\Delta\nu_{\mathrm{rf}} = 0$ as well as a number of side-bands of smaller amplitude symmetric on either side of the resonance. Hence, a measurement of the radial energy as a function of the frequency of the quadrupole excitation can be used to obtain the true cyclotron frequency of the ion and hence its mass.
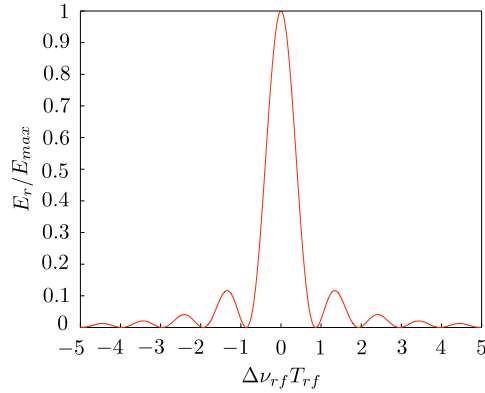
Figure 2.7: Radial energy of an ion in a Penning trap after a quadrupole excitation for a period of time, T_r. The radial energy is a maximum at the resonant frequency, $\Delta\nu_{rf} = 0$. Courtesy of M. Brodeur [41].

Experimentally the radial energy of the ion in a Penning trap can be found by relating it to the time of flight of the ion between the trap and a particle detector placed outside the strong magnetic field. Consider an ion orbiting in a magnetic field oriented in the z- direction with magnetic moment:

$$\vec{\mu} = \frac{E_r}{B_0}\hat{z}, \tag{2.35}$$

where E_r is the radial kinetic energy of the ion and B_0 is the magnetic field strength. If such an ion moves through a magnetic field gradient that is aligned with the z- axis the resulting force in the z- direction is:

$$F_z = -\frac{\mathrm{d}}{\mathrm{d}z}\,\vec{\mu}\cdot\vec{B}(z) = -\frac{E_r}{B_0}\frac{\mathrm{d}B(z))}{\mathrm{d}z}, \tag{2.36}$$

where $B(z)$ is the magnetic field strength along the path of the ion. Hence, we see that the ions radial energy can be converted into longitudinal kinetic energy.

An ion extracted from the trap can be guided to the detector using a series of electrostatic optics. In order to reach the detector the ion must by necessity traverse a strong magnetic field gradient and hence its initial radial energy is converted into longitudinal energy (see figure 2.8). The time taken for the ion to reach the detector can

be calculated as [110]:

$$T(E_r) = \int_{z_0}^{z_1} \sqrt{\frac{m}{2(E_0 - qV(z) - \mu(E_r)B(z))}} \, dz, \qquad (2.37)$$

where E_0 is the initial energy of the ion, q is its charge, $V(z)$ is the electrostatic potential along the ion's path, z_0 is the initial position of the ion and z_1 is the position of the particle detector. Hence, a measurement of the time taken for the ion to reach the detector after extraction from the trap gives a relative measure of its radial energy in the trap and can thus be used to obtain the ion's true cyclotron frequency.
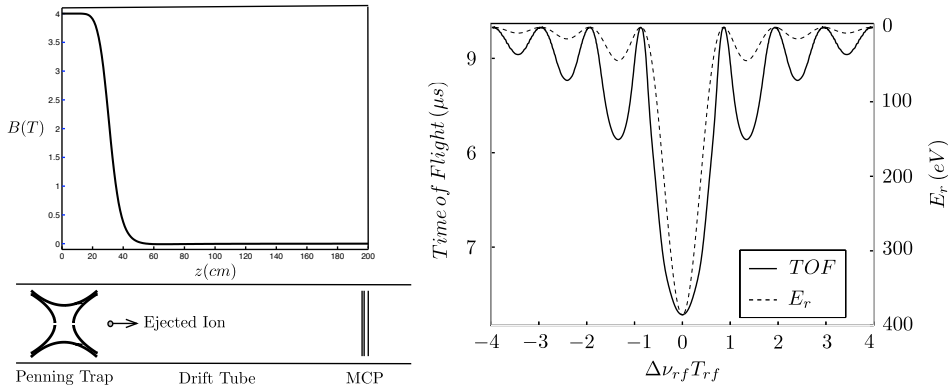
Figure 2.8: The longitudinal magnetic field strength has a strong gradient outside the Penning trap (left). Thus the radial energy of the ions in the trap is converted into longitudinal energy upon extraction. A measurement of the time of flight to an Micro Channel Plate (MCP) detector placed outside the field gradient thus gives a relative measurement of the ions radial energy upon extraction from the trap. Figures courtesy of M. Brodeur [41]

- The Fast Fourier Transform Ion Cyclotron Resonance (FT-ICR) method. For this non-destructive method the image currents induced in the trapping electrodes are detected when the ions oscillate under the effect of the applied fields (see figure 2.9). The Fast Fourier Transform of the image current yields both ω_z and ω_+ directly and using the fact that [111]:

$$\omega_- = \frac{\omega_z^2}{2\,\omega_+}, \qquad (2.38)$$

the cyclotron frequency can be found. For this method to work accurately it is necessary to use a resonant circuit with a large suppression
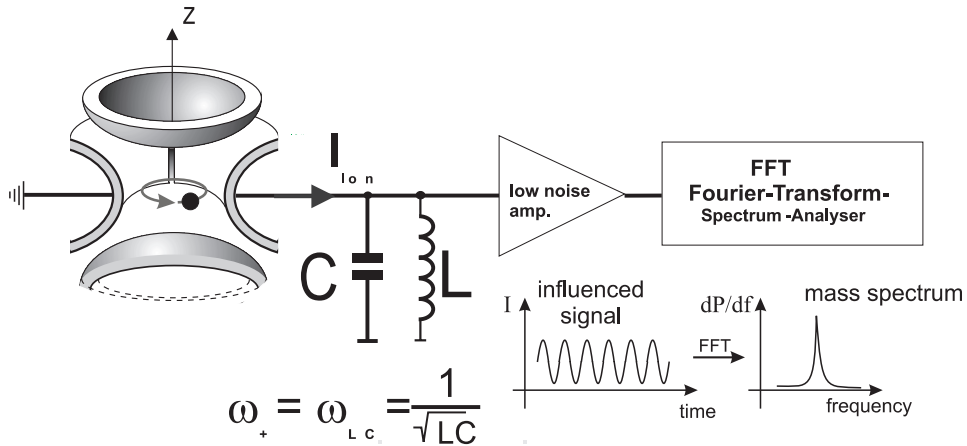
Figure 2.9: A typical setup for the FT-ICR method. The induced signal is passed through a parallel LC circuit, to filter out noise, before it is amplified. The Fourier transform of the signal is then taken. From [42]

of the electronic noise produced by the detection equipment. A long observation time is also desirable as this helps to eliminate the effects of random noise. For this reason this method has thus far only be used to measure the masses of stable particles. All existing on-line Penning trap facilities use the time of flight method to make mass measurements on short lived radio-isotopes (see section 2.3).

2.2.4 Beam Injection and Trapping

There are two well established methods for injecting ions into a trap. The first uses a buffer-gas inside the trap to reduce the longitudinal energy of the injected ions. However, this method is not suitable when making precision measurements which require excellent, $p \approx 1 \times 10^{-9}$ mbar, vacuum inside the trap so as to reduce the effects of collisions with contaminants. With the second method trapping is achieved by dynamic switching of the trap electrodes [112].

A simple dynamic loading scheme is shown in figure 2.10. Dynamic trapping can be used on continuous beams; however it will only trap a small section of the beam, wasting the rest. Therefore it is a requirement for efficient trapping that the ions be delivered to the trap in bunches. Also a requirement for efficient capture is a good overlap between the longitudinal emittance of the injected pulse and the acceptance of the trap. A Penning
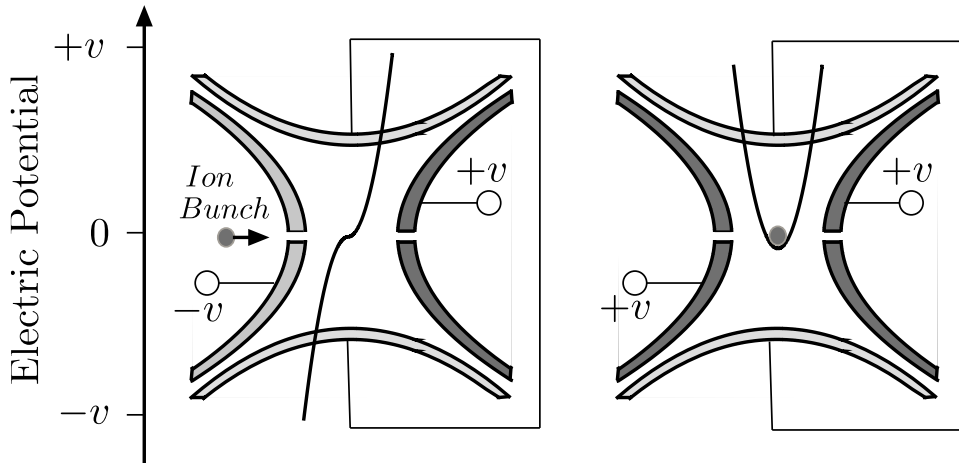
Figure 2.10: In its simplest form dynamic trapping has two steps. First an ion pulse enters the trapping region with one half of the trap potential lowered (left). Second the trapping potential is then raised before the ions can leave the trap (right). A small bunch of ions is thereby contained in the trapping region.

trap is normally operated with a well depth on the order of $1\,\text{to}\,10\,\text{V}$, so to capture one hundred percent of the incident ions the longitudinal energy spread of the beam needs to be lower than the trap depth, i.e. on the order of a few electron volts. The ion pulse also needs to have a time spread that is short compared to the time it would take the pulse to traverse the ion trap. Assuming a typical beam energy of ten electron-volts, and a trap width of $10\,\text{mm}$ this takes on the order of a micro-second. Pulse widths on the order of one hundred nano-seconds or shorter are therefore desirable.

Injection into the trap also places significant constraints on the transverse properties of the incoming ions. In our theoretical description of the time of flight method method we casually assumed that the ions would be injected into the trap in such a way that they would have a finite amplitude magnetron motion and no fast cyclotron motion. In theory this would be achieved by injecting the ions in to the Penning trap exactly along the magnetic field line that passes through the centre of the trap. As the ions have no velocity component perpendicular to the magnetic field they also have no reduced cyclotron motion once trapped. Further, because the electric field gradient on the centre of the trap is zero they have no initial magnetron motion. Once trapped a magnetron motion could then be induced by the

application of an RF dipole excitation at exactly the magnetron frequency. In reality the beam will have some finite emittance that will make this idealised injection scenario impossible. This will cause the ions to pick up some radial energy upon injection into the trap and so start the measurement process with some finite reduced cyclotron and magnetron motions. This is a source of error in the mass measurement and leads to a broadening of the time of flight spectra. Hence, it is always desirable for the ion pulses to have as low of a transverse emittance as possible. For example, simulations of injection of ions into the TITAN Penning trap were recently carried out. It was found that a transverse emittance of $10\,\pi\,\mathrm{mm\,mrad}$, or lower, at an injection energy of $1\,\mathrm{keV}$ would be required to minimise the effects of radial energy pickup [41].

2.3 Facilities for High Precision Mass Spectrometry

Traditionally methods for making precision mass measurements have been classified into two groups; direct and indirect. Indirect techniques make measurements of mass differences between nuclei by looking at either reactions [113] or decays [114, 115]. This can be very useful when looking at very short lived nuclei, e.g. using invariant mass spectrometry (described in section 1.2.1) the masses of particles can be found that are completely unbound. In particular mass spectrometry based on nuclear gamma decay can be extremely precise with resolutions on the order of $1\,\mathrm{eV}$. However, applications of indirect methods are limited as the properties of the other particles involved must also be known to high accuracy.

Direct techniques are somewhat misnomered because no high precision device can measure mass directly. Instead what is measured is either a time of flight or a frequency of revolution as an ion moves under the influence of a magnetic field. This is then compared to that of an ion whose mass is known.

Time of flight spectrometers such as SPEG at GANIL [116], France or the S800 at the NSCL [117], USA can make measurements in as little as $1\,\mu\mathrm{s}$ and are useful for making wide surveys of the masses of very short lived isotopes. However, their resolution is limited with $\delta m/m \approx 1\times 10^{-5}$ typically achievable. In the MISTRAL double turn mass spectrometer ions follow a helical path through a homogeneous magnetic field [118]. The cyclotron frequency of the ions is determined by giving the ions an RF kick at two points in their trajectory. If the kicks are timed correctly the RF field has no

net effect and the ions leave the spectrometer through a pair of narrow slits. If the kicks are miss-timed the ions deviate from the ideal trajectory and do not leave the spectrometer. The spectrometer can make measurements with $\delta m/m \approx 5 \times 10^{-7}$ on low numbers of ions with micro-second half-lives. In a storage ring such as the ESR at GSI, Germany mass measurements with $\delta m/m \approx 1 \times 10^{-6}$ can typically be made by measuring the time of flight around the ring [119]. An order of magnitude improvement in resolution can be made by measuring the orbital frequency in the ring using the Schottky pickup method [120]. However, this requires the ions injected into the ring to be cooled via repeated interaction with cold electrons. This process takes a few seconds making this measurement technique unsuitable for very short-lived ions.

To date the most precise mass measurement have been carried out using Penning traps where accuracies of up to 1×10^{-11} have been reached with stable ions. With radio-active ions accuracies up to $\delta m/m = 8 \times 10^{-9}$ have been achieved. However, unlike the techniques outlined in the previous paragraph these measurements are carried out on very low energy ions, $E \leq 10\,\text{eV}$. Hence the radioactive ions have to be prepared for injection into the Penning trap. Here, we present a quick overview of the other Penning trap systems worldwide.

2.3.1 Off-Line Penning Traps

- MIT ICR. A Penning trap system developed by D. E. Pritchard's group at the Massachusetts Institute for Technology (MIT), and successfully operated for over ten years, it recently relocated to Florida State University [121]. The MIT ICR trap is a cryogenically cooled Penning trap mass spectrometer where ions are created in the trap via the ionization of a neutral gas. The group has developed a system for directly comparing the relative frequencies of two different species of ions in the trap at the same time, one reference mass and one ion of interest, via the FT-ICR method [122]. This allows them to reduce a number of the systematic uncertainties associated with precision traps, most importantly fluctuations in the magnetic field. Mass measurements have been demonstrated with accuracies of $\delta m/m \approx 1 \times 10^{-11}$.

- UW-PTMS. The PTMS (Penning Trap Mass Spectometry) group at the University of Washington uses a cryogenically cooled precision Penning trap in order to make mass measurements via the FT-ICR method [123]. Cooling the trap lowers the pressure inside the trap

to around 1×10^{-18} mbar thus reducing the effects of collisions with contaminants in the trap. This allows them to achieve accuracy of the order of $\delta m/m \approx 1 \times 10^{-10}$.

2.3.2   Penning Traps at Radioactive Beam Facilities

- ISOLTRAP. Radioactive ion beams are created at the ISOLDE facility at CERN, Geneva, via the ISOL (Isotope Separator On-Line) method [124]. The 60 keV ion beam produced is collected in a gas-filled RFQ, then transferred to a gas-filled Penning trap, for isobar separation, before being passed into a 6 Tesla precision Penning trap where the mass measurements are made using the TOF method [125].

  The ISOLTRAP group was the first to show that a Penning trap mass spectrometer could be coupled to externally produced radioactive ions. The system has since been used to measure the masses of over 400 nuclides to an accuracy of around $\delta m/m = 1 \times 10^{-8}$ [126]. Before the measurements presented in this thesis the shortest lived isotope ever measured using a Penning trap was ^{74}Rb with $t_{1/2} = 65$ ms, this mass was measured at ISOLTRAP [127].

- JYFLTRAP. At the cyclotron laboratory of the University of Jyväskylä, Finland, the IGISOL (Ion Guide Isotope Separator On-Line) method is employed in order to produce low energy (40 to 60 keV) heavy ion beams [128]. The quality of these beams is then improved by the use of a gas-filled RFQ before injection into a tandem (isobar separator and precision trap) 7 Tesla Penning trap system for mass measurements. This trap came on-line in 2003 and made its first measurements on some zirconium isotopes ($t_{1/2} \approx 1$ s) with $\delta m/m \leq 5 \times 10^{-7}$ [129]. They have since measured a large number of masses including ^{46}V one of two independent measurements which prompted the re-evaluation of the isospin symmetry breaking corrections to the $\mathscr{F}t$ values described in section 2.1.2 [95].

- SMILETRAP. The SMILETRAP facility, located at the Manne Siegbahn laboratory in Stockholm, uses an EBIS (Electron Beam Ion Source) in order to produce a highly charged beam of stable ions. These are subsequently passed through an analyzing magnet, in order to select a specific charge-to-mass ratio, before injection into a cylindrical Penning trap. The ions are then passed into a hyperbolic Penning trap where mass measurements are made via the TOF method [130].

Measurements have been made on a number of ions with accuracies in the range of $\delta m/m \approx 1 \times 10^{-9}$ to 1×10^{-10}. This group recently published a new result for the masses of ^{6,7}Li with an accuracy of 6×10^{-10} [91].

- SHIPTRAP. Medium to heavy mass radionuclides are produced via fusion-evaporation reactions at the SHIP (Separator for Heavy Ion reaction Products) at GSI Darmstadt with energies of around $100\,\text{keV}/u$ [131]. This beam is then slowed down to thermal energies in a high pressure ($\approx 100\,\text{mbar}$) gas stopping cell, extracted and bunched in an RFQ, before injection into a 7 Tesla tandem Penning trap system. Results of the first on-line measurements were published in 2003 [132]. Recently the masses of some nuclei relevant to calculations of the end points of the rp- process were published [133]. The masses of the heavy nuclei close to the proton drip-line have also been measured [134].

- CPT. The Canadian Penning Trap is currently situated at the Argonne National Laboratory, USA. Beam from the ATLAS accelerator hits a solid target producing high energy recoil products ($E \approx 50\,\text{MeV}/u$) which are then put through an Enge magnetic separator. The beam is decelerated using a gas stopping cell, then cooled and bunched in a gas-filled RFQ, passed through an additional Paul trap for isobar separation before injection into a 6 Tesla precision Penning trap [135]. The masses of around 100 unstable ion species have been measured with a typical precision of $\delta m/m = 1 \times 10^{-8}$ for half-lives as low as 1 s [136]. This group carried out the first Penning trap measurement of ^{46}V showing a deviation from the previously accepted value [94].

- LEBIT. Located at Michigan State University's National Superconducting Cyclotron Laboratory (MSU/NSCL) the LEBIT (Low Energy Beam and Ion Trap) device uses a gas stopping cell in order to thermalize the high energy beam ($E \geq 100\,\text{MeV}/u$) delivered by the A1900 fragment separator [137, 138]. The beam is subsequently extracted from the cell and delivered to a 9.4 Tesla Penning trap system using first a gas filled linear Paul trap for cooling and then a second linear trap where the beam is bunched. This group has recently published the mass of the super-allowed beta emitter ^{38}Ca[139, 140] with $\delta m/m = 8 \times 10^{-9}$, as well as a range of masses relevant to the rp-process [141].

2.4 The TITAN Penning Trap Mass Spectrometer

2.4.1 Overview of the TITAN Experiment

As previously stated the ultimate goal of the TITAN experiment is to carry out high precision mass spectrometry, ($\delta m/m < 1 \times 10^{-8}$), on short-lived ($t_{1/2} \approx 50 \, \text{ms}$) radio-isotopes using a Penning trap [142]. An empirical formula has been proposed which gives an expression for the ultimate possible precision of Penning trap mass measurements as [143]:

$$\frac{\delta m}{m} \simeq \frac{m}{TqBN^{\frac{1}{2}}},$$ (2.39)

where N is the number of ions detected and T is the excitation time for ions in the trap i.e. the amount of time for which the RF excitation is applied, B is the strength of the magnetic field and q is the charge of the ion.
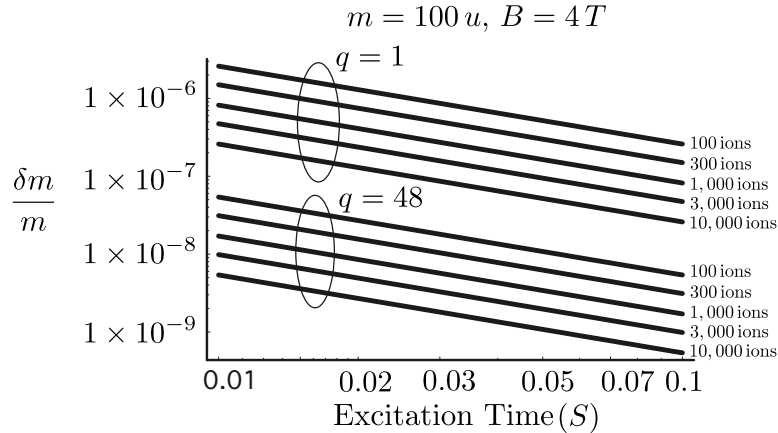
Figure 2.11: Comparison between the precision in mass measurement for singly and highly charged ions in a 4 Tesla Penning trap for given numbers of observed ions.

For stable ions high resolution can be obtained by increasing the excitation time. However, for short-lived ions this is not possible and at present the maximum experimentally achieved resolution is on the order of 8×10^{-9} (see section 2.3). In order to improve this precision one can therefore either increase the number of observations (normally limited by the yield of the

required ion species and the beam time available at on-line facilities), increase the magnetic field strength (technically very difficult beyond around 10 Tesla) or increase the charge state, q, of the ion to be measured (see figure 2.11).

An overview of the stages of the TITAN experiment is shown in figure 2.12. There are two possible modes of operation. In the first the continuous, low energy ($E \leq 60$ keV) ISAC beam is cooled and bunched by the RFQ, then sent directly to a 4 Tesla Penning trap where the mass measurement is made. This method is essentially the same as employed at all other Penning trap facilities. However, there is no trap for isobaric cleaning at TITAN. Although this would initially seem to be a disadvantage as it limits the number of experiments that can be carried out with this simplified set up, it is the removal of this extra stage of beam preparation that makes measurements on extremely short lived isotopes such as ^{11}Li possible.
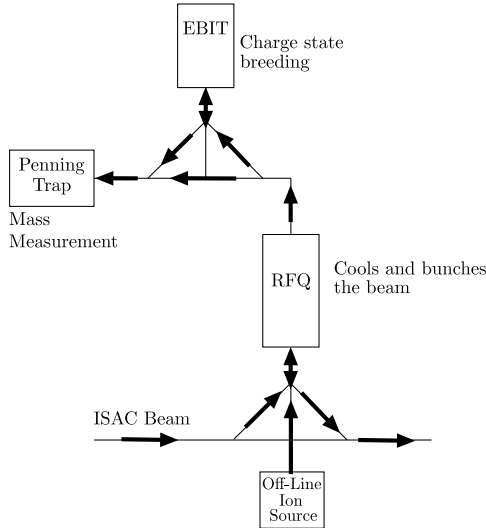
Figure 2.12: Layout of the TITAN experiment with possible beam paths shown as black arrows. Under normal operation the ISAC beam is brought up into the RFQ.

In the second mode of operation the ion bunches from the RFQ are sent to an Electron Beam Ion Trap (EBIT) for charge state breeding before they are sent to the Penning trap [144]. Using this unique combination of RFQ, EBIT and Penning trap TITAN will be able to perform mass spectrometry on highly-charged, short-lived ions for the first time. Equation 2.39 can be used in order to compare the ultimate accuracy possible for mass

measurements at TITAN and those made at other systems (see figure 2.11). For the same number of singly charged ions TITAN's resolution is actually worse than that at other systems due to the lower magnetic field strength. However, for highly charged ions (only available at TITAN) the resolution is much better than that achievable at other facilities.

The measurements presented in this thesis were made using just the RFQ and the Penning trap. At this time the EBIT is still under going off-line commissioning and is not part of the TITAN setup. Because Lithium is so light only a small improvement could be made in the overall accuracy of the measurement by charge state breeding. In the case of ^{11}Li this improvement would be more than offset by the loss of statistics due to radioactive decay during the charge breeding process. This coupled with the excellent yields of ^{11}Li available at ISAC, on the order of $30,000$ ions/s, made ^{11}Li the ideal candidate for commissioning of the spectrometer without the EBIT.

2.5 Summary

Following a general introduction to the motivation for precision mass spectrometry an basic overview of Penning trap theory was given. The time of flight method of Penning trap mass spectrometry was explained alongside methods for capturing ions in a Penning trap. In this context it was seen that the incoming ion pulses need to have short pulse lengths, less than $100\,\mathrm{ns}$, have a small longitudinal energy spread, on the order of $10\,\mathrm{eV}$ and a small transverse emittance, $\epsilon_{99\%} \leq 10\,\pi\,\mathrm{mm}\,\mathrm{mrad}$ at $1\,\mathrm{keV}$. An overview of existing Penning trap facilities was presented alongside a description of the TITAN Penning trap mass spectrometer.

Chapter 3

Off-line Tests of the TITAN RFQ

The role of the Radio-Frequency Quadrupole (RFQ) is to prepare the ISAC beam for injection into the Penning trap. The design and simulation of the RFQ were the subject of my masters thesis [53]. At the time it was written the RFQ was set up on a test stand. The RFQ is now installed in the ISAC hall and the has been tested using off-line ion sources as well as the ISAC beam. The RFQ itself is essentially the same as previously described. However, the injection and extraction optics were completely redesigned for the ISAC installation due to sparking problems at the test stand. In this chapter I will first give an overview of how the RFQ works followed by a description of the experimental set up in the ISAC hall. I will then present some results from the commissioning of the RFQ.

3.1 Buffer Gas Cooling in an RFQ

The purpose of the gas-filled RFQ is to reduce the emittance of an ion beam. The emittance of an ion beam is conserved under the application of conservative forces (see appendix A). However, it is possible to reduce the emittance of an ion beam via the application of non-conservative forces, e.g. by collisions with a buffer gas. Consider an ion beam impinging on an infinitely long chamber filled with a dense gas. The ion beam will lose energy via collisions with the gas, eventually cooling to the ambient temperature of the gas. This process will eventually lead to the loss of the ion beam as the scattering will act so as to thermalize the ions in all three dimensions (ignoring other possible loss processes such as charge exchange). The loss of velocity of the beam in the common direction of motion can be countered via the application of an accelerating electric field. However, this in itself does not necessarily lead to a reduction of the emittance of the ion beam. Although the velocity of the ions perpendicular to the common direction of motion will be reduced via buffer gas damping, seemingly leading to

a reduction in emittance, scattering of the ions forward momentum into the transverse direction acts to counter this effect causing the ion beam to expand radially. This can lead to a net increase of the beam's emittance or worse to the loss of the ion beam. Therefore, in order to reduce an ion beam's emittance via buffer gas cooling it is necessary to provide a force that counteracts the radial expansion. An RFQ can be used to provide such a force making the buffer gas cooling of ion beams possible.

3.1.1 Paul Trap Concepts

As shown in the last chapter it is impossible to trap ions electrostatically in more than one dimension. However, using electrodynamic fields it is possible to create a net focusing force on a charged particle and hence trap in more than one dimension. Consider the standard quadrupolar two dimensional electrode geometry shown in figure 3.1 with positive potential applied to one pair of opposing electrodes and an equal but opposite (negative) potential applied to the other pair of opposing electrodes. A positive ion inside this geometry will feel an attractive force due to the negative electrodes and a repulsive force due to the positive electrodes. This means that it will move toward one of the negative electrodes. If we switch the potentials on the electrodes, before the ion reaches the negative electrode, from positive to negative and vice versa the ion now moves towards one of the newly negative electrodes. By switching the potentials on the rods fast enough we can make it such that the ions never have enough time to reach any given electrode and are effectively trapped. This explanation is slightly simplistic in that it ignores the fact that the applied oscillating field also has the effect of driving the ion motion. However, by proper selection of the properties of the oscillating potential it is possible to trap ions in two dimensions. This kind of trap is known as a two dimensional or linear Paul trap. Due to it quadrupolar structure this kind of trap is also known as an RFQ (RadioFrequency Quadrupole).

The stability of an ions motion in the trap, i.e. whether an ion motion is bound or unbound, depends on the amplitude and frequency of the applied RF field, the RF waveform, the size of the trap and the charge-to-mass ratio of the trapped species. The stability can also be affected by the application of a DC quadrupolar field to the trapping electrodes or, in the case of the square-wave-driven trap, by adjusting the duty cycle of the applied RF [145]. Thus linear Paul traps are commonly used as mass filters [146].

The extension of RF trapping to three dimensions is straight forward. Consider the geometry of the hyperbolic Penning trap. By taking the cross-
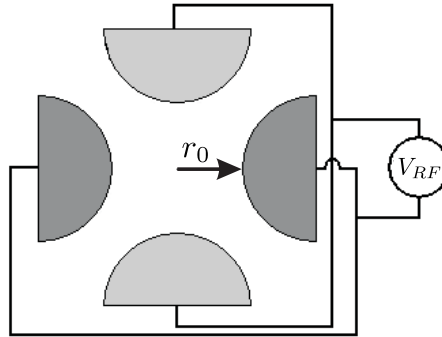
Figure 3.1: Ion can be trapped in two dimensions via the application of RF fields to this quadrupolar electrode geometry.

section of this geometry in a plane parallel to the axial direction of the trap we obtain something similar to the two dimensional quadrupole above, the only difference being the ratio of the axial to the radial dimensions. Hence, by applying RF-fields to the ideal trap geometry we can trap ions in three dimensions. This kind of trap is known simply as a Paul trap.

3.1.2 Digital Ion Traps

RFQ's use four rods driven with an RF potential in order to trap ions in two dimensions. One pair of rods has an applied potential that is 180° out of phase with the potential on the other pair. Traditionally such devices have been driven with a sinusoidally varying RF potential. The potential is generated using an RF amplifier then ferrite cores are used to split the phase of the field before it is applied to the trap electrodes. The leakage inductance of the transformer and the capacitance of the RFQ electrodes then form a LC circuit on the secondary of the transformer.

The stability of an ion's motion in an RFQ is dependent both on the amplitude and the frequency of the applied potential, as well as on the charge-to-mass ratio of the ion. It is desirable to keep the amplitude of the RF as large as possible as this increases the depth of the trapping potential and hence the transfer efficiency of the trap (this is particularly important for radioactive ions because they are difficult to produce). In a traditional RFQ driver the transformer is driven far from the resonant frequency of the LC circuit such that the frequency response is fairly flat in the region of interest. This leads to a large amount of power dissipation in the secondary

circuit and is by no means efficient. This design cannot be used at higher voltages as the power requirements are too severe. Instead the transformer must be run close to the resonant frequency so as to reduce losses in the secondary circuit. Losses can be further reduced by using a high Q, i.e. low bandwidth, resonator. This means that the combination of high voltage and high bandwidth is impossible with a traditional driver.

A square-wave-driven linear Paul trap was first demonstrated by J. A. Richards [145]. Using bipolar junction transistors a square-wave of 80 V maximum peak-to-peak amplitude was generated at frequencies of up to 1 MHz. This was used to drive a small quadrupole for use as a mass filter. The use of square-waves eliminates the need for ferrite cores and as such it is possible to build a broadband trap. More recently the cooling and bunching of ion beams in a square-wave-driven three dimensional Paul trap has been demonstrated by the CPT (Canadian Penning Trap) group at the ANL (Argonne National Laboratory) [147]. Using two fast switching MOSFETs in a push-pull configuration, the group was able to create a square-wave with a peak-to-peak amplitude of 100 V at frequencies of up to 300 kHz. A number of papers have also appeared on the use of digital, three- dimensional ion traps as mass filters from the Shimadzu research laboratory in the UK (see for example [148–150]) where a three-dimensional Paul trap has been driven with 1 kV peak-to-peak amplitudes at up to 1 MHz. The name Digital Ion Trap (DIT) was first introduced by the Shimadzu group. The DIT is so called because digital electronics are used to control the fast switching of the applied square-wave and, in the case of the three-dimensional trap, any other applied RF excitations.

The main limiting factor in square-wave generator design is the energy dissipated in the switching transistors. This energy scales linearly with the capacitance of the driven system. An RFQ cooler and buncher is typically much larger than any previous square-wave-driven system and hence presents a larger capacitive load. For this reason a square-wave-driven RFQ cooler and buncher has been heretofore unrealizable experimentally. However, it was realized that existing technology at TRIUMF developed by the KICKER group, for the MuLan experiment [151], could be adapted in order to make a square-wave generator to drive such a trap. The group had previously developed a method for stacking MOSFETs such that the total energy dissipated in each chip was reduced. Initially the driver was commissioned to operate at $400\,\mathrm{V}_{pp}$ switching at frequencies of up to 1 MHz. A second version of the driver was tested that can switch voltages of up to $600\,\mathrm{V}_{pp}$ at frequencies up to 3 MHz while driving a dummy load. However, this system hasn't been installed in the ISAC hall yet.

3.1.3 Ion Motion in a Digital RFQ

An ion trap works by applying a net force on the ions that pushes them towards the center of the trap. The simplest such force is one that varies linearly with distance from the center of the trap. If we define the center of the trap as $(x, y) = (0, 0)$ with trapping provided in the xy- plane then such a force can be represented as:

$$\vec{F}(x, y) = ax\hat{\boldsymbol{x}} + by\hat{\boldsymbol{y}}, \tag{3.1}$$

where a and b are constants of proportionality. Such a force can be exerted on the ions via the application of an electric field:

$$\vec{E}(x, y) = E_0(\lambda x\hat{\boldsymbol{x}} + \sigma y\hat{\boldsymbol{y}}), \tag{3.2}$$

where E_0, λ and σ are constants governing the strength of the field. Now Gauss' law dictates that:

$$\vec{\nabla} \cdot \vec{E} = 0, \tag{3.3}$$

giving the only non-trivial ($\lambda = \sigma = 0$) physically possible solution:

$$\lambda = -\sigma, \tag{3.4}$$

and as such:

$$\vec{E} = E_0\lambda(x\hat{\boldsymbol{x}} - y\hat{\boldsymbol{y}}). \tag{3.5}$$

This electric field has the corresponding potential:

$$\phi = -\frac{1}{2}E_0\lambda(x^2 - y^2). \tag{3.6}$$

This potential can be generated by a set of four hyperbolic electrodes placed with four-fold symmetry in the xy- plane (see figure 3.2). If a positive bias is applied to one of the opposing pairs of electrodes and a bias equal in magnitude but opposite in polarity is applied to the other pair of opposing electrodes the potential is then:

$$\phi = \frac{\phi_0(x^2 - y^2)}{2r_0^2}, \tag{3.7}$$

where ϕ_0 is the magnitude of the potential difference between adjacent electrodes and r_0 is half the minimum distance between the opposing pairs of electrodes.

Although the potential given by equation 3.7 has the desired effect of focusing linearly in one dimension it also has the undesirable effect of providing
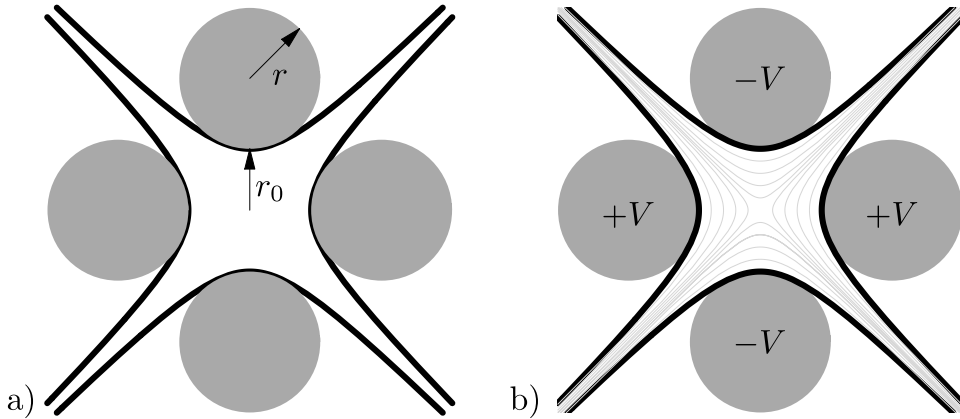
Figure 3.2: a) The ideal hyperbolic structure (black) needed to create the potential given by equation 3.23 can be closely approximated by circular electrodes (gray) where $r = 1.148\,r_0$. b) The equipotential lines generated by such a geometry where $V = \frac{\phi_0}{2}$.

a linear defocusing force in the perpendicular direction. However, it has long been known that by placing a series of quadrupolar devices together, such that the focusing direction of each subsequent section is perpendicular to the previous section, a net focusing force can be obtained [152]. Alteratively, a net focusing force can be provided by applying a time dependent potential to the quadrupolar structure thus forming a linear Paul trap.

Consider the quadrupolar structure driven by an ideal square wave, $S_\delta V$, with angular frequency ω, time period T and duty cycle $\delta = 0.5$ where:

$$S_{0.5} = 1 \qquad 0 < t \leq \frac{T}{2}, \tag{3.8}$$

$$S_{0.5} = -1 \qquad \frac{T}{2} \leq t \leq T, \tag{3.9}$$

and V is the amplitude of the square-wave such that:

$$\phi_0 = 2V. \tag{3.10}$$

The time dependant potential inside the trap is thus:

$$\phi(t) = \frac{S_{0.5}V(x^2 - y^2)}{r_0^2}, \tag{3.11}$$

and the corresponding electric field is:

$$E(t) = -\frac{2S_{0.5}V}{r_0^2}(x\hat{\boldsymbol{x}} - y\hat{\boldsymbol{y}}), \tag{3.12}$$

This gives the equations of motion for an ion in the trap as:

$$m\frac{d^2x}{dt^2} = -Ze\frac{2S_{0.5}V}{r_0^2}x, \tag{3.13}$$

$$m\frac{d^2y}{dt^2} = Ze\frac{2S_{0.5}V}{r_0^2}y, \tag{3.14}$$

$$m\frac{d^2z}{dt^2} = 0. \tag{3.15}$$

Here m is the mass of the ion and Ze is its electric charge. In order to understand the nature of the ions motion inside the RFQ cooler and buncher let us now consider the ions motion with respect to just one of the radial axes. If we let:

$$u = \frac{\omega^2}{4}x, \tag{3.16}$$

$$q = \frac{4ZeV}{m\omega^2 r_0^2}, \tag{3.17}$$

$$h = \sqrt{2q}, \tag{3.18}$$

and:

$$\zeta = \frac{\omega t}{2}, \tag{3.19}$$

then the ion motion inside the trap can be described by:

$$\frac{d^2u}{d\zeta^2} + h^2u = 0 \qquad 0 < \zeta \leq \frac{\pi}{2}, \tag{3.20}$$

$$\frac{d^2u}{d\zeta^2} - h^2u = 0 \qquad \frac{\pi}{2} \leq \zeta \leq \pi. \tag{3.21}$$

The definition of the dimensionless parameter q includes all physical dimensions and fields and it is standard practice to describe the ions motion in a sinusoidally-driven trap in terms of this parameter. Its use in the description of ion motion in a square-wave-driven trap avoids a redefinition of the commonly accepted stability parameter. These equations are known as the Meissner equations after E. Meissner who first used them to study the vibrations of the driving rods in locomotives [153]. They have exact solutions which can most simply be expressed in terms of the transfer matrices:

$$M_+ = \begin{pmatrix} \cos(h\frac{\pi}{2}) & h^{-1}\sin(h\frac{\pi}{2}) \\ -h\sin(h\frac{\pi}{2}) & \cos(h\frac{\pi}{2}) \end{pmatrix}, \tag{3.22}$$

for the period $0 < \zeta \le \frac{\pi}{2}$ and:

$$\boldsymbol{M_-} = \begin{pmatrix} \cosh(h\frac{\pi}{2}) & h^{-1}\sinh(h\frac{\pi}{2}) \\ h\sinh(h\frac{\pi}{2}) & \cosh(h\frac{\pi}{2}) \end{pmatrix}, \qquad (3.23)$$

for the period $\frac{\pi}{2} \le \zeta \le \pi$. So over the period $0 < \zeta \le \pi$ the transfer matrix is:

$$\boldsymbol{M_\pm} = \boldsymbol{M_-} \cdot \boldsymbol{M_+}, \qquad (3.24)$$

where:

$$\begin{pmatrix} u \\ v_u \end{pmatrix}_{\zeta=\pi} = \boldsymbol{M_\pm} \cdot \begin{pmatrix} u \\ v_u \end{pmatrix}_{\zeta=0} \qquad (3.25)$$

Meissner's equations are specific versions of a more general set of equations known as the Hill equations:

$$\frac{d^2u}{d\zeta^2} + \left(\theta_0 + \sum_{r=1}^{\infty} 2\theta_r \cos(2r\zeta) \right) = 0, \qquad (3.26)$$

where in the case of the Meisnner equation $\theta_r = 0$ for $r > 0$. The properties of Hill equations were studied in the 1800's by G. Floquet and it was found that such equations have both stable and unstable solutions [154]. In this case the stable solutions correspond to a net focusing force and the unstable solutions correspond to a net defocusing force on the ion. The stability criterion:

$$|\boldsymbol{Tr(M_\pm)}| < 2, \qquad (3.27)$$

can be used to determine if the ion's motion is bound or unbound [155]. This gives the condition that for a ideal square wave with 50% duty cycle the value of q must be less than 0.712 if an ion's motion is to be stable in the trap. Solutions to the ion's equations of motion for a number of values of q are shown in figure 3.3.

It is a general feature that the stable solutions of a Hill type equation will be of the form:

$$u(t) = \Re\left[A \sum_{n=-\infty}^{\infty} C_n \exp\left[i(n\omega + \omega_s)t\right] \right], \qquad (3.28)$$

where A is a constant depending on the equation's initial conditions. The solution is a Fourier series corresponding to a superposition of an infinite set of frequencies where:

$$\omega_n = |n\omega + \omega_s| \qquad n = 0, \pm1, \pm2..... \qquad (3.29)$$
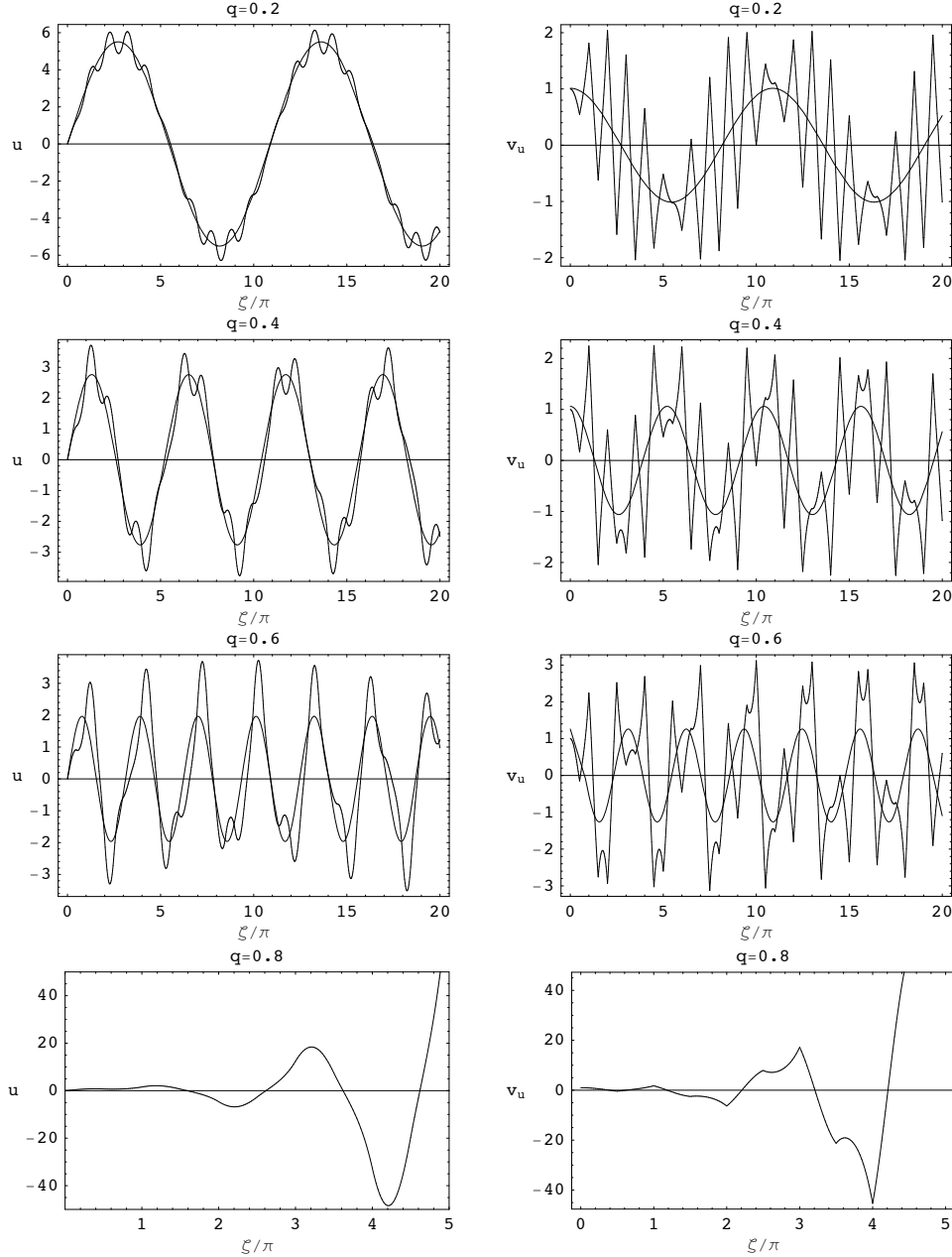
Figure 3.3: Solutions to the Hill equation, with initial conditions $u = 0$ and $v_u = 1$, for given values of q with the pure harmonic macromotion overlayed for comparison. For $q = 0.8$ the motion is unbounded (note the larger scale of the motion) and hence no macromotion solution exists. As the value of q increases so too does the difference between the macromotion and the exact solutions.

The relative amplitudes, C_n, depend on the exact form of the Hill equation, i.e. on the form of the applied potential, but are independent of the equations' initial conditions. The slowest oscillation frequency, ω_s, is known as the secular frequency and is also dependant on the form of the applied potential and independent of the initial conditions. The value of the secular frequency can be calculated as [148]:

$$\beta = \frac{1}{\pi} \arccos\left(\frac{\boldsymbol{Tr(M_\pm)}}{2}\right) = \frac{1}{\pi} \arccos[\cos(\pi\sqrt{q/2})\cosh(\pi\sqrt{q/2})] \quad (3.30)$$

$$\omega_s = \frac{\beta\omega}{2}. \quad (3.31)$$

By observation of the solutions to the Meissner equation we see that the motion describes a slow harmonic motion, known as the macromotion, perturbed by smaller amplitude, higher frequency oscillations, known as the micromotion. If we assume that the ion is moving in a harmonic potential at the secular frequency we can describe the oscillations as:

$$u(\zeta) = A_m \cos(\beta\,\zeta + \alpha), \quad (3.32)$$

where A_m is the amplitude of the secular motion and α describes the phase of the motion both of which can be derived from the ion's initial conditions. Figure 3.3 shows a comparison between the purely secular oscillation and actual solutions to the Meissner equation. It can be seen that at lower q values the motion is very close to that of a particle trapped in a simple harmonic potential well. However, as the value of q rises the amplitudes of the higher frequency oscillations increase perturbing the motion from the ideal harmonic case until, at the critical value of $q = 0.712$, the particle motion becomes unbounded.

Thus, we see that by using a quadrupolar structure driven by a square-wave it is possible to provide a net centering force on the ions that is close to that created by the ideal harmonic potential. Further, by segmenting the rod structure it is also possible to apply DC offsets so as to create a longitudinal potential. If such a device is filled with a buffer gas (see section 3.1.5) it can be used to cool an ion beam. Bunching of the beam can be achieved by applying a longitudinal potential of the form shown in figure 3.4. The cooled ions will collect in the longitudinal potential minimum and are thus trapped three dimensionally. A cooled bunch of ions can be obtained by raising an electrostatic barrier inside the RFQ, *e.g.* at the longitudinal position $z = 600\,\mathrm{mm}$, to stop further incoming ions before they reach the trapping region. The accumulated sample can then be extracted as a bunch by reducing the potential at the end of the RFQ.
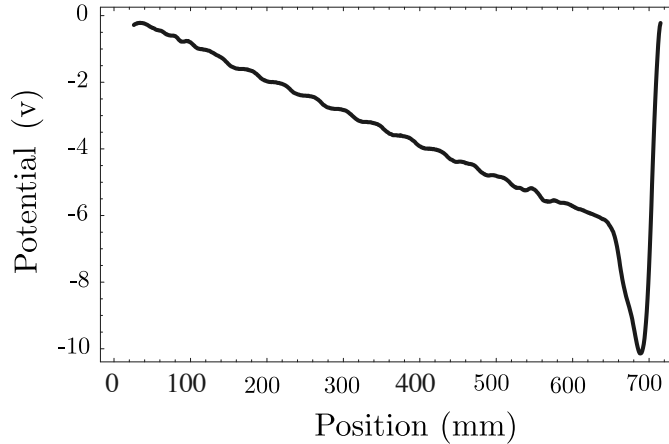
Figure 3.4: Longitudinal potential applied to the RFQ rods extracted from a simulation of the device. The ions drift through the gas under the influence of a weak electric field ($\approx 0.1\,\text{V/cm}$) before being captured in a deep potential well.

3.1.4 Ion Motion in Phase Space

Some important properties of an ion's motion inside an RFQ can be best understood by a study of an ion's motion in position-velocity phase space [156, 157]. First consider an ion undergoing the simple harmonic macro-motion described by equation 3.32. The ion will trace out an ellipse in phase space as shown in figure 3.5. Now consider the motion of an ion in the RFQ as calculated using equations 3.22 and 3.23; this is shown in figure 3.6. It can be seen that at each phase of the RF the ion's motion falls along the circumference of a different ellipse. The effect of the micro-motion is to rotate and stretch the original harmonic ellipse by an amount that is dependant on the phase of the RF whilst conserving its area.

The area of the corresponding harmonic ellipse will be equal to that of any one of the distorted ellipses. This area can be found numerically and hence the amplitude, Am, of the harmonic ellipse can be found using:

$$Area = Am^2 \beta. \tag{3.33}$$

The acceptance of the purely harmonic system can be defined by the ellipse corresponding to a motion with maximum amplitude $r_{\max} = r_0$. As we have seen the effect of the micromotion is to distort this ellipse as a function of phase. To first order the acceptance of the RFQ is defined by
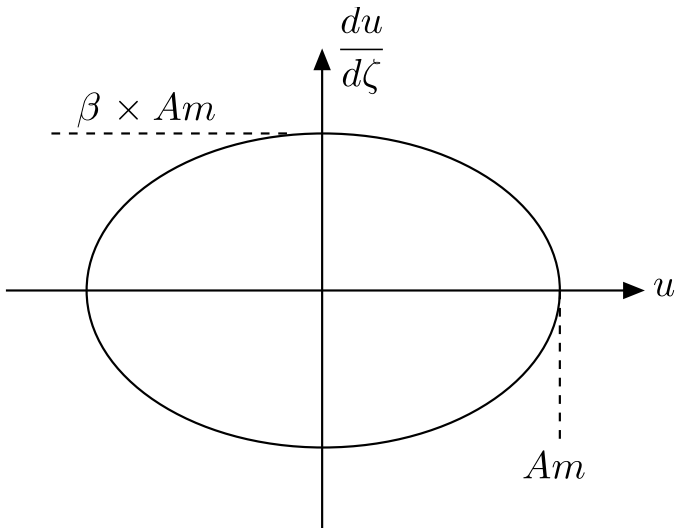
Figure 3.5: A particle undergoing simple harmonic motion as described by equation 3.32 traces out a right ellipse in phase space.
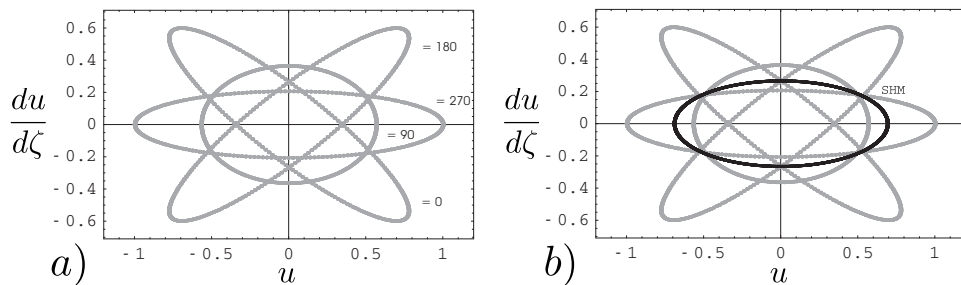
Figure 3.6: a) Distorted harmonic ellipses for different phases of the applied RF- field. A value of 0.4 was taken for q and the ellipses have been scaled such that the maximum positional deviation $= 1$. b) The ellipse of the corresponding pure simple harmonic motion overlayed on the distorted ellipses.

57

the harmonic ellipse whose maximum distorted amplitude $r'_{\max} = r_0$, and is given by:

$$\text{Acceptance} = \omega_s r^2_{\max} = \frac{\beta \omega}{2} r^2_{\max}, \tag{3.34}$$

where ω is the angular frequency of the applied RF and β can be found using equation 3.30. The amplitude $r_{\max}$ of the harmonic ellipse can be found numerically by first converting the dimensions of the ellipses back into the usual SI units and then scaling the ellipses such that $r'_{\max} = r_0$. By rearranging equation 3.16 we can obtain an expression for ω as:

$$\omega = \sqrt{\frac{4ZeV}{mqr_0^2}}, \tag{3.35}$$

hence:

$$\text{Acceptance} = \beta \sqrt{\frac{ZeV}{mqr_0^2}}\, r^2_{\max}. \tag{3.36}$$

The acceptance of TITAN's RFQ is shown in figure 3.7 as a function of q. The results assume an applied peak-to-peak voltage of 400 V, an ion mass of $133\,u$ and a value for $r_0 = 10\,\text{mm}$. As shown in equation 3.36 increasing the value of the applied voltage by a factor of two increases the acceptance by a factor of root two. The maximum acceptance was found to occur at $q \approx 0.32$. Using these concepts we can also calculate the depth of the simple
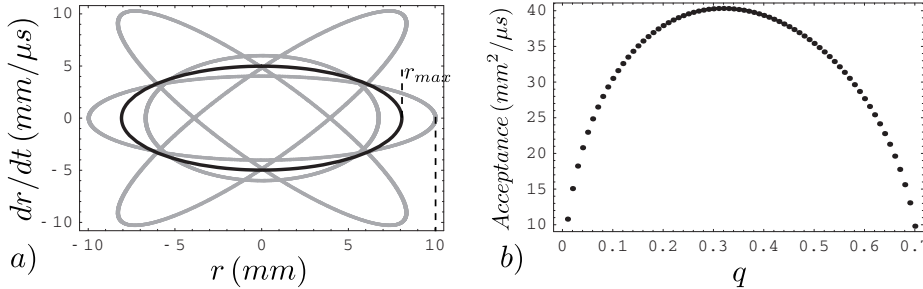
Figure 3.7: a) Distorted harmonic ellipses (gray) and the corresponding purely harmonic ellipse (black) for an ion in TITAN's RFQ operating with $q = 0.3$. The ellipses are scaled such that maximum deviation of the ion from the center of the trap $r'_{\max} = r_0$. b) The acceptance of the trap as a function of q for $V = 200\,\text{V}$.

harmonic potential, sometimes called a pseudo-potential, in the trap:

$$V_{\text{pseudo}} = \frac{1}{2} \frac{m}{Ze} (\omega_s r_{\max})^2 = \frac{1}{2} \frac{\beta^2 V}{qr_0^2} r^2_{max}. \tag{3.37}$$

58

This is shown in figure 3.8 for $V_{pp} = 400$V. It can be seen that the depth of the harmonic potential increases as a function of q until $q \approx 0.5$ when it starts to fall again.
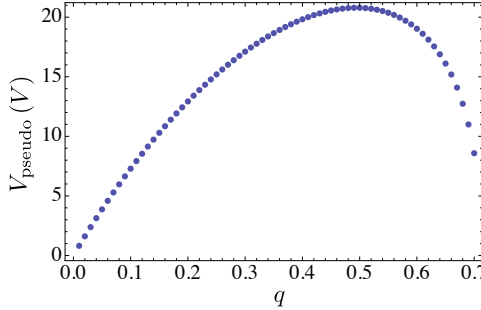
Figure 3.8: Depth of the simple harmonic pseudo-potential in the TITAN RFQ for $V_{pp} = 400$ V

3.1.5 Viscous Damping Model of Ion Beam Cooling

Here we consider a simple model for the cooling of an ion beam inside an RFQ. Although not complete this kind of model is very useful in trying to understand the general properties of such a beam cooler.

Consider a cloud of ions with thermal energy sitting in a chamber filled with an inert buffer gas. Left unperturbed the cloud expands as a function of time via the process of diffusion. If a uniform electric field is applied over the length of the chamber the ion cloud will start to move through the gas. The energy gained from the electric field will be countered by energy lost through collisions with the gas. After some time the average rate of the energy gained and the average rate of the energy lost will reach an equilibrium and the result will be an ion cloud moving through the gas at a fixed average velocity known as the drift velocity, v_d. If the drift velocity is less than the average velocity due to thermal motion of the ions then the diffusion process will remain relatively unaffected by scattering of the ions' net forward momentum into the transverse direction. In this regime the electric field strength is proportional to the drift velocity where the constant of proportionality is known as the mobility, k [158]:

$$v_d = kE. \tag{3.38}$$

If the drift velocity of the ions is significantly higher than the average thermal velocity of the atoms, then scattering of the ions forward momentum into
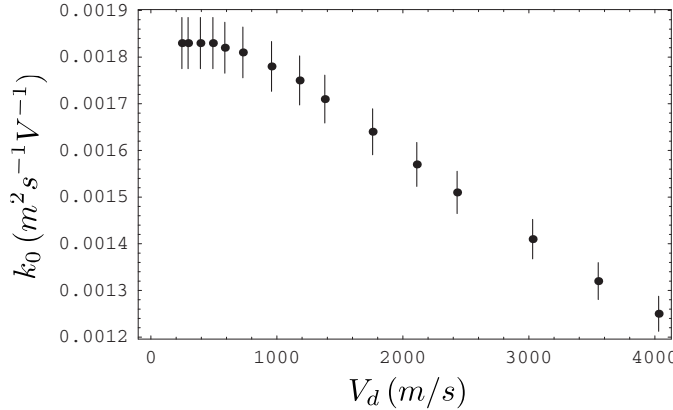
Figure 3.9: Experimental data for the mobility of Cs^+ ions in He [43]. Data exists for drift velocities up to $4030\,\text{m/s}$ corresponding to a kinetic energy of around $10\,\text{eV}$.

the radial plane becomes significant. In this regime the ions mobility is no longer constant but is instead dependent on the ratio of the electric field strength to the number density of the gas, E/N. The drift velocities of ions in a gas can be measured experimentally as a function of E/N and hence the mobility can be found.

As the drift velocity of the ions is a constant the acceleration due to the electric field:

$$a_E = \frac{eE}{m}, \tag{3.39}$$

can be thought of as being countered by an effective deceleration due to the viscous drag caused by the gas:

$$a_d = -\frac{eE}{m} = -\frac{e}{m}\frac{V_d}{k}. \tag{3.40}$$

From the measured values of the drift velocity it is possible to construct a plot of drift velocity versus mobility and a polynomial fit to this data gives an expression for the mobility in terms of the drift velocity. When modelling the motion of an ion through the buffer gas we can assume that its instantaneous velocity is equal to the net drift velocity of an ion cloud and hence we can calculate the drag force on the particle using equation 3.40.

Including the drag force, the equations of motion for particles in a gas

filled cooler and buncher become:

$$m\ddot{x} = -Ze\frac{S_\delta V}{r_0^2}x - e\frac{\dot{x}}{k(\dot{x})}, \tag{3.41}$$

$$m\ddot{y} = Ze\frac{S_\delta V}{r_0^2}y - e\frac{\dot{y}}{k(\dot{y})}, \tag{3.42}$$

$$m\ddot{z} = ZeE_z - e\frac{\dot{z}}{k(\dot{z})}, \tag{3.43}$$

where the damping term should only be applied until the ions reach thermal energies. These equations are not exactly solvable but they can be integrated using numerical techniques. Figure 3.9 shows the experimentally determined ion mobility as a function of the drift velocity for ceasium ions in a helium buffer gas. The data is given in terms of the reduced mobility, k_0, which is the mobility of the ions at standard temperature, $T_0 = 297\,\mathrm{K}$, and pressure, $P_0 = 1\,\mathrm{bar}$. This can be related to the mobility at any given temperature and pressure as:

$$k = k_0\,\frac{T}{T_0}\frac{P_0}{P}. \tag{3.44}$$

As is common with such experimental results no data exists for ions with energies greater than around $10\,\mathrm{eV}$. RFQ coolers typically accept ions with around 5 to $100\,\mathrm{eV}$ energies and as such, data outside the experimental range are needed. One way to obtain such data is via the Monte Carlo method described in my masters thesis [53]. Results for ceasium ions in helium are shown in figure 3.10.

A typical calculation of an ion's trajectory is shown in figure 3.11. Radially the amplitude of the ion's motion is damped by the buffer gas whilst its oscillation frequency remains the same. If the effect of the longitudinal potential is ignored then the average range, R_z of an ion entering the RFQ with velocity v_{int} in the z- direction can be calculated in the gas as:

$$R_z = \frac{m}{e}\int_0^{v_{int}} k(v_z)dv_z, \tag{3.45}$$

and the average cooling time can also be calculated from:

$$t_{\mathrm{cool}} = \frac{m}{e}\int_{v_{\mathrm{therm}}}^{v_{\mathrm{int}}} \frac{k(v_z)}{v_z}dv_z, \tag{3.46}$$

where v_{therm} is the thermal velocity of the cooled ions. Typical results of these calculations are also shown in figure 3.11. Such calculations reveal little about the final properties of a cloud of ions in the gas as they apply
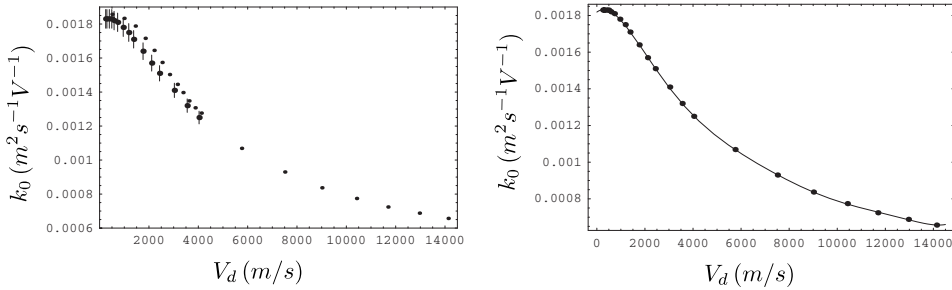
Figure 3.10: a) Comparison of the experimental data for the mobility of Cs^+ ions in he with the values obtained from Monte Carlo simulations. The simulations show some deviations from the experimental results (to be discussed in the following chapter) but reproduce the general trend of the experimental data well. b) A polynomial fit to a combination of the experimental data, at low energies, and the simulated data, at high energies ($V_d > 4030 \, \text{m/s}$), gives an expression for the mobility of Cs^+ in He in the energy range 0 to 150 eV.

the same average damping force to each ion. This means that eventually all the ions end up with the same final energy which is clearly not representative of a physical system.

From the simple considerations above we see that the range of 30 eV ceasium ions in 2.5×10^{-2} mbar of helium, a typical gas pressure achieved in other RFQs currently in operation (see for example [159] or [160]), is around 500 mm and that it takes around 300 μs for the ions to thermalise. Although the cooling time and stopping range will vary with the ions mass, consideration of the variance in experimental ionic mobilities tells us that the ceasium numbers should be around the right order of magnitude for most ions. In fact most of the proposed measurements with the TITAN system are for ions with masses less than ceasium and as such shorter stopping ranges and cooling times can be expected. The TITAN system will be used to make measurements on ions with half-lives in the tens of milliseconds or longer and as such cooling times of around 1 ms are acceptable. The maximum length of the cooler was predetermined by spatial constraints to be 700 mm which fits with the 500 mm stoping range for ceasium. Thus with this simple model we see that cooling of the ISAC beam is indeed possible using a gas filled RFQ.

63
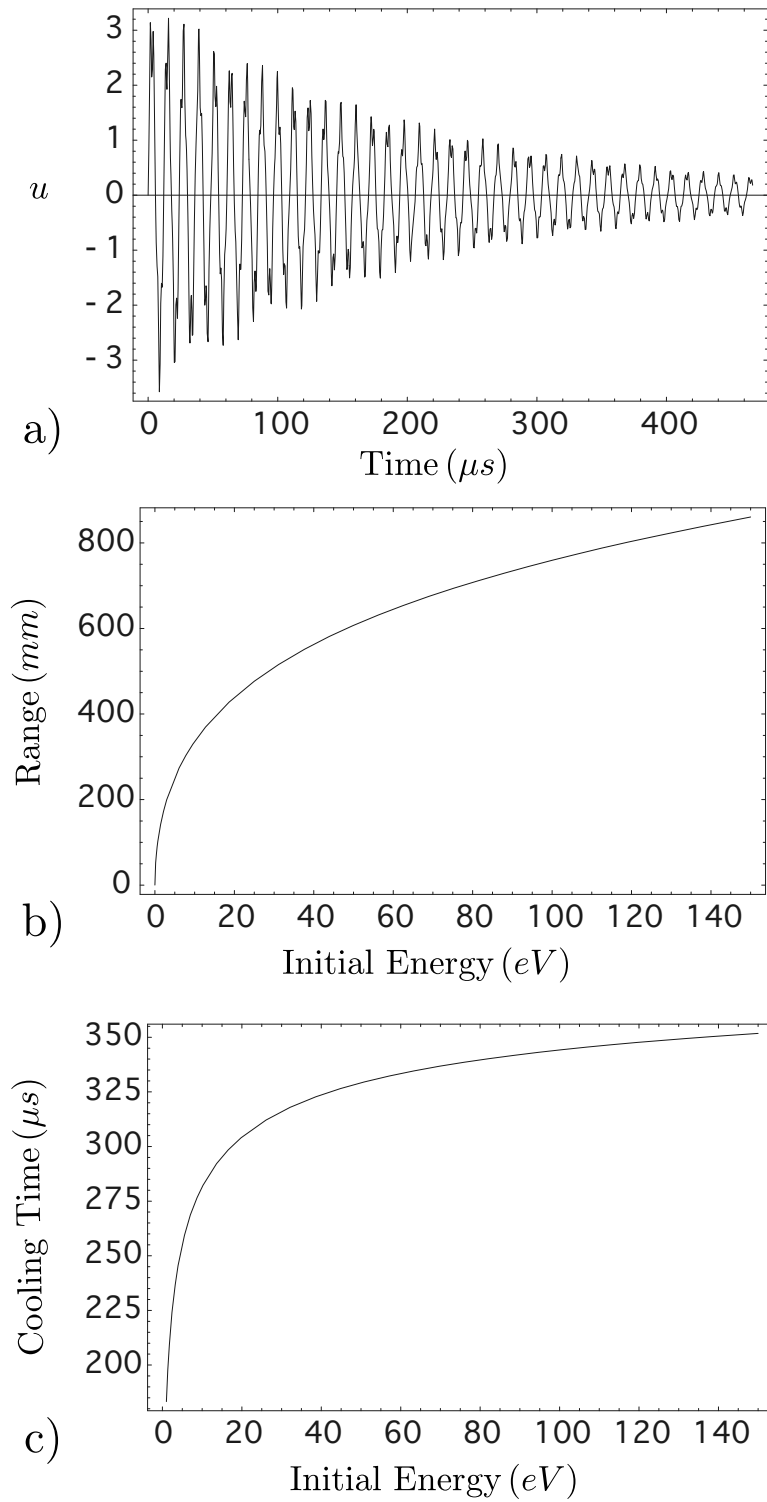
Figure 3.11: a) An ion's motion becomes damped as a result of its interaction with a buffer gas. b) The calculated range of Cs^+ ions in He at a gas pressure of 2.5×10^{-2} mbar. c) Calculated time for Cs^+ ions in He to cool to thermal energy at a gas pressure of 2.5×10^{-2} mbar.

3.2 Experimental Set-up

A general overview of the complete set up of the TITAN experiment can be seen in figure 3.12. The Penning trap and EBIT are located on a platform that sits above the ISAC floor. The ISAC beam is delivered beneath the platform. The beam is then bent through 90° and injected into the RFQ which is mounted vertically. Once extracted from the RFQ the beam is again bent through 90° and delivered onto the platform.

3.2.1 Optics Elements

There were a number of ion optical elements used for the transport of the ISAC beam to the TITAN RFQ. These kinds of devices are commonly used at radio-active ion beam facilities. Further discussion can be found in books on ion optics (see for e.g. [161] or [162]).

Einzel Lens

An Einzel lens can be formed using the electrode geometry shown in figure 3.13. A radial focusing force can be generated by placing the central electrode at a different potential than the two end plates. For a given geometry the system can be used to focus an incoming beam with the focal length dependant on the potential difference between the central electrode and the outer electrodes. There are two modes of operation for an Einzel lens. In a decelerating lens a potential is applied to the tube which is of the same polarity as the beam. In an accelerating lens the opposite is true (see figure 3.13). It is usually preferable to use an accelerating lens as they tend to produce a more linear focusing force. However, such a lens requires the application of a potential that is higher in magnitude than the longitudinal beam energy. Consequently Einzel lenses are typically only used for low energy beam transport.

Electrostatic Quadrupole

Another method for focusing a charged beam is through the use of electrostatic quadrupoles. Such devices have the same electrode geometry as the Radio-Frequency Quadrupole presented in section 3.1.3. However, because they are static they only focus in one plane, while defocusing in the other. However, by using combinations of electrostatic quadrupoles separated by short drift regions it is possible to create a net focusing force in both trans-
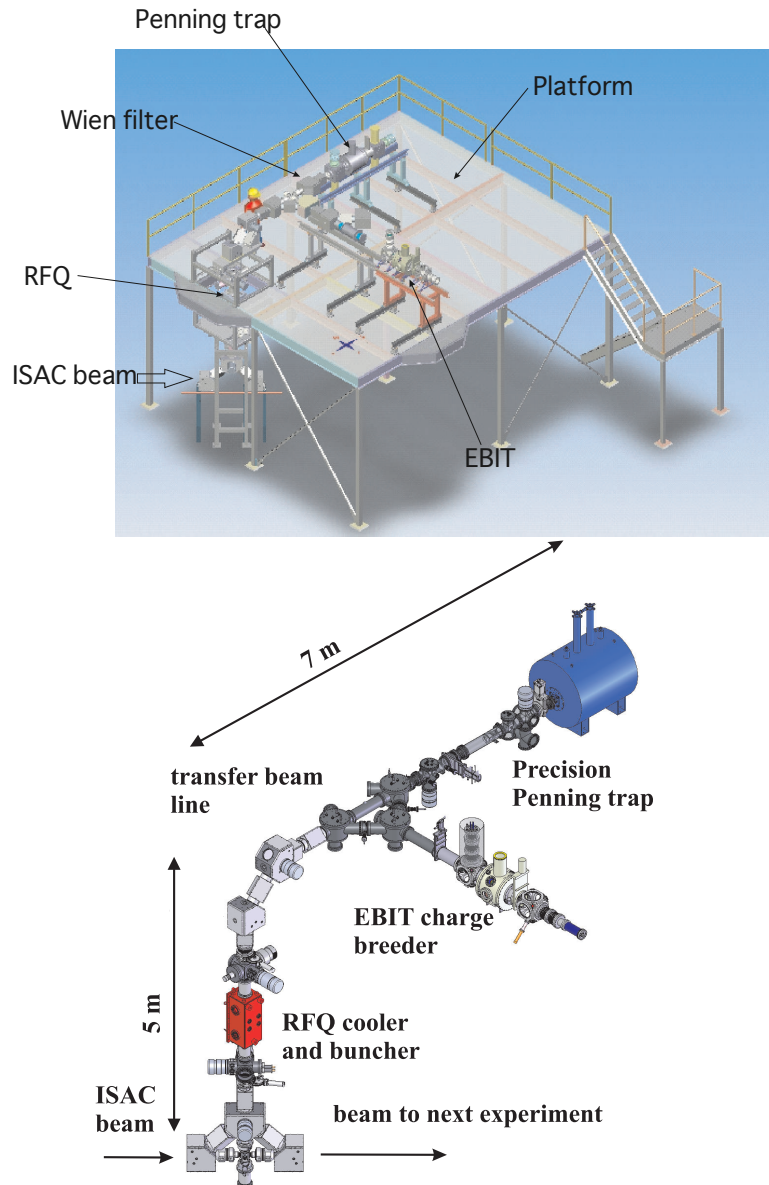
Figure 3.12: A general overview of the experiment showing the location of the ion traps with respect to the TITAN platform (top). The layout with the platform removed showing rough dimensions of the system (bottom).
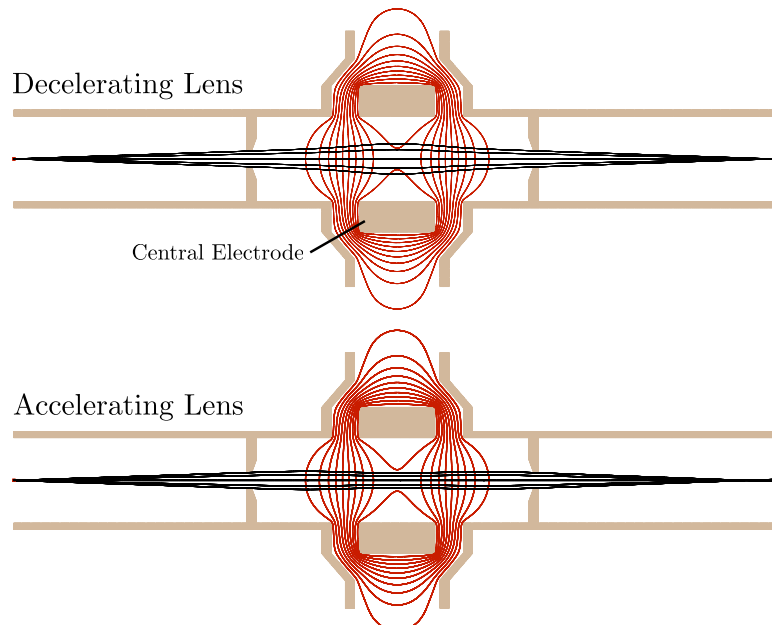
Figure 3.13: A typical geometry for an Einzel lens the ion beam enters from the left. A net focusing force can be achieved by biasing the central electrode either positively (decelerating) or negatively (accelerating) with respect to the charge state of the ion beam.
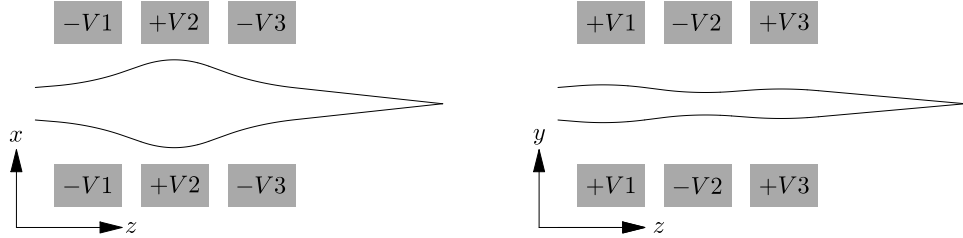
Figure 3.14: Combinations of electrostatic quadrupoles can be used to focus an ion beam in both transverse planes.
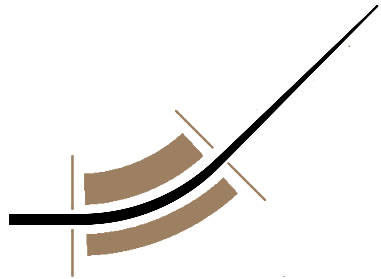
Figure 3.15: SIMION [44] simulation of a spherical bender. The bender not only steers the beam through forty five degrees but it also focuses the beam in both the bend (shown) and the non-bend directions.

verse directions. As an example the calculated trajectory of an ion beam is shown in figure 3.14 as it passes through a quadrupole triplet.

Electrostatic Benders

The most simple electrostatic benders consist of a pair of parallel plates with a potential applied across them. As an ion beam moves through the plates the resulting electric field acts so as to steer the beam. This allows for moving the beam through small angles and can be used to correct for misalignment of other optical elements. Steering through larger angles can be achieved by bending the plates or as at ISAC through the use of spherical plates. Spherical plates offer the advantage that as well as bending the beam they also focus in the bend and the non-bend directions (see figure 3.15).

3.2.2 TITAN Test Ion Source

In order to allow for off-line testing of the RFQ independent of the ISAC facility a small Test Ion Source (TIS) was mounted below the platform. The test ion beams were produced using commercial surface ion sources purchased from Heat Wave Labs (www.cathode.com). These sources consist of a rhenium filament potted in an alumina insulator. The alumina is in thermal contact with the emission surface. The surface is an alumino-silicate of the element of interest, fused into a porous tungsten disk. The filament is heated by passing a current through it which in turn heats the alumina and the emission surface. This causes ions to be released through the process of thermionic emission [163]. For testing purposes both lithium and caesium sources were used.

An ion beam was created by floating the ion source at high voltage (typically 5 to 40 kV above ground). The ions were extracted from the source using a puller electrode (TIS1:ANODE) which was biased at a few kilovolts below the source voltage. Finally the ions were accelerated towards ground such that their final longitudinal kinetic energy was defined by the floating voltage of the source. The ions were then passed through a series of steering electrodes (TIS1:XCBx and TIS1:YCBx) and an einzel lens (TIS1:EL1) before injection into the ISAC low energy transfer line (see figure 3.16).

3.2.3 ISAC Low Energy Transfer Line

After extraction from the ISAC mass separator the beam is delivered to the TITAN RFQ via a series of electrostatic quadrupoles and benders known collectively as the ISAC low energy transport line [164]. The section of beam line directly below the TITAN platform is shown in figure 3.17. The RFQ itself is mounted vertically and so the beam is bent upward using a pair of spherical benders (2T:B1). The first bender deflects the beam through 45° before it is passed through a pair of quadrupoles. The second bender only bends the beam through 36°; the final 9° bend is carried out using a pair of plates (2T:YCB3). This combination of benders forms a kind of switch yard whereby the source of the ion beam can be selected by switching the voltage on the last 9° bend. If the pair is normally biased the ISAC beam is steered up into the RFQ, if the plates are unbiased the beam from the TIS is sent to the RFQ, finally by reverse biasing the plates it is possible to send ion pulses that have been extracted from the bottom of the RFQ back into the ISAC beam line. After the switchyard the beam is then passed through a series of quadrupoles (2T:Q3, TRFC:Q1, TRFC:Q2) before delivery to the

To ILE2T

Test Ion
Source

TIS1:YCB1
TIS1:XCB1

TIS1:EL1

TIS1:YCB0
TIS1:XCB0

TIS1:ANODE
TIS1:FILBIAS

250 mm
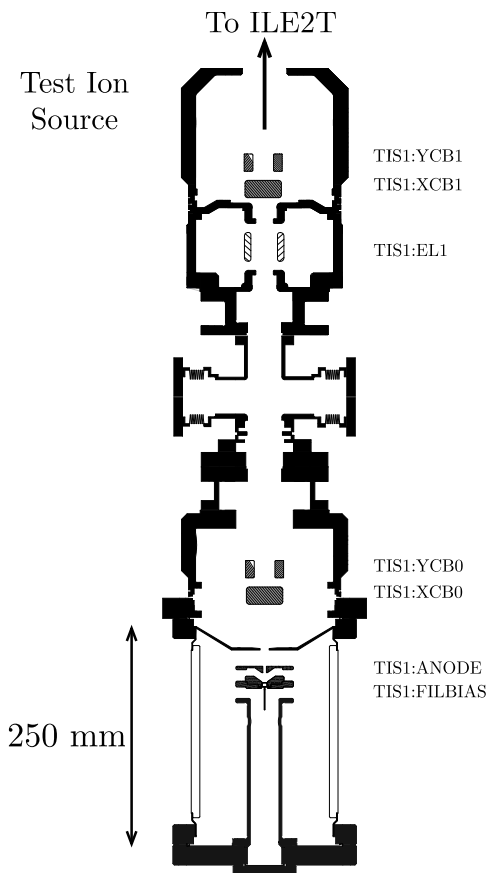
Figure 3.16: The TITAN Test Ion Source (TIS) and the ion optics used to deliver the test beam to the ISAC low energy transport line.
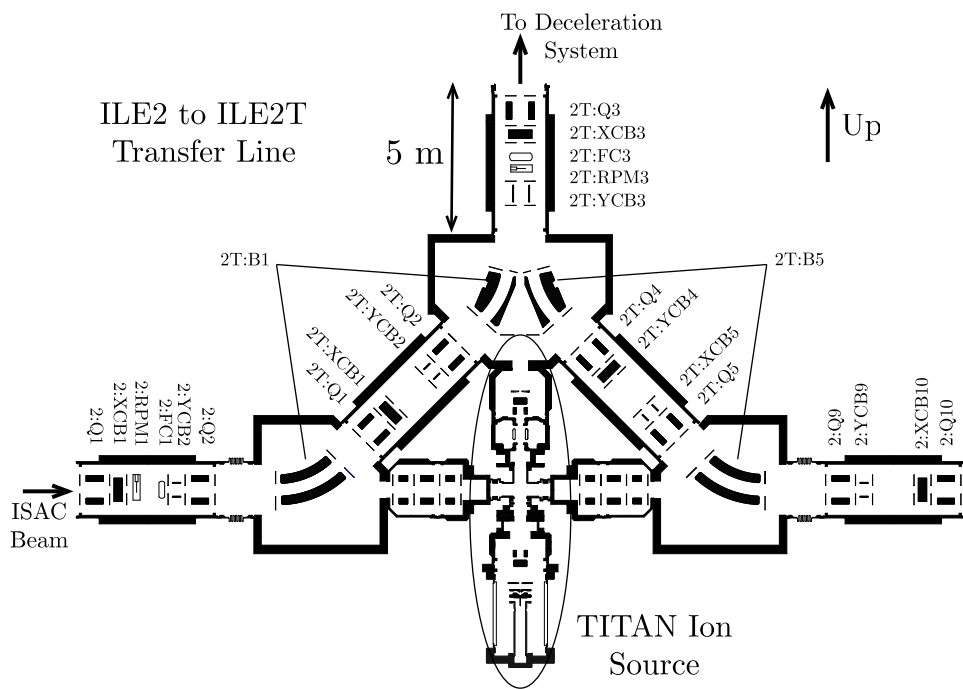
Figure 3.17: The ISAC Low Energy (ILE) transfer line in the region below the RFQ. The location of the TITAN Ion Source is indicated.
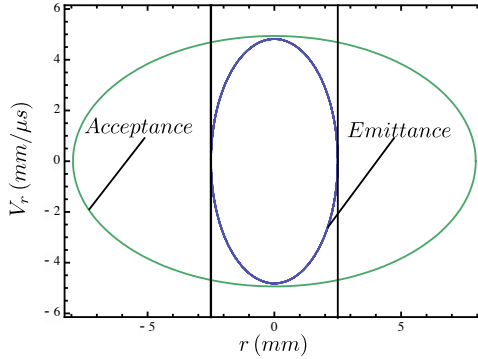
Figure 3.18: The emittance of the ISAC beam as compared to the acceptance of the TITAN RFQ. The two parallel lines represent the buffer gas aperture at the entrance to the RFQ. The beam emittance was calculated assuming an ion mass of $133\,u$ and a beam energy of $40\,$keV.

injection and deceleration system.

3.2.4   Deceleration and Injection

One of the biggest challenges in the design of a gas-filled RFQ is that of injection of the beam into the cooler. The ISAC beam can be delivered to the RFQ with energies in the range of $20\,$to $60\,$keV. An RFQ beam cooler typically accepts beams with energies in the range of $10\,$to $200\,$eV and as such the beam must be decelerated. The transverse emittance of the beam is typically on the order of $10\,\pi\,$mm mrad. However, the low energy transfer-line described in the previous section can potentially transport beams with up to $50\,\pi\,$mm mrad. The injection optics must therefore be able to take a $50\,\pi\,$mm mrad at $60\,$keV and decelerate it down to $10\,$eV whilst maintaining a good match between the emittance of the beam and the acceptance of the RFQ. The deceleration can be achieved by floating the RFQ at a voltage close to, but slightly below, the beam energy.

A set of injection optics comprising a series of aperture lenses had been commissioned as part of the initial set-up on the test stand [53]. However, It was found to be impossible to operate the RFQ at higher than $20\,$kV due to problems with the electrodes sparking. It was therefore decided to redesign the injection optics for the installation in the ISAC hall. In order to design a set of injection optics for an RFQ it is necessary to first calculate the acceptance of the device. This is complicated by the fact that the acceptance changes depending on the amplitude, frequency and phase

of the applied RF. It is therefore usual to design the optics to match the first order acceptance of the RFQ, as defined in section 3.1.4, then carry out higher order simulations to see how well the system will accept the beam.

The low energy beam transport line was designed so that the ISAC beam's transverse emittance profile would form a right ellipse at a distance of 240 mm downstream from the entrance to the RFQ. For a $50\,\pi$ mm mrad beam this right ellipse would have a radius of 2.5 mm in both transverse directions. Figure 3.18 shows the emittance profile of this beam in position-velocity space as compared to the maximum first order acceptance of the TITAN RFQ (as calculated in section 3.1.4). It can be seen that the two ellipses overlap well and that a beam with this profile would not hit the 2.5 mm radius differential pumping apertures which are needed to maintain the buffer-gas pressure inside the RFQ. The deceleration optics were therefore designed so that they could decelerate the beam whilst maintaining this emittance profile and thus provide for efficient injection of the beam into the RFQ.

We have previously noted that a beam undergoing simple harmonic motion traces out a right ellipse in position-velocity phase space. Therefore, the new deceleration optics create a radially harmonic potential such that the natural motion of an ion in the potential matches the initial emittance of the injected beam. Thus, the beam is decelerated without any change in its transverse emittance profile. Such a system has previously been described using an axially symmetric static quadrupole [156]. However, this geometry wasn't suitable as it would require some re-shaping of the RFQ electrodes. Instead the design was simplified so as to only require two deceleration electrodes, one which would sit at ground and the other at the same voltage as the floating RFQ. The potential is generated using the electrode geometry shown in figure 3.19. The required radius, r_0, can be calculated using:

$$\omega \propto \frac{\sqrt{E_{rad}}}{r_{beam}} = \frac{\sqrt{E_{long}}}{r_0}, \tag{3.47}$$

where E_{rad} and E_{long} are the initial radial and longitudinal energies of the beam and r_{beam} is its radius as it enters the decelerator. This leads to the simple condition:

$$r_0 = \sqrt{\frac{E_{long}}{E_{rad}}}\,r_{beam} \approx \frac{r_{beam}}{\theta_{beam}}, \tag{3.48}$$

where θ_{beam} is the divergence of the beam as it enters the decelerator. The beam delivered from ISAC has $r_{beam} = 2.5$ mm and $\theta_{beam} = 20$ mrad so:

$$r_0 = 125\,\text{mm},\ z_0 = \frac{r_0}{\sqrt{2}} = 88.4\,\text{mm} \tag{3.49}$$
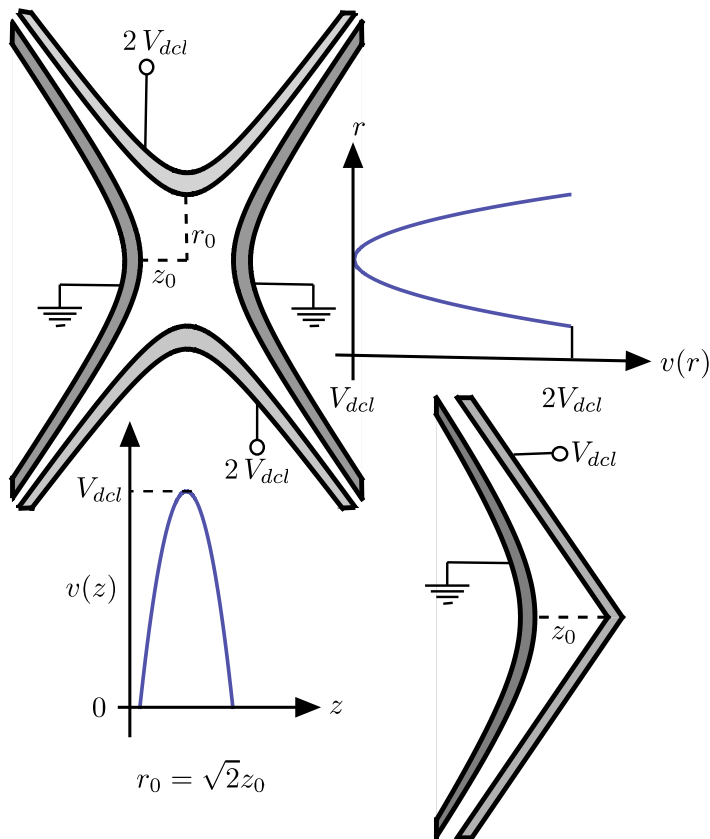
Figure 3.19: With the end-cap electrodes at ground and the ring electrode at twice the required decelerating voltage, V_{dcl}, the hyperbolic electrode structure used to generate the harmonic potential in a precision Penning trap can also provide the required harmonic potential for the deceleration system. However, a full trap geometry is not needed. Instead a quarter of a trap may be used with one end-cap electrode and one conical electrode to generate the equi-potential line at the deceleration voltage.
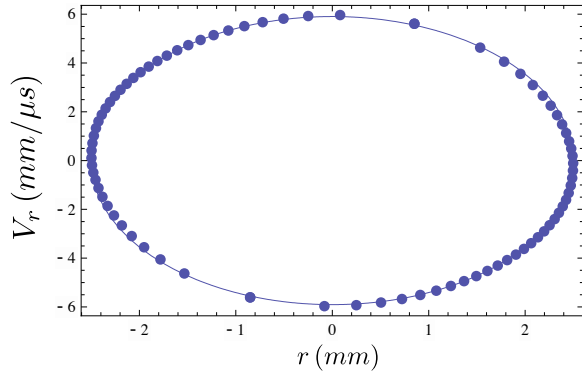
Figure 3.20: Comparison of the initial (solid line) and final (dots) emittance of a 60 keV, 50 π mm mrad beam of mass 133 u after simulated deceleration with the new injection optics. There are some minor differences between the two ellipses. However, they are close to identical.

The final design of the deceleration system was based on simulations carried out using the ion optics package SIMION [44] . These simulations were necessary in order to take into account deviations from the ideal harmonic potential. Such deviations can be created by the introduction of apertures in the deceleration electrodes to allow for injection of the ions and by the truncation of the electrodes which are ideally infinite. SIMION works by solving the Laplace equation numerically using finite element methods. The solution is found on a regular grid, and an array of values for the electrostatic potential at each point on the grid is generated. The trajectories of ions can then be simulated as they move through the resulting array of values for the electrostatic potential. Electrodynamic effects can also be approximated by changing the potential applied to the electrodes as the ions propagate through the array. The changing of potentials can be controlled via user programs written in the Lua scripting language. Two sets of simulations were carried out. The first was a simple two-dimensional simulation of the system which ignored the effects of the electrodynamic field applied to the RFQ. This simulation was carried out on a relatively fine grid with ten grid units per millimetre. These simulations showed that although the effects of truncating the electrodes were negligible, the injection apertures act so as to slightly focus the injected beam. A simple solution to this problem was to place an einzel lens before the decelerator. The lens was placed so as to exactly compensate for the focusing effect caused by the apertures in the decelerator. Figure 3.20 shows the results of the two dimensional simula-

74
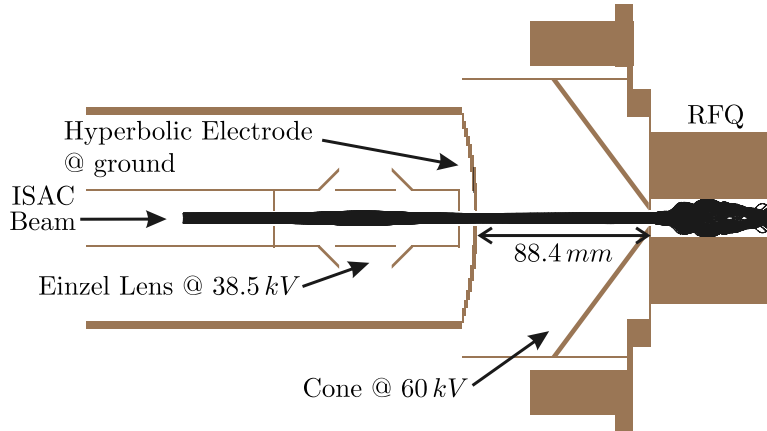
Figure 3.21: SIMION simulation of the new deceleration optics for the TI-TAN RFQ. Here a 40π mm mrad beam is decelerated from 60.1 keV and injected into the RFQ, $q = 0.3$, $V_{pp} = 400$ V, with 100% efficiency.

tion. It can be seen that with the inclusion of the einzel lens the decelerator perturbs the emittance profile of the injected beam very little. Finally, a full three dimensional simulation was carried out on a coarser grid size (one grid unit per millimetre). The effects of the RF potential were included in this simulation. It was found that at an applied peak-to-peak voltage of 400 V a 60 keV, $40\,\pi$ mm mrad beam could be injected into the RFQ without losses (see figure 3.21). However, a peak-to-peak voltage of 600 V is required to fully accept the $50\,\pi$ mm mrad at 60 keV. The final design of the deceleration system is shown in figure 3.22 including the einzel lens (TRFC:DCL3), the hyperbolic electrode (TRFC:SK3C) and the deceleration cone (TRFC:SK4).

3.2.5 Radio-Frequency Quadrupole

The mechanical structure of the Radio-Frequency Quadrupole is essentially the same as described in my masters thesis [53]. However, for completeness it is desirable to repeat this description here. The vacuum and high voltage systems associated with the RFQ were modified for the new installation in the ISAC hall.
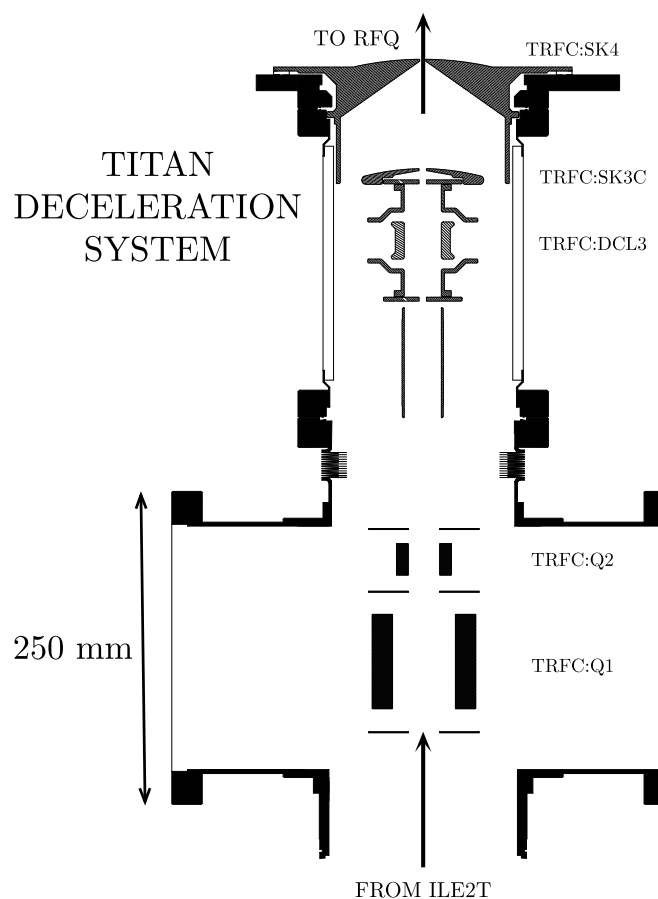
Figure 3.22: The new deceleration system for the TITAN RFQ.

Mechanical Design

The structure of the RFQ is shown in figures 3.23 and 3.24. The trap has an $r_0 = 10$ mm, is 700 mm long and was segmented longitudinally into twenty four pieces. The main body of the trap consists of eleven segments each 40 mm long. Twelve 20 mm sections were used at the ends of the trap, seven at the trap entrance and five at the trap exit, along with one 9 mm piece. The shorter electrodes were used so as to give greater control over the longitudinal potential in the injection and bunching regions.
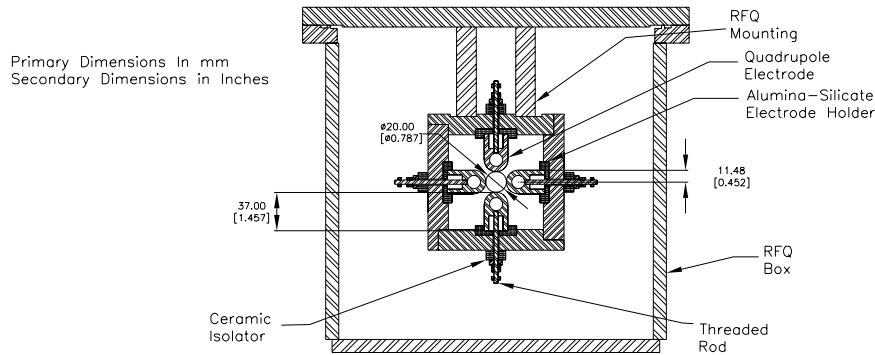
Figure 3.23: Mechanical drawing of the RFQ design (end view).

The RFQ electrodes were machined in a 'pillbox' shape. This allowed for the electrodes to be easily mounted on four specially machined alumina-silicate electrical isolators. The isolators were designed to hold the electrode pieces such that they were equally spaced and properly aligned. The isolators were held in place by three metal frames which were mounted on the lid of the RFQ box (see figure 3.24) . This meant that the structure could easily be lifted in and out of the box if maintenance was required. Opposing pairs of electrodes were wired together using stainless steel welding rod. The box lid had fifteen $2\frac{3}{4}''$ ConFlat flanges welded to it to allow for the mounting of electrical feedthroughs and for the attachment of a gas feeding system.

High Voltage Considerations

In order to decelerate the incoming beam before cooling the RFQ is floated at a voltage, V_f, close to that of the beam energy. To achieve this the RFQ
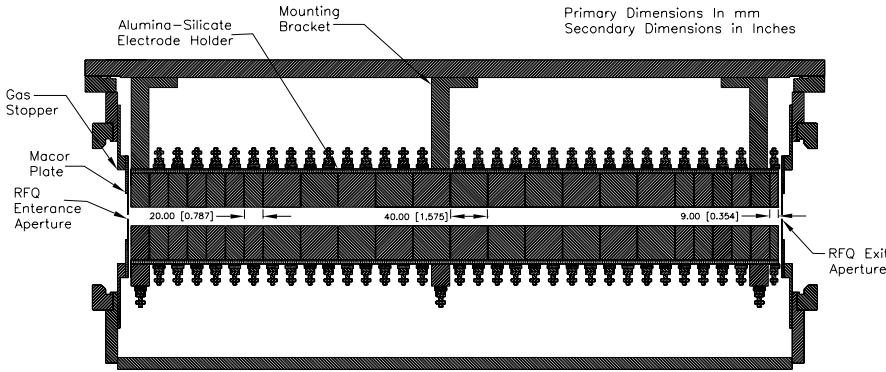
Figure 3.24: Mechanical drawing of the RFQ design (side view).

itself was mounted in an large vacuum vessel which was isolated from ground using ceramic insulators which where capable of holding 60 kV electrostatic potential. The whole device was mounted inside a Faraday cage (cage 2 in figure 3.25). The square-wave driver was also placed inside the cage, on ceramic insulators, and floated to the same potential as the RFQ. A second Faraday cage was built on the platform and all the electronics required for the RFQ were placed within. The gas feeding system for the RFQ was also placed inside this cage. The two cages were floated at a common potential and were connected via a duct. This duct allowed for cables to be passed from one cage into the other. The test ion source was placed inside a third Faraday cage which was connected through a second duct to the RFQ cage. The source was floated using the same supply as the RFQ, however a second supply was also used so as to be able to apply a small offset in voltage, δV, between the two devices. This offset defined the injection energy of the ion beam as it entered the RFQ.

Vacuum and Gas Flow

An overview of the vacuum system for the TITAN RFQ is shown in figure 3.26. The gas feeding system was mounted in the Faraday cage on the platform. The gas was then fed into the RFQ via a stainless steel tube that ran through the duct between the two cages. Gas pressure, typically on the order of 1×10^{-3} to 1×10^{-2} mbar, was maintained inside the RFQ box through the use of differential pumping apertures. These apertures had

78
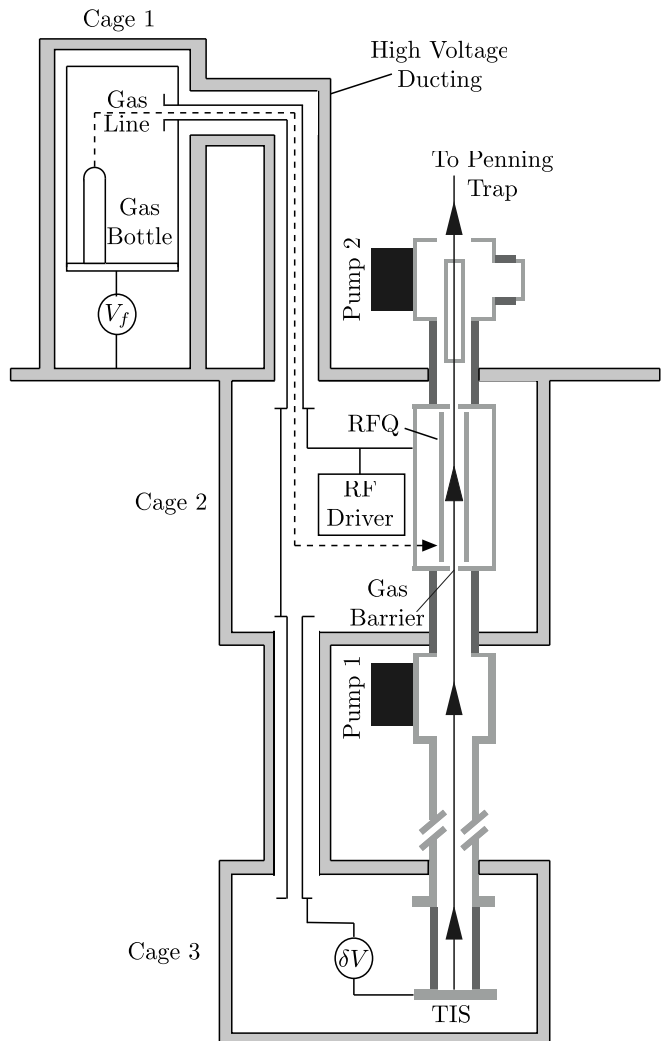
Figure 3.25: Schematic overview of the high voltage set-up for the TITAN RFQ.
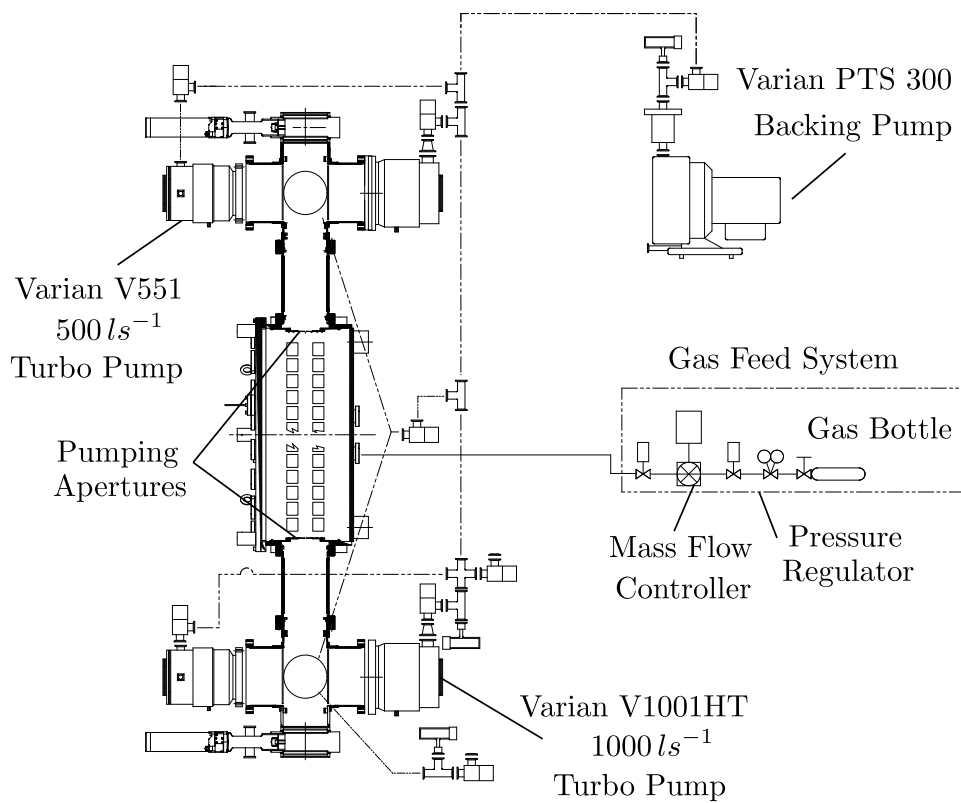
Figure 3.26: Overview of the vacuum system for the TITAN RFQ.

5 mm diameters to allow for the injection of the ion beam into the RFQ. Pumping was achieved through the use of both a 1000 l/s and a 500 l/s turbo-molecular pump mounted at ground on the vacuum crosses at either end of the RFQ.

Square-Wave-Driver

The square-wave was generated using fast switching MOSFETs (Metal-Oxide-Semiconductor Field-Effect Transistor). A simple signal amplifier can be generated by using two such MOSFET's in a push-pull configuration (see figure 3.27). A method for stacking a series of MOSFETs such that high voltages, $V \leq 25$ kV, could be switched with repetition rates of up to 77 kHz had already been developed at TRIUMF for use in the MuLan experiment at the Paul Scherrer Institute in Switzerland [164]. Each MOSFET was placed on a separate circuit board electrically isolated from ground. Power was magnetically coupled to the board via an inductive core and the trigger signal relayed via optical fibre. This meant that the common voltage on each board could follow the voltage on the MOSFET's source ensuring that the gate-source junction remained forward biased regardless of the voltage on the source. The square-wave generator used was based on this system. The whole system can simply be considered as a square-wave-driven RC circuit. The RFQ presents a capacitative load, along with the capacitance of the MOSFETs themselves and the capacitance of all the wires etc used to connect the driver to the RFQ rods. There is also a resistance in the circuit so as to limit the current passing through the MOSFETs. The repetition rate is limited by the rise time of the voltage which is dependant on the RC time constant for the circuit. The system was designed to switch a maximum peak-to-peak voltage of 400 V at frequencies of up to 1.2 MHz. Two stacks of three DE375-102N12A MOSFETs from Directed Energy Incorporated were used to create each phase of the square-wave. These MOSFETs have fast switching times (≈ 5 ns), can operate with a maximum voltage between the drain and the source equal to 1 kV and can be operated with a maximum current between the collector and the emitter of 72 A. To generate a square wave of 400 V_{pp} only requires two MOSFETs. However, by stacking the chips the power dissipated by each of the chips is reduced increasing the maximum frequency at which it is possible to drive the MOSFETs. Stacking the MOSFETs also has the desirable effect of reducing the total capacitance of the stack as their individual capacitances add in series. It also allows for further MOSFETs to be added in the future making it possible to switch voltages larger than 1 kV. Detailed simulations and experimental measure-

ments of the total capacitance of the RFQ system were carried out and the total capacitance found to be around 1500 pF [165]. Assuming that the system is symmetrical this means that each pair of rod represents a capacitance of 750 pF. A resistance of 75 Ω was used to limit the current through the MOSFETs. This gives an RC time constant for the circuit of $\tau = 56$ ns and a rise time (10% $\rightarrow$ 90%) equal to 124 ns. At an operating frequency of 1 MHz the combined rise and fall time is approximately 10% of the period of the applied RF.
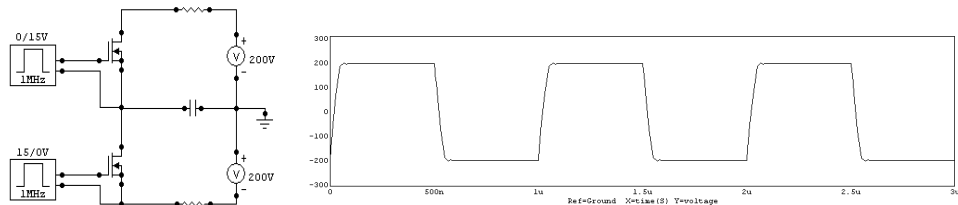
Figure 3.27: A simple push-pull system for creating a high amplitude square-wave. The wave is generated by alternatively forward biasing the gate-source junctions of the MOSFETs. Each trigger floats at the respective source voltage. This ensures that the MOSFETs remain forward biased as the source voltage changes. The waveform shows the voltage between the MOSFETs as a function of time.

The driver was tested directly by applying voltage to the RFQ rod structure. To minimize the length and hence the capacitance of the connecting wires the driver was mounted beside the RFQ box. The square-wave was then put onto the RFQ electrodes via coupling capacitors (see figure 3.28). The voltage over the MOSFETs was supplied by a single supply. A square-wave was generated between 400 V and ground. The coupling capacitors converted this to a wave between ± 200 V. The longitudinal potential was supplied from separate DC power supplies and then added to the AC signal using coupling resistors. The value of the resistance, 10 MΩ, was chosen such that it was much larger than the impedance of the RFQ. This ensured that the RF did not flow into the DC supply. The resulting measured waveform is shown in figure 3.29. A second version of the driver has also been commissioned driving a dummy load. This driver can be run at 600 V$_{pp}$ (peak-to-peak) at up to 1 MHz and 400 V$_{pp}$ at up to 3 MHz . When installed this version of the driver will be able to trap over the full mass range available at TRIUMF without the need to reduce the applied voltage below 400 V$_{pp}$.
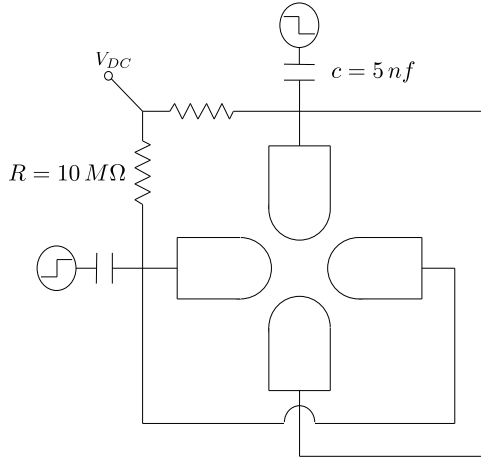
Figure 3.28: The AC potential is coupled to the electrodes via a capacitor and the DC potential via a resistor. A resistance is chosen that is large compared to the impedance of the RFQ such that the AC signal doesn't flow into the DC supply.
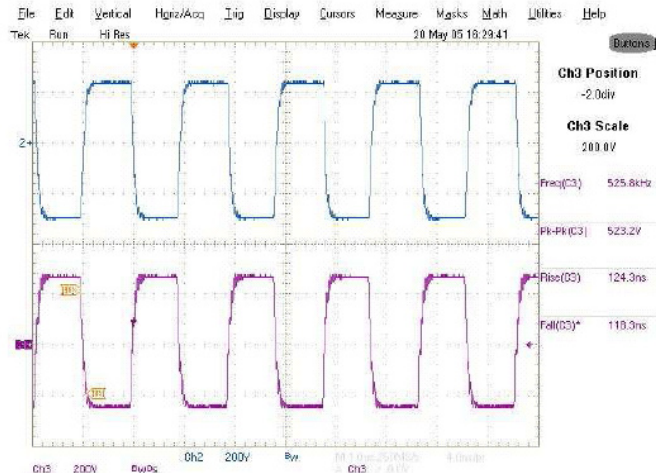
Figure 3.29: Oscilloscope screen shot of both phases of the applied waveform taken directly from the RFQ rods. Both waves have a 500 V peak-to-peak amplitude and are set to oscillate at a frequency of 526 kHz. It was later decided to limit the operating voltage to 400 V in this configuration as this reduced the current load on the MOSFETS.
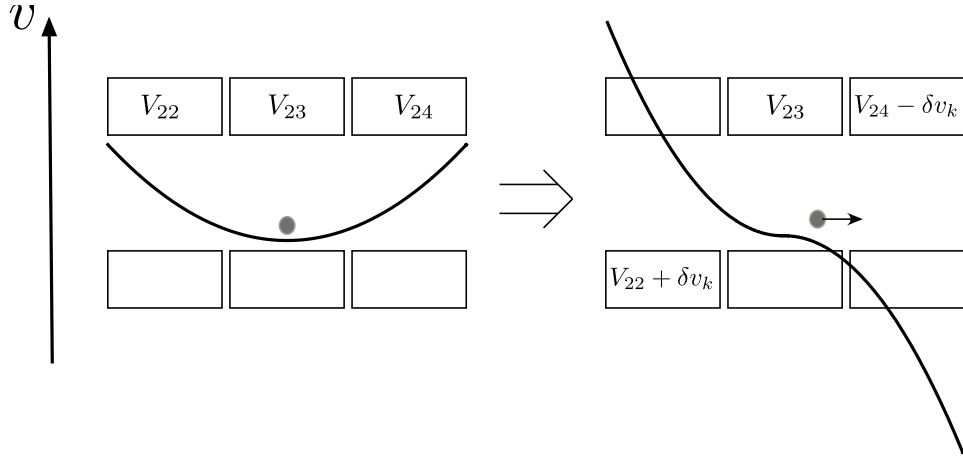
Figure 3.30: Extraction of an ion pulse from the RFQ is achieved by applying a kicking voltage δv_k to the last (#24) and third from last (#22) segments.

3.2.6 Extraction and Re-Acceleration

Extraction of an ion pulse from the RFQ is achieved by pulsing the DC potentials applied to the RFQ electrodes as shown in figure 3.30. The ions are then re-accelerated using electrostatic optics.

Pulsing Methods

The simplest method for pulsing the DC voltage applied to the RFQ electrodes is to use a push-pull switch as shown in figure 3.31. The rise time of the applied pulse is governed by the RC time constant of the coupling capacitor and the load resistance. It was found experimentally that in order to properly pass the square-wave without significant attenuation a coupling capacitor of at least $2\,\mathrm{nf}$ must be used. When coupled with the minimum resistance required so as to not overload the RF driver, $40\,\mathrm{k\Omega}$, this gives a time constant of $80\,\mu\mathrm{s}$. Simulations had shown that the ion bunch would take on the order of $10\,\mu\mathrm{s}$ to exit the trap. The rise time for the extraction pulse using this method is then significantly longer than the extraction time from the trap which is undesirable.

Two methods were considered for reducing the RC time constant. The first involves floating the push-pull switch on the RF such that the load resistance is no longer needed. The second was to inductively couple the RF onto the extraction electrodes, thus removing the coupling capacitor.
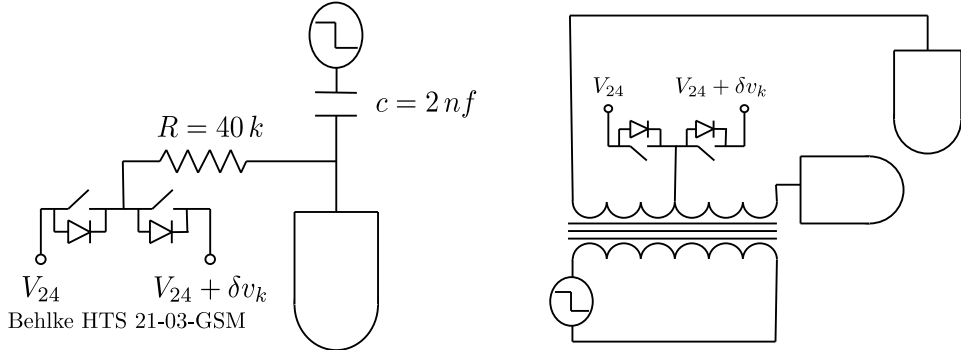
Figure 3.31: Pulsing of the last RFQ segment can be applied using a simple push-pull switch (left). However, the rise time is governed by the RC time constant. Inductively coupling the RF onto the electrodes removes the coupling capacitor and so decreases the rise time (right).

The first method is more in keeping with the broadband philosophy behind using a square-wave-driver. However, it was considered to be technically too difficult to implement with the current driver set-up. The second method introduces transformers and hence a LC circuit formed by the capacitance of the RFQ electrodes and the leakage inductance of the transformer. If the resonant frequency of the LC circuit is much higher than the maximum operating frequency of the square-wave-driver then the square wave should be passed by the transformer without the introduction of ringing. If not the LC circuit will begin to resonate distorting the induced waveform. It was found that by using a separate transformer for each segment the capacitive load was low enough that any ringing on the applied waveform was negligible over the frequency range $200\,\mathrm{kHz}$ to $1\,\mathrm{MHz}$ at up to $400\,\mathrm{V}_{pp}$. However, if in the future a square-wave-driver with significantly increased RF voltage ($\mathrm{V}_{pp} > 1\,\mathrm{kV}$) is constructed this method will not be practical.

Re-acceleration

The re-accleration optics have a fairly simple design which is shown in figure 3.32. The ions are extracted from the RFQ and accelerated using the inverse of the deceleration optics described in section 3.2.4. They are then focused using an accelerating Einzel lens and passed through a differential pumping barrier. In the DC mode of operation the longitudinal energy of the extracted beam is always equal to that of the injection energy as the ions are re-accelerated towards ground. However, in pulsed mode the transport

RFQ
@ 60 kV

Pulsed Drift Tube
$\Delta V = 1\,kV$

Einzel Lens
@ $-1.6\,kV$

Differential Pumping Aperture

59 kV

Behlke HTS 651-01-GSM
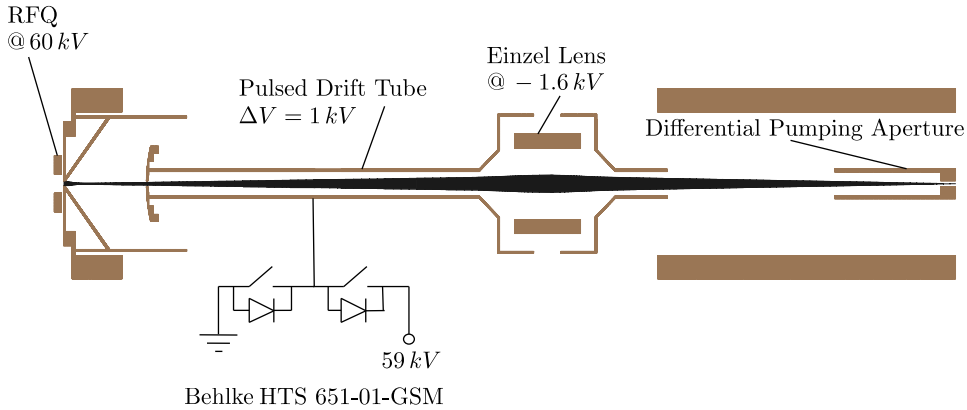
Figure 3.32: Extraction optics for the TITAN RFQ. An ion pulse accelerated to 1 keV longitudinal kinetic energy before entering a pulsed drift tube. The potential on the tube is then switched using a push-pull switch such that the ions leave the tube at ground. The ions are subsequently focused so that they pass through a 5 mm differential pumping aperture using an Einzel lens placed half way between the RFQ and the aperture.

energy of the extracted bunch can be reduced by first accelerating the ions into a drift tube with the required transport energy (see figure 3.32). Once the ions are inside the tube its potential can be pulsed to ground. Thus the ions leave the tube at ground potential with a kinetic energy equal to the initial potential difference between the RFQ and the tube, ΔV. Figure 3.33 shows the full layout of the extraction optics including the bender used to bring the cooled beam up onto the TITAN platform.

3.2.7 Beam Detection and Diagnostics

A number of different systems for beam detection were used in order to commission the TITAN RFQ. The positions of these devices are shown in figures 3.17 and 3.22.

Faraday Cup

For detection of ion currents a simple Faraday cup was used. If an ion beam impinges on a metal plate then the beam current can be read directly by placing an ammeter between the plate and ground. However, the ion beam can also cause secondary electrons to be released from the plate's surface. Hence, the net current between the plate and ground can be greater than the

To Penning
Trap

TRFCBL:B1

TRFCBL:Q4
TRFCBL:Q3
TRFCBL:MCP0
TRFCBL:Q2
TRFCBL:Q1

TRFCBL:XCB0

TRFCBL:FC0

300 mm

Buffer Gas Aperture

TRFC:EL5

TITAN
Acceleration
System

TRFC:PB5

TRFC:SK5
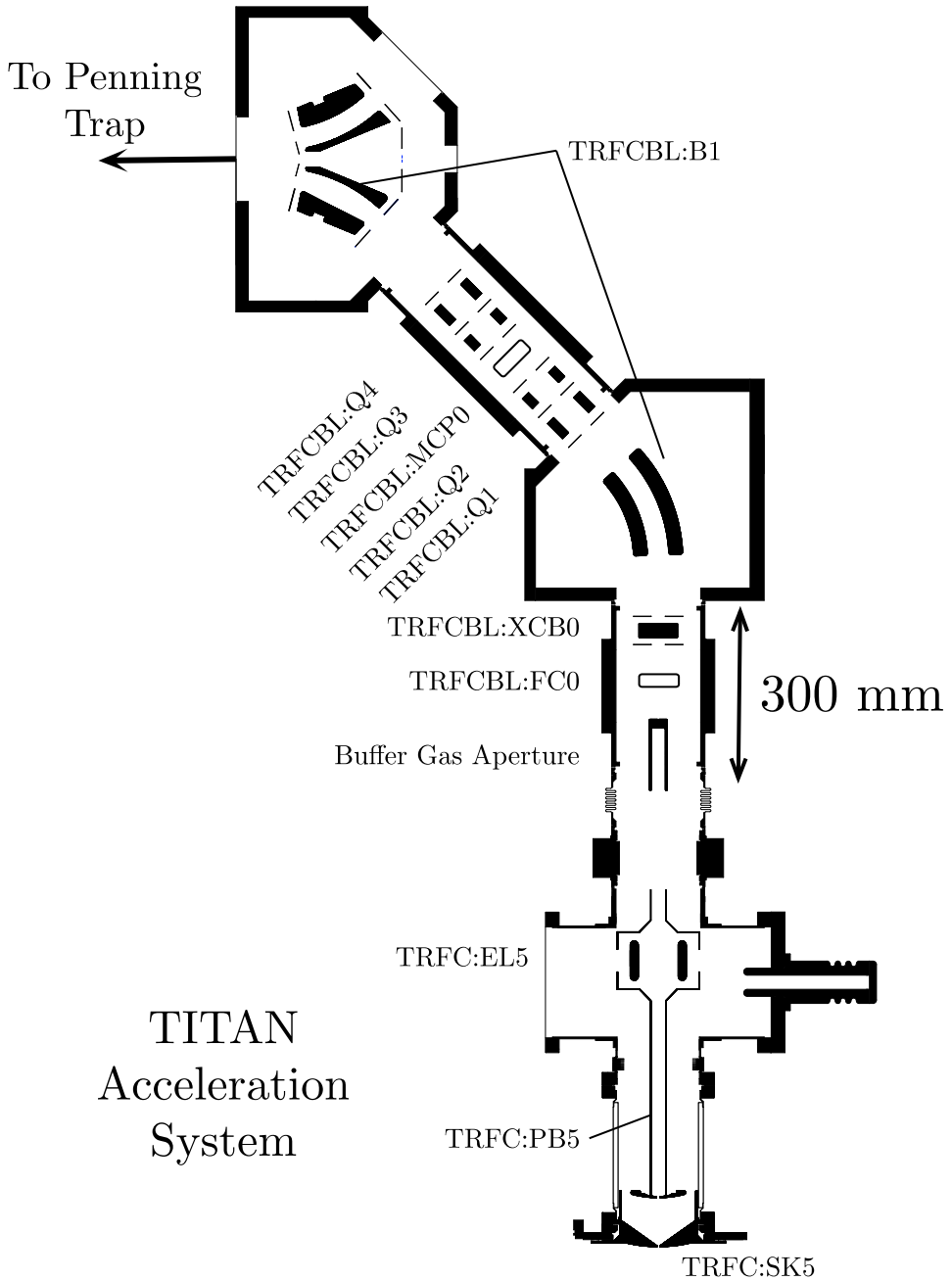
Figure 3.33: The TITAN acceleration system.
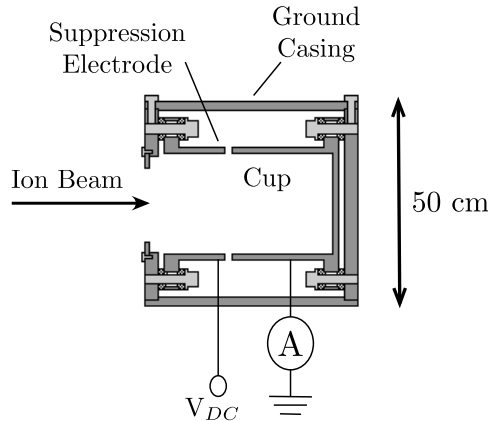
Figure 3.34: A typical Faraday cup design.

beam current. To reduce this effect a cup is used instead of a plate. If the depth of the cup is much greater than its diameter then the probability of electrons leaving the cup is reduced, leading to an improved current reading. A long narrow cup can only be used if the divergence of the ion beam is small. Usually this is not the case. A shorter cup can be used with an electrically biased plate at its entrance. By applying a negative voltage to the plate an electric field is created that repels the secondary electrons back into the cup. A typical Faraday cup design is shown in figure 3.34.

Rotating Profile Monitor

A Rotating Profile Monitor (RPM) passes a helical-shaped wire probe through the incident ion beam first in the horizontal and then in the vertical direction. As the beam strikes the wire secondary electrons are created which are subsequently detected. A plot of the electron current as a function of the wire's position then gives the corresponding beam profile.

MCP and Channeltron

Faraday cups lack sensitivity below $I = 10 \, \text{pA}$ due to inherent noise in the electrical system. For detection of smaller ion currents some form of current amplification is first needed. Both MCP and Channeltron detectors work by amplifying the number of secondary electrons produced when an ion beam impinges on a surface of low work function. The amplification takes place by repeatedly accelerating the secondary electron beams between
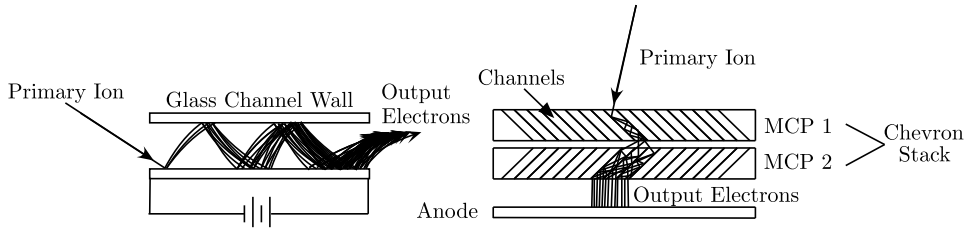
Figure 3.35: A single channel electron multiplier (left) and a chevron stack MCP (right). In a electron multiplier an accelerating voltage is applied over the length of a narrow semiconducting tube. The secondary electrons produced when the incident ion hits the tube are thus accelerated until the in turn collide with the tube wall. This repeats producing an avalanche of secondary electrons.

successive collisions with the surface (see figure 3.35). A channeltron is large single channel electron multiplier which gives a final current which is simply proportional to that of the incident ion beam current, with a typical gain is on the order of 10^7. A Micro-Channel Plate (MCP) is an array of electron multipliers formed into a thin glass plate [166]. The plates can be stacked so as to further increase the gain. The resultant electrons can either be detected electronically or optically through the use of a fluorescent phosphor screen.

3.3   Test Results

The RFQ was tested using both caesium and lithium beams from the test ion source. For efficient cooling of the beam the mass of the gas atom should be significantly less than that of the ion such that the ions are not significantly perturbed from their initial trajectories upon collision. When cooling lighter ions such as lithium the choices of potential buffer gases are therefore limited. Two potential candidates were identified: helium and molecular hydrogen (H_2). The cooling of light ions in H_2 had previously been investigated with an RFQ at the GANIL facility in Caen, France with reasonable efficiencies on the order of 10% [167]. However, cooling in H_2 was initially discounted due to the explosive nature of the gas. Initial tests were therefore carried out in helium. However, during the testing an opportunity arose to measure the mass of ^{8}He with the spectrometer. This couldn't be cooled in helium due to resonant charge exchange and so H_2 was used. Once the use of H_2 in the TITAN RFQ was formally approved tests were also carried out to study

89

the cooling of lithium in helium.

3.3.1 DC transmission tests

For these tests the efficiency of the RFQ in DC mode was studied systematically as a function of gas pressure, RF voltage, RF frequency and injection energy (δV). The DC effiency was defined simply as the ratio of the extracted ion current, as measured on TRFCBL:FC0 (see figure 3.33), to the injected current, as measured on ILE2T:FC2 (see figure 3.17). The tests were carried out for both caesium at an initial beam energy of 5 keV and lithium at 20 keV. The beam widths were measured using the ILE2T:RPM3 (see figure 3.17) as a function of the voltage applied to the Einzel lens TIS1:EL1 (see figure 3.16) which were then used to get the emittance of the ion beam using a transfer matrix found through SIMION simulation (see appendix A). It was found that the TIS beam had a transverse emittance of $\epsilon_{99\%} = 25 \pm 5 \, \pi \, mm \, mrad$ at both 5 keV and 20 keV which matched well with SIMION simulations of the source which predicted $\epsilon_{99\%} = 30 \, \pi \, \text{mm} \, \text{mrad}$. In all cases an initial ion current on the order of a nano-amp was used and a 7 V DC gradient was applied across the length of the RFQ.

Figure 3.36 shows the efficiency of the transfer of the caesium in helium as a function of the buffer gas pressure for different injection energies ($V_{pp} = 400$ V, $f = 600$ kHz). In general the efficiency of the RFQ increases as the initial energy of the ions decreases. This is because the ions are more likely to be scattered into the RFQ electrodes through high energy collisions than low energy collisions. At very low energy the efficiency falls this is probably due to the longitudinal energy spread of the beam, at low energies a proportion of the beam will not be sufficiently energetic to enter the cooler. The efficiency as a function of the stability parameter q is also shown in figure 3.36 ($\delta V = 20$ V, $p = 5 \times 10^{-3}$ mbarr) . Maximum transmission occurs at $q \approx 0.5$, this corresponds to the deepest psuedo-potential in the RFQ. The advantage of running at higher voltages can be easily seen as the efficiency rises with the peak-to-peak voltage.

Figure 3.37 shows the DC efficiency of stable lithium in both hydrogen and helium as a function of the rate of flow of the gas into the RFQ ($f = 1.15$ MHz, $V_{pp} = 80$ V). It can be seen that with both gases good DC efficiencies can be obtained although the peak DC efficiency in hydrogen ($\approx 40\%$) is twice that of helium ($\approx 20\%$). Using the original version of the RF driver the frequency couldn't be increased above 1.2 MHz. This meant that the RFQ could not be operated at the full $400 \, V_{pp}$ and still have a suitable trapping parameter, q, for lithium ions. The voltage of
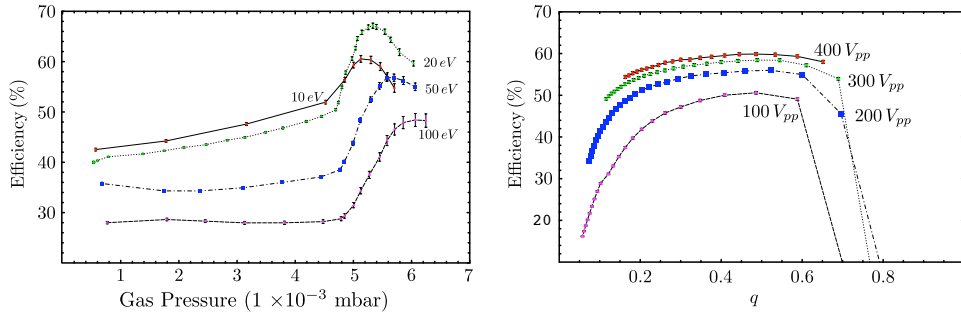
Figure 3.36:   The DC transmission efficiency of caesium ions in helium through the TITAN RFQ.
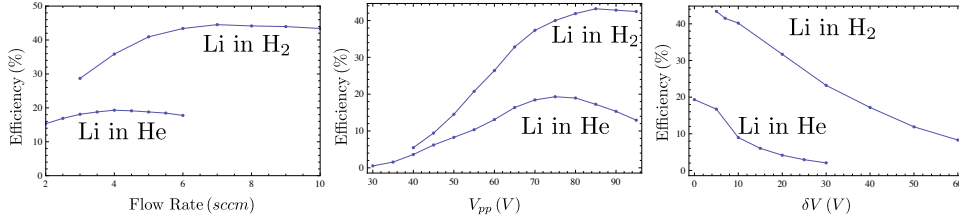
Figure 3.37:   The DC transmission efficiency of lithium ions in helium and H_2 through the TITAN RFQ as a function of flow rate, RFQ square-wave-voltage V_{pp}, and offset voltage δV (as defined in figure 3.25).

the applied RF was thus varied at fixed frequency ($f = 1.15\,\mathrm{MHz}$) to find the peak transfer efficiency. This occurred at slightly different voltages for the two gases but was generally higher than that for operation of the RFQ without gas. Also of note is the efficiency as a function of δV (as defined in figure 3.25). Unlike for caesium in helium it can be seen that a lower δV always resulted in an increased transfer efficiency. Due to the light mass of lithium the RFQ had to be run at a lower peak-to-peak voltage than for caesium resulting in a shallower pseudo-potential. This combined with large scattering angle associated with collisions between ions and gas atoms that are similar in mass leads to significant losses for higher energy collisions.

3.3.2   Pulsed Operation

Pulsed operation of the RFQ was demonstrated by detecting the extracted pulses on TRFCBL:MCP0. The signal induced on the MCP's anode was capacitively coupled onto a scope as shown in figure 3.38. The ions were
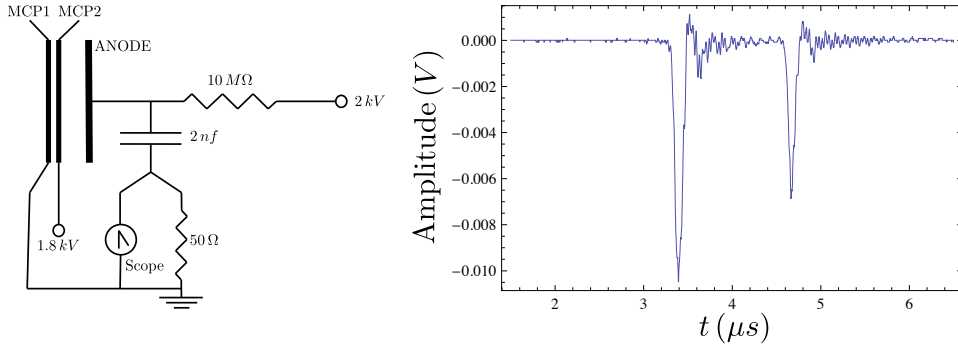
Figure 3.38: Two signals induced on the MCP corresponding to ^{6}Li and ^{7}Li. The signals were capacitively coupled into an oscilloscope as shown. The oscilloscope traces are the average of the signal induced by 128 individual pulses.

collected by keeping the same 7 V DC potential but with the potential on the last RFQ electrode raised above the high voltage bias. For caesium ions a deep well was formed by lowering the potential on the penultimate electrode (#23) to around -11 V . However, for lithium ions it was observed that this would result in ion pulses of severely reduced amplitude. This was due to scattering of the ions as they are accelerated into the deeper well. A typical pair of detected lithium pulses is shown in figure 3.38 . There are two peaks; the earliest and therefore the lightest corresponds to ^{6}Li, the later to ^{7}Li.

The width of the ion pulses as a function of the extraction voltage is shown in figure 3.39. It can be seen that extremely short pulses, 30 ns FWHM, were achievable. The pulse width was also observed to decrease with increased extraction amplitude with a plateau at around 100 V. It was also observed that the pulse width increased when the pulse drift tube was used to reduce the ion's extraction energy from 5 keV to 1 keV. This was also coupled with a reduced capture efficiency in the Penning trap due to an increase in the longitudinal energy spread. This was found to be due to the power supply used to pulse the drift tube being unable to drive a dynamic load. Hence, the potential on the electrode would drift after the tube was switched back to high voltage. This time dependant potential would lead to parts of the ion pulse being accelerated by different amounts thus increasing the longitudinal energy spread. A large, 3 μf, buffer capacitor has since been purchased to be installed in parallel to the power supply. It is hoped that this will reduce the amount of drift resulting in ion bunches with properties similar to those without the pulsed drift tube.
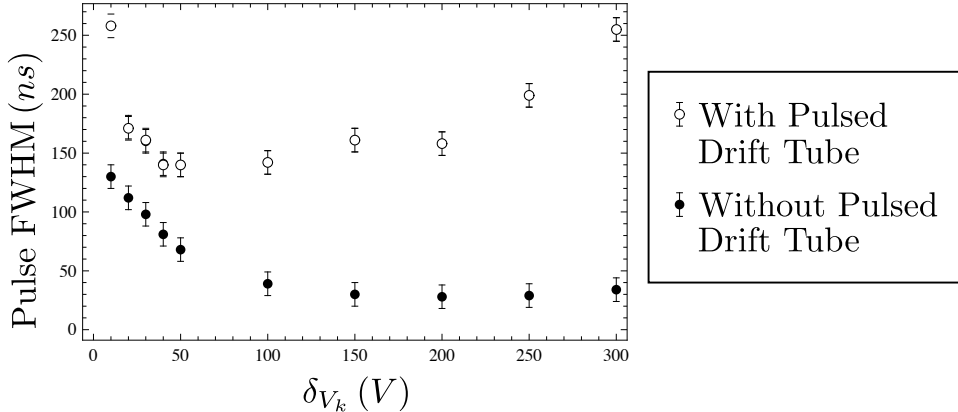
Figure 3.39: Measured pulse widths (Full Width Half Maximum) as a function of extraction voltage, δ_{V_k}. It can be seen that without the pulse drift tube pulse width on the order of 30 ns were achievable. Using the pulse drift tube to reduce the longitudinal energy from 5 keV to 1 keV caused significantly deterioration the pulses with a best achievable width on the order of 150 ns.

3.3.3 Life-times in the Trap

The cooling of an ion beam through elastic scattering is, unfortunately, not the only possible interaction possible with the gas. Other effects such as charge exchange and the formation of molecules can also occur. These effects lead to the gradual loss of the ions in the trap, thus the ions can only be stored for a finite amount of time. These effects were studied by injecting a short pulse of ions into the RFQ by applying a $100\,\mu$s gate to the incoming beam. The amplitude of the signal induced on an MCP by the cooled ion bunch was then measured as a function of the storage time. The longitudinal trap was formed using the same 7 V DC gradient described in the previous two sections with the voltage on the last (24) electrode raised to 6 V above the high voltage bias. The radial trap was formed by applying $60\,V_{pp}$ RF at 1.15 Mhz. The ions were extracted by applying a ± 30 V kick to electrodes 22 and 24. The buffer gas pressure was held at 4.5×10^{-3} mbar. For lithium in hydrogen no appreciable difference in the amplitude of the signal was noted for storage times up to 30 ms. The results for lithium in helium are shown in figure 3.40. A clear decay in the amplitude of the extracted pulse was observed with half-life $t_{\frac{1}{2}} = 5.7 \pm 0.1$ ms.
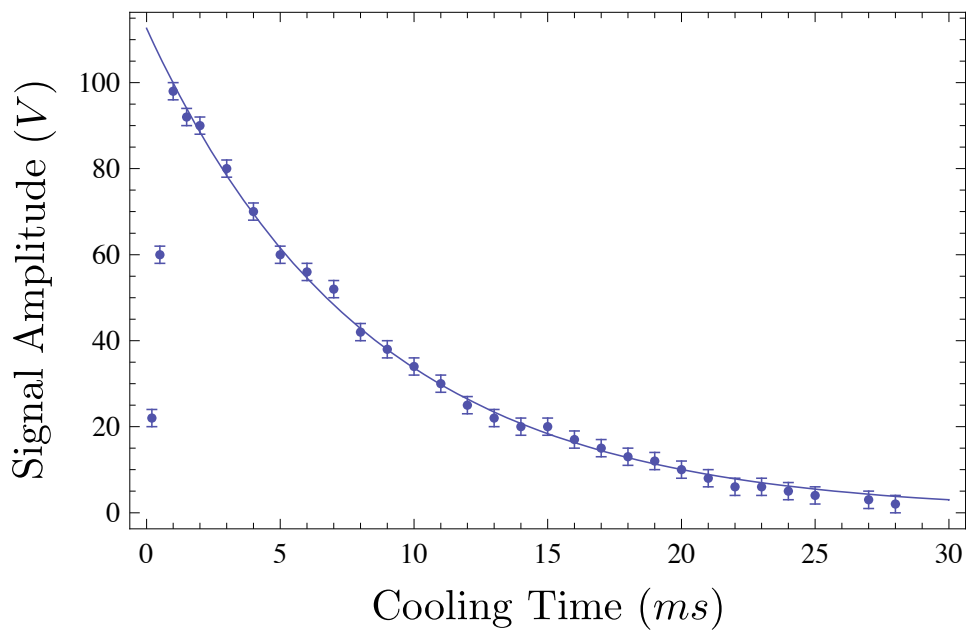
Figure 3.40: Amplitude of the signal induced on the MCP for lithium ions in a helium buffer gas as a function of cooling time.

3.4 Summary

The theory of a square-wave driven linear Paul trap has been presented and combined with a simple viscous drag model. It has been shown how the an ion beam can be cooled and bunched in such a device. A design for a new set of deceleration optics have been presented which can decelerate a $40\,\pi\,\mathrm{mm}\,\mathrm{mrad}$ beam from $60\,\mathrm{keV}$ to $10\,\mathrm{eV}$ without significant change in its transverse phase space profile. A description of the experimental set-up of the TITAN RFQ in the ISAC hall was given including test ion source, high voltage cages, gas feed system, square-wave-driver, injection and extraction optics, beam detection and beam diagnostics. Some results from off-line testing were presented including DC efficiencies, pulse widths and storage times. It was observed that lithium ions could be most efficiently cooled using a H_2 buffer gas, with up to 40% DC efficiency demonstrated. The use of hydrogen as a buffer gas was also observed to result in significantly increased trapping times. A study of the extracted pulse widths showed that extremely short pulses, $30\,\mathrm{ns}$ FWHM, were achievable. However, use of a pulse drift tube to reduce the ions longitudinal energy was seen to significantly deteriorate the quality of the ion bunches.

Chapter 4

Lithium Mass Measurements and Data Analysis

In this chapter I present the results of the mass measurements of ^{8,9,11}Li. First a description of the experimental set-up including the Penning trap and injection optics is given. The results and analysis procedure are then described including estimates of systematic error. Finally a new value for the two neutron separation energy of ^{11}Li is calculated and compared to the other existing experimental results.

4.1 Experimental Set-up

4.1.1 Beam Transfer

In section 3.2.6 the extraction and re-acceleration optics for the ion bunches that had been cooled in the RFQ were described. Figure 3.33 shows the extraction optics and the subsequent ion optics used to bring the cooled ion bunches up onto the ISAC platform. The transport optics between the RFQ and the Penning trap were designed for a maximum beam energy of $5\,\mathrm{keV}$, with transport typically carried out at $1\,\mathrm{keV}$. At this low energy it was possible to use a simple combination of Einzel lenses to bring the beam into the strong magnetic field of the Penning trap. The layout of these lenses is shown in figure 4.1.

4.1.2 Lorentz Steerer and Pulsed Drift Tube

In section 2.2.4 a possible method for preparing the ions for a measurement in the Penning trap was described, whereby the ions were injected into the Penning trap without any initial radial amplitude. A pure magnetron oscillation was then excited by the application of a dipolar RF field. This method is currently in use at most Penning trap mass spectrometers worldwide. However, when working with very short lived ions it is not always desirable to apply such an excitation. This is because it takes a finite amount of time,
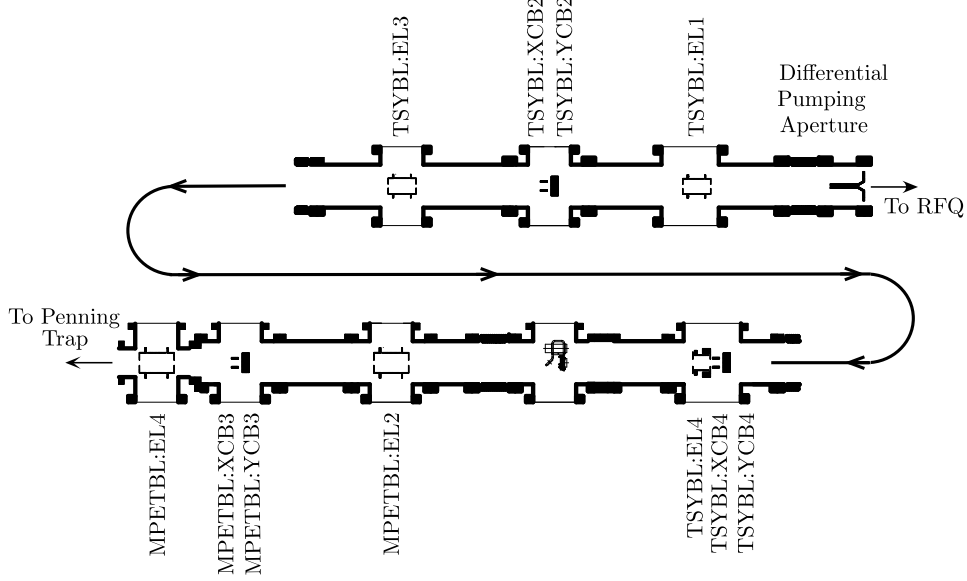
Figure 4.1: The low energy transfer line (MPETBL) between the RFQ and the Penning trap.

typical a few milliseconds, which subsequently reduces the time available for the mass measurement itself. The Lorentz steerer is a solution to this problem, initially developed by the LEBIT group at MSU [168, 169], whereby the dipolar excitation is applied electrostatically outside the Penning trap but still inside the strong magnetic field.

The layout of the injection optics for the TITAN Penning trap is shown in figure 4.2. As the ions enter the magnetic field they are manipulated electrostatically using a series of drift tubes. The ions first enter a wide drift tube in an area of weak magnetic field. As the field strengthens the beam is compressed hence a narrower drift tube can be used. A tapered drift tube that follows the longitudinal gradient of the magnetic field is used to obtain a smooth transition between the wide and the narrow tubes. The ions then enter the Lorentz steerer. The steerer is formed by segmenting a drift tube into four pieces. By applying a small voltage, $\pm\delta v$, across the steerer a crossed magnetic and electric field is set-up and the ions obtain an initial magnetron motion before entering the Penning trap.

Following the Lorentz Steerer the beam is decelerated to a few tens of electronvolts using a simple drift tube electrostatically biased slightly below the beam energy. Once the ions are inside the tube its potential is switched
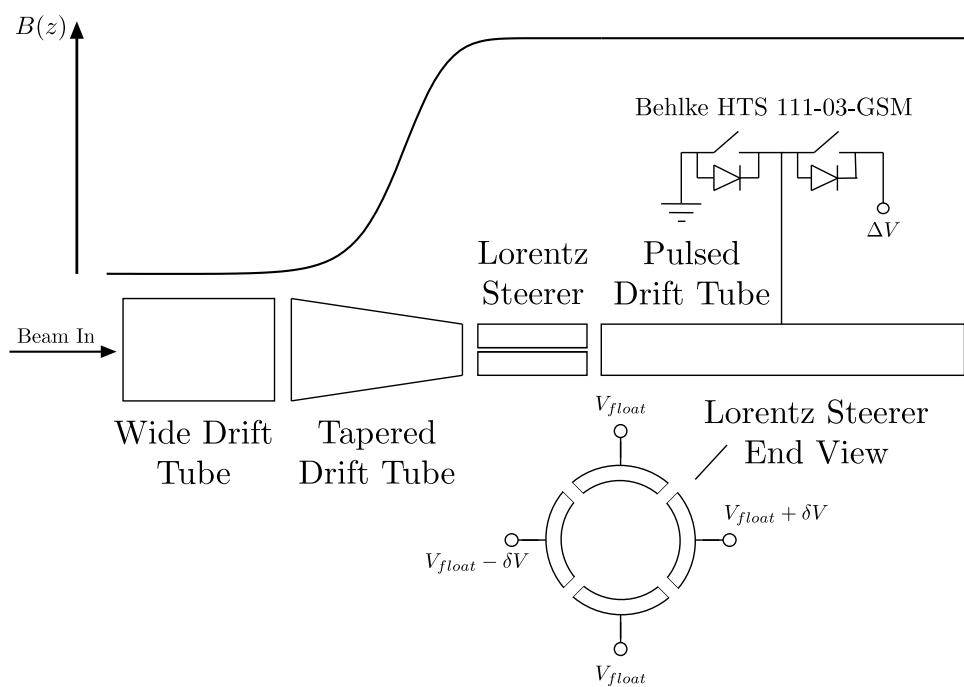
Figure 4.2: The ion optics for beam injection into the Penning trap.

down to ground in a manner similar to the pulsed drift tube described in section 3.2.6. Thus the ions enter the Penning trap at ground potential with a very low kinetic energy, $E \approx 10 \, \text{eV}$.

4.1.3 Penning Trap System

The Penning trap electrode geometry is shown in figure 4.3. Alongside the usual ring and end-cap electrodes this includes a pair of correction electrodes in order to compensate for imperfections in the axial harmonic potential created by the apertures in the end-cap electrodes (required for injection and extraction) and a pair of guard electrodes to compensate for the deviation in the radial electric field caused by the finite truncation of the trap electrodes. Each guard electrode was also segmented into four pieces to allow for the application of both dipole and quadrupole RF excitations. This kind of segmentation is unique to the TITAN Penning trap. At all other traps the ring electrode is segmented to allow for the application of excitations. The trap electrodes were made from oxygen free copper, as were the drift-tubes described in the previous section. The trap electrodes were also gold plated so as to ensure a constant potential across their surfaces and to reduce the effects of out-gassing which could cause a relatively high vacuum in the trapping region.

The magnetic field was provided using a custom built super-conducting magnet from American Magnetics, with a Helholtz configuration. The magnet was designed for a maximum field strength of 4 Tesla and a maximum operable strength of 3.7 Tesla was established. Cooling of the magnet coils was achieved using baths of both liquid helium and liquid nitrogen. The injection, extraction and Penning trap electrodes were all mounted in a long titanium vacuum chamber. This chamber was machined so as to fit into the room temperature bore of the super-conducting magnet. Room temperature shim coils were used to correct for any magnetic field inhomogeneity in the trapping region.

The vacuum in both the MPETBL and the Penning trap itself was provided using Varian V551 500 l/s turbo-molecular pumps backed with Varian Turbo-V 81 70l/s turbo-molecular pumps, these in turn were backed with Varian PTS 300 Scroll pumps. Thus a vacuum on the order of 1×10^{-10} mbar was routinely available in the MPETBL. A Varian Vacion plus 300 ion pump was also used on the Penning trap chamber so as to lower the pressure to 1×10^{-11} torr. The actual pressure inside the trap centre is unknown however storage and excitation times of 2 s were established without significant interaction with background gas. This is a factor of four times longer than
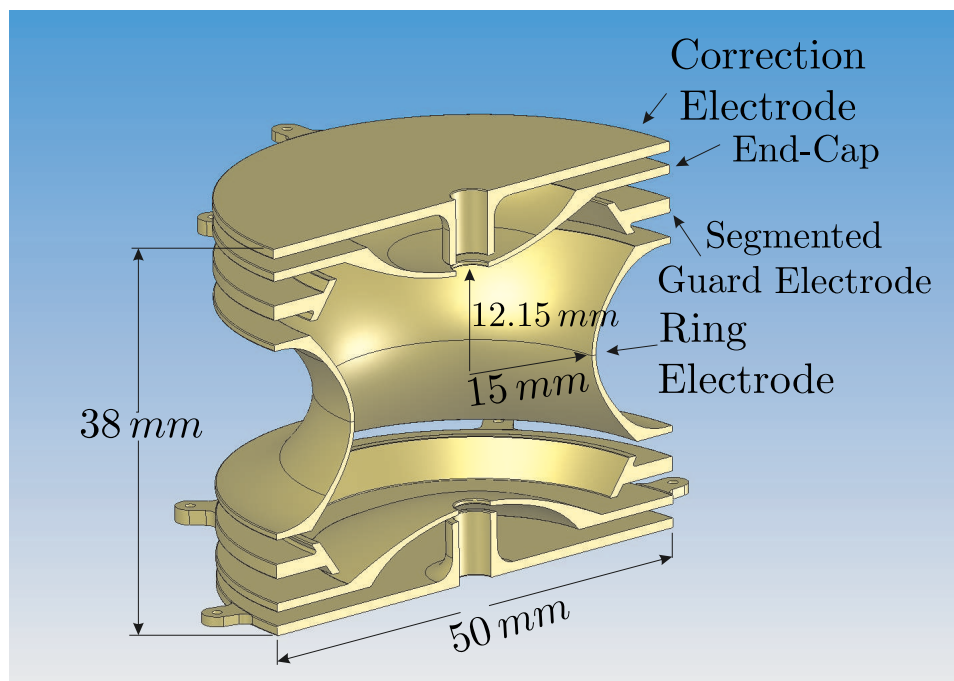
Figure 4.3: Rendered drawing of the Penning trap electrodes.

any excitation applied for the measurements in this thesis.

4.1.4   Extraction and Detection

Extraction of the ions from the Penning trap was achieved by pulsing the voltage applied to its end-cap electrodes. This extraction signal was also used to start a clock which measured the time taken for the ion to reach the MCP. Upon extraction the ions entered a series of drift tubes which guided the ions out of the strong magnetic field. As they drifted through these tubes the ions radial kinetic energy was converted into longitudinal kinetic energy resulting in the desired time of flight effect as described in section 2.2.3. The magnetic field gradient was strongest inside the tapered drift tube, hence the voltage applied on this tube was critical in defining the amplitude and width of the observed time-of-flight spectrum [41]. The ions were subsequently accelerated into a drift tube, to an energy on the order of $1\,\mathrm{keV}$ before passing through an Einzel lens such that they were focused onto a chevron stack MCP detector. The signal induced on the MCP stopped the clock and the time of flight was recorded.
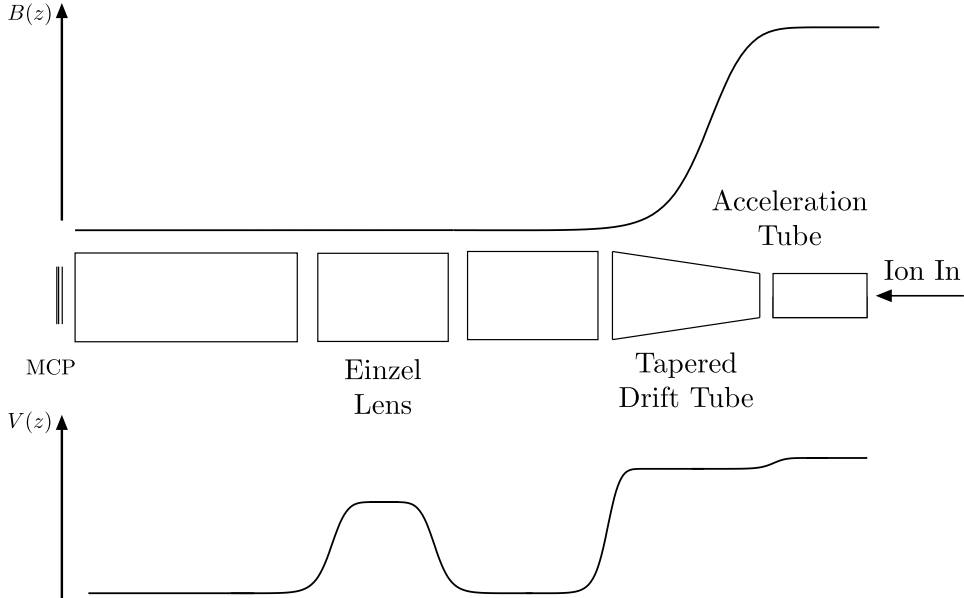
Figure 4.4: The ion optics for ion extraction from the Penning trap.

Parameter	Unit	Description
Centre	Hz	Central frequency of the fitted distribution
ρ_-	mm	Initial radius of the magnetron motion
ρ_+	mm	Initial radius of the reduced cyclotron motion
Conv		Percentage completion of the conversion process
ADamp	Hz	A damping coefficient to take into account the ions interaction with any background gas
TRF	s	The length of the quadrupole excitation
TofOff	μs	Difference between the base-line time of flight and the peak of the resonance

Table 4.1: Possible fitting parameters in EVA.

4.2   Data Analysis and Systematic Error Budget

4.2.1   Analysis Procedure

The data was analysed using the package EVA which is currently maintained by S. Schwarz at MSU. The basic function of the package is to fit the time of flight curves obtained from the Penning trap mass spectrometer. Two types of fit can be carried out. In the first a simple Gaussian is fit to the central peak of the spectrum. This is useful for obtaining a quick estimate of the position of the centroid. The second fit is somewhat more complicated. In chapter two we saw that the time of flight between the Penning trap and the MCP could be written as:

$$T(E_r) = \int_{z_0}^{z_1} \sqrt{\frac{m}{2(E_0 - qV(z) - \mu(E_r)B(z))}}\, dz, \qquad (4.1)$$

where E_0 is the initial energy of the ion, q is its charge, $V(z)$ is the electrostatic potential along the ion's path, $B(z)$ is the magnetic field strength along the ion's path, $\mu(E_r)$ is the ion magnetic moment, z_0 is the initial position of the ion and z_1 is the position of the particle detector. EVA can carry out a time of flight fit to the data using this function. It takes as an input quadratic approximations to the longitudinal electric and magnetic field strengths. The missing ingredient is the radial energy of the ions which in itself is a function of a number of parameters including the central frequency. This gives a more reliable fit to the data because it also includes the side bands of the characteristic time of flight spectra. This kind of fit is often referred to as a MIKE fit after M. König who pioneered its use [110]. A full list of available fitting parameters is given in table 4.1.

Figure 4.5 shows results from a typical ^{6}Li data set that has been analysed with EVA. The program produces a number of different plots from the data two of which are shown. The first, on the left, shows the data binned by time of flight. It can be seen for ^{6}Li that the data falls within a fairly narrow window from 20 to $60\,\mu$s. For low statistics measurements random events such as dark counts on the MCP detector can shift the measured cyclotron frequency. Hence, it is usual to exclude events that fall outside of this time of flight window. EVA also calculates a suggested statistical error bar for the time of flight resonance as the standard deviation of the binned time of flight data:

$$\sigma_{stat} = \sqrt{\frac{1}{N} \sum_i N_i (t_i - \bar{t})^2}, \qquad (4.2)$$

Where N_i is the number of counts in each time of flight bin, t_i. This error is applied equally to all data points in the time of flight resonance and so doesn't effect the value obtained for central frequency from the fitting routine. However, an over-estimation of the error bar will lead to unnecessary uncertainty in the final result. Thus it is desirable to remove events that are unlikely to be part of the real data, not only because they can shift the centre frequency, but also because they can artificially inflate the statistical error. This is achieved by selecting data obtained within a specific time of flight window. In fact for all the data presented, the selection process was found to shift the central frequency by an insignificant amount when compared to the statistical error from the fit. However, excluding data at higher times of flight was observed to reduce the final uncertainty in the fit by up to a factor of two.

Once the selection was made a fit was carried out to the resonant spectra. For measurements carried out using the same initial settings it is reasonable to expect a number of the parameters listed in table 4.1 be consistent across all the data sets. For each data set preliminary fits were carried out in which all parameters, except for the damping constant which was always assumed zero and the RF excitation time which was known, were allowed to vary. For each data set consistent values for the conversion factor and initial reduced cyclotron radius were found. The fits were then redone holding these parameters constant. The final fits then yielded values for the central frequency, the initial magnetron radius and the time of flight offset. The second plot, on the right, in figure 4.5 shows a fit to a typical time of flight resonance for ^{6}Li taken with an excitation time of $498\,$ms. The values for the initial magnetron radii were then used to calculate a systematic error
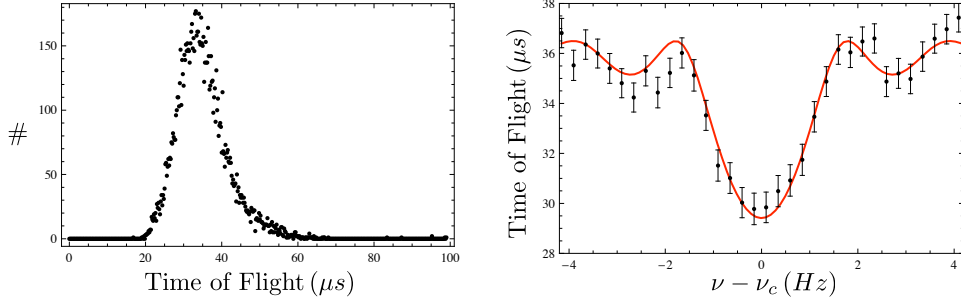
Figure 4.5: A typical ^{6}Li data set showing a time-of-flight histogram (left) and the a resonant spectra (right). The solid line is a fit to the data with the expected line shape, the fit returns a value for $\nu_c = 9450899.16(3)\,\text{Hz}$.

associated with relativistic effects, this is discussed further in section 4.2.5 .

The results from the EVA fits were then input into the program SOMA (Simple Online Mass Analysis) written by R. Ringle [168]. The program takes results for both the reference and the measured ions. First the reference frequency at the time of each measurement, ν_r, is calculated using a linear interpolation between the references taken before and after the measurement. The ratio, r, of this frequency to the measured frequency, ν_m, is then used to calculate the atomic mass, m, as:

$$r = \frac{\nu_r}{\nu_m}, \tag{4.3}$$

$$m = r(m_r - m_e) + me, \tag{4.4}$$

where m_r is the atomic mass of the reference ion, and m_e is the electron mass. The first ionisation potential for the atomic electrons can also be included which for lithium is $5.4\,\text{eV}$ [170].

4.2.2 Magnetic Field Drift

A possible source of error in a Penning trap mass measurement comes from changes in the magnetic field between references. The field produced by the super-conducting magnet has a very slow exponential decay due to a phenomena known as flux creep [171, 172]. This decay is so slow, typically $\delta B/B \approx 1 \times 10^{-9}/h$, that it is approximately linear over relatively long periods of time (years). Thus the linear interpolation carried out by SOMA to find the magnetic strength at the time of the measurement is justified. However, deviations from this ideal linear behaviour do also occur caused

for example by variations in the atmospheric temperature/pressure around the magnet. Changes in pressure affect the boil-off rate, and hence the temperature, of the liquid helium used to cool the super-conducting coils. The change in temperature can cause changes in the magnetic permeability of the insulating materials used in the construction of the magnet and hence changes the magnetic field [173]. Changes in the room temperature may also change the permeability of the material surrounding the Penning trap, i.e. the vacuum chamber, support structure etc., which in turn can cause slight variance in the magnetic field inside the magnet's bore.

A number of studies have been carried out at other facilities to try and reduce the magnitude of such effects. At ISOLTRAP where magnetic fluctuations as large as $\delta B/B = 5 \times 10^{-8}$ had been observed the frequency of ^{85}Rb ions were measured over a period of days whilst the temperature of the room temperature bore was also recorded [41]. The results showed a linear correlation between the temperature and the variation in the field, showing that temperature dependant phenomena could account for the observed variations in the magnetic field. A number of traps now use a stabilisation system to maintain the pressure of the liquid helium. This has proven to reduce magnetic field fluctuations to the order of 1×10^{-9} (see for example [173]). Such a system is also planned for TITAN however it was not installed while these lithium measurements were carried out.

More dramatic changes in the magnetic field of the TITAN Penning trap, on the order of $\delta B/B = 1 \times 10^{-7}$ were observed to occur when the large crane in the ISAC hall was moved over the Penning trap. This is because the ferromagnetic steel used in the construction of the crane itself becomes magnetised. This field from the crane in turn modifies the field from the magnet. Hence during the online run the crane was locked in position at the far end of the ISAC hall. A shift on the same order of magnitude was also observed associated with the electromagnets for the TRIUMF cyclotron coming off-line. However, this occurrence would be easily apparent during an on-line run due to loss of the proton beam.

Throughout the online run the cyclotron frequency of ^{6}Li was measured at approximately two hour intervals to serve as the reference for the mass measurements. The results of these measurements are shown in figure 4.6. A linear fit to the data gives the field decay rate as:

$$-\frac{1}{B}\frac{dB}{dt} = 0.20(1) \times 10^{-8}/h, \qquad (4.5)$$

the maximum duration of any single measurement during the run was one hour introducing a systematic error of $\delta m/m = 2 \times 10^{-9}$. The fit residuals
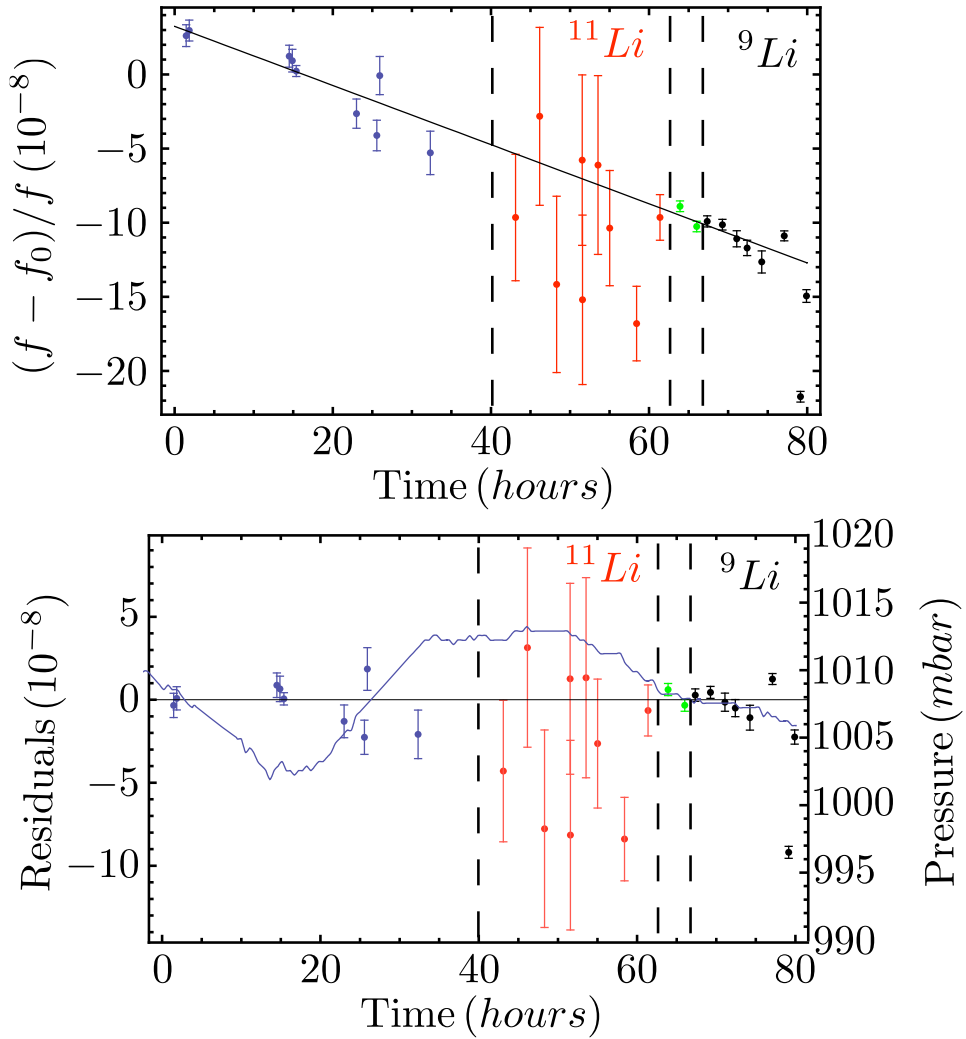
Figure 4.6: A linear fit to measurements of the cyclotron frequency of ^{6}Li over the period of data taking for the measurements presented in this thesis. Here f_0 is somewhat arbitrarily taken to be 9450900 Hz. Also shown are the fit residuals with the atmospheric pressure measured at a local weather station overlaid.

are also shown in figure 4.6 alongside the atmospheric pressure as measured at a local weather station. The plot has been divided into sections, the first section contains measurements taken before the online data taking began, the second section shows the reference measurements for the ^{11}Li data, the third the references for ^{8}Li and finally the forth section contains the references for ^{9}Li. The plot of the residuals has a number of interesting features.

1. The data for the atmospheric pressure can be seen to reproduce the observed trend in the fit residuals for both the ^{9}Li and the ^{8}Li data. However, there are two points in the ^{9}Li data which show large deviation from the other residuals. During the online run the gas bottle in the RFQ ran low and had to be replaced. This is a fairly involved procedure because the gas bottle sits at high voltage. The two wayward data points were taken just after the gas bottle was replaced. It is possible that following this procedure one of the numerous parameters for either the RFQ or the Penning trap was set incorrectly leading to these errant points. As the exact cause of this fluctuation is unknown the data was analysed both with and without the data taken after the gas bottle was changed. The final result of which is discussed further in section 4.3.

2. The reference data for the ^{11}Li measurements is seen to oscillate between high and low values. The difference between the values corresponds to a shift in the measured frequency of approximately $1\,\text{Hz}$. The atmospheric pressure data would also seem to suggest that the residuals should be constant over this period of time. After the run a study of the Penning trap was carried out using both ^{12}C and ^{6}Li. For a combination of large initial cyclotron frequency plus large numbers of ions in the trap the measured cyclotron frequency was reduced by approximately $1\,\text{Hz}$. This was found to be due to the saturation of the MCP detector distorting the measurement. The data was thus analysed both including and excluding the low lying reference points.

3. There are three reference points taken about fifteen hours into the run that are not well reproduced by the atmospheric pressure data. The exact cause of this shift is unknown however the data points followed a major power surge in which a number of devices electrical/magnetic devices were brought off-line. Although the magnet has active shielding to try and reduce the amount of interference from external devices on the field produced, shifts in the magnetic field had previously been observed following similar incidents.

SOMA takes a linear interpolation between successive frequency measurements to calculate the reference frequency at the time of the measurement. However, as we have seen non linear effects can occur. An upper limit on such effect was calculated using the reference measurements for the ^{8}Li and the ^{9}Li measurements (only the data before the RFQ's gas bottle was changed). A linear interpolation between the first and last data points spanning a period of over ten hours was taken. The RMS deviation of the actual data from the line was then calculated. This was found to correspond to an uncertainty of $\delta m/m = 7 \times 10^{-9}$ which was included as an additional systematic. This is a conservative estimate of the error associated with such effects as the maximum time between successive reference measurements was only three hours not ten.

4.2.3   Non-ideal trapping Potentials

Frequency shifts can arise from imperfections in the trapping potential. There are three main source of these kinds of shift [125]:

1. Deviations from the ideal quadrupolar electrostatic field. Such deviations can arise due to the finite truncation of the trap electrodes, the introduction of holes in the end cap electrodes for the injection/extraction of ions and misalignment of the trap electrodes with respect to one another. The compensated trap design used at TITAN allows to correct for some of these effects. However, some residual octupole and dodecapole fields are inevitable. Such fields cause a shift in the measured mass which scales linearly with the mass difference between the reference and the measured ion:

$$\frac{\delta m}{m} = \frac{\delta \omega}{\omega} \frac{(m - m_{ref})}{m}.$$ (4.6)

2. Magnetic field inhomogeneity. If the magnetic field is not constant over the whole trapping region the ion will see a varying field strength as its motion is converted from magnetron to reduce cyclotron. If the reference and the measured ion start with different initial magnetron radii, or different axial amplitudes, this can lead to a shift in the measured frequency. Such a shift is to first order mass independent.

3. Misalignment of the trap axis with respect to the magnetic field. This leads to a shift in the frequency which for small angles is proportional to the square of the angle between the trap and field axis [111]. Again this shift is mass independent.

Electrode	Ideal Setting (V)	Actual Setting (V)
Correction	3.14	2.8
End-Cap	2	2
Guard	0	0.1
Ring	0	0

Table 4.2: Penning Trap Electrode Voltages

To look at the effects of such shifts both the masses of ^{7}Li and ^{12}C were measured using the TITAN Penning trap. The best agreement between the measured and the literature values for the frequency ratio of ^{7}Li to ^{6}Li was found with the trap settings as shown in table 4.2. This showed some deviation from the ideal settings consistent with e.g. misalignment of the ring and the end-cap electrodes by 1 thousandth of an inch (0.03 mm) [174]. However, with this configuration the frequency ratio of ^{7}Li to ^{6}Li was found to agree with that measured at SMILETRAP at the 7×10^{-9} level (46 eV) [175]. Using the same configuration the mass excess of ^{12}C was measured to be 0.8(4) keV. These were preliminary measurements carried out with a short excitation time. Hence it is expected that these results will be improved by further data taking. Due to the comparatively large shift compared to the ^{7}Li result this shift is mass dependant and hence predominately due to deviations from the ideal electric field.

With further study and the measurement of a wide range of well known masses a better understanding of the magnitude of the different types of frequency shift will be obtained. However, due to the preliminary nature of the ^{12}C result its outer limit was used to calculate the maximum magnitude of the possible mass dependant shift. This was then taken as a systematic error for the lithium measurements as shown in table 4.2.3. It can be seen that the predicted shift for a mass seven ion is over three times bigger than that observed. In fact the ^{7}Li result is compatible with the lower limit of the carbon mass excess. Thus these uncertainties are almost certainly over estimates which will be improved by further studies of the trap.

4.2.4 Contaminant Ions and Multiple Trapped Ions

Confinement of multiple ions in the trap can lead to a frequency shift caused by their Coulomb interaction. Such effects have been well studied at other trap facilities [110, 176]. In general if the ions are of the same species this leads to a force that acts on the centre of mass of the ion cloud and as such no frequency shift is observed. However, if two or more ions of differing

Mass (u)	δm (keV)	$\delta m/m$
7	0.2	3×10^{-8}
8	0.4	5×10^{-8}
9	0.6	7×10^{-8}
11	1	1×10^{-7}
12	1.2	1×10^{-7}

Table 4.3: Extrapolated Mass Dependant Shifts

mass are confined then a frequency shift can occur. This effect has been seen to linearly increase with the number of trapped ions. Possible sources of contamination in the data presented are:

1. Contaminant ions from the ISAC source. In general the resolving power of the mass separator may not be good enough to deliver an ion beam that is isobarically pure. However, previous experiments at TRIUMF had shown that the lithium beams produced were practically free of contamination.

2. Chemistry inside the RFQ. Chemical effect in the RFQ may lead to the generation of unwanted contaminants. However, off-line tests with ^{6,7}Li showed that these effect were negligible when using ^{2}H as the buffer gas.

3. Decay Products. Although decay of trapped radioactive species is a possible source of contamination, the energy associated with the decays are typically much higher than the depth of the trapping potential. As such the probability of such products remaining in the trap is expected to be low.

For large numbers of trapped ions the effect of contamination can be probed by analysing the data with different numbers of hits on the MCP. The true cyclotron frequency is then found from a linear extrapolation to the result for a single ion in the trap [177]. However, for all the data presented in this thesis the number of ions injected into the trap was kept low such that the number of hits on the MCP was typically in the range of 1 to 2 hits per cycle, except for the ^{11}Li data where the count rate was much lower. Hence, there was not enough data at higher counts to perform the linear extrapolation. However, typical data sets for ^{8}Li and ^{9}Li were re-analysed excluding data with more that two hits on the MCP. No shift in the central frequency was observed that was not well contained within the statistical uncertainty on

Species	$\bar{\rho}_-$ (mm)	$(r - r_{rel})/r_{rel}$	$\delta m/m$
^{6}Li @ $2\,Hz$	0.22(1)		
^{8}Li @ $2\,Hz$	0.20(1)	$5(1) \times 10^{-10}$	6×10^{-10}
^{9}Li @ $2\,Hz$	0.21(1)	$6(1) \times 10^{-10}$	7×10^{-10}
^{6}Li @ $50\,Hz$	0.38(1)		
^{11}Li @ $50\,Hz$	0.46(1)	$2.7(1) \times 10^{-9}$	3×10^{-9}

Table 4.4: Systematic shift due to relativistic effects

the fits. Hence, the systematic uncertainty due to contaminant ions was seen to be negligible.

4.2.5 Relativistic Corrections

For extremely high precision Penning trap measurements, e.g. on stable species with $\delta m/m \approx 1 \times 10^{-10}$, it is usual to use a reference ion with near identical mass to the measured ion, i.e. a mass doublet. In this case the reference and measured ions have the same velocity, assuming identical initial magnetron radii, and hence any relativistic effects will cancel out. However, the measurements presented in this thesis were not made using mass doublets and hence relativistic effects do occur. The magnitude of such effects can be calculated by relating the measured frequency ratio, r_{rel}, to the non-relativistic frequency ratio, r, using:

$$r_{rel} = \frac{\gamma_r}{\gamma_m} r = \frac{\gamma_r}{\gamma_m} \frac{\nu_r}{\nu_m}, \tag{4.7}$$

where γ_r and γ_m are the Lorentz factors for the reference and the measured ions respectively. These Lorentz factors can be calculated using the initial magnetron radii and the cyclotron frequencies from the fits carried out in EVA where:

$$\gamma = \frac{1}{\sqrt{1 - \frac{(2\pi\nu\rho_-)^2}{c^2}}}. \tag{4.8}$$

The average initial magnetron radii for both the reference and measured lithium ions is shown in table 4.2.5 alongside the calculated shift in the frequency ratio. The upper limit of these shifts was then used to calculate a systematic error for each radioactive lithium species which is also given. In all cases any systematic error due to relativistic effects can be seen to be negligibly small for the current precision.

Facility	$m\,(u)$	$\Delta\,(\text{keV})$
SMILETRAP	6.015122890(40)	14086.882(37)
JILA-TRAP	6.015122795(16)	14086.793(15)
AVERAGE	6.015122808(15)	14086.807(14)

Table 4.5: ^{6}Li Reference Masses

4.2.6 Reference Mass

The AME2003 result for the mass of ^{6}Li was based on a measurement on a single Penning trap mass measurement at the now defunct JILA-TRAP experiment previously at the National Institute of Standards and Technology, USA [92]. As previously a mentioned a more recent Penning trap mass measurement has also been carried using SMILETRAP [91]. The two results are summarised in table 4.2.6 . It can be seen that the two results disagree at the 1.5×10^{-8} level, just outside their one standard deviation error bars. As such the weighted average of the two results, as shown, has been used as the reference for the measurements in this thesis.

4.3 On-line Results

The following data was taken over a period of three days, from December 12 to December 14, 2007, using surface ionised lithium beams produced with a $75\,\mu\text{A}$, $500\,\text{MeV}$ proton beam from the TRIUMF cyclotron impinging on a tantalum target. The ISAC beam was extracted at an energy of $20\,\text{keV}$ and then cooled and bunched in H_2 using the TITAN RFQ. The initial tune into the RFQ was obtained using a ^{7}Li pilot beam, a maximum DC efficiency of 60% was observed suggesting that the ISAC beam emittance was better than that from the test ion source. During the run the target-surface ion source system was operating at less than ideal conditions with a maximum yield of $3000\,^{11}$Li per second. Much higher yields of ^{8,9}Li were available. In fact both beams had to be attenuated using slits in the ISAC separator system so as to not operate the RFQ at the space charge limit. The Penning trap was operated with a $2\,\text{V}$ well depth, with correction electrode settings that which were found during previous off-line measurements. All the measurements were made with respect to the mass of ^{6}Li, with the masses calculated using the weighted average of the two available high precision Penning trap measurements of its mass (see section 4.2.6).

^{8}Li Measurements

Three independent ^{8}Li measurements were carried out over a period of two hours. For these measurements the trap was operated with a 2 Hz duty cycle allowing for an excitation time of 498 ms. Data was collected at forty one, equally spaced values for the excitation frequency in the range 7085950 ± 5 Hz. Before analysis the data was selected inside the time of flight window $20\,\mu$s to $70\,\mu$s as discussed in section 4.2.1. A ^{8}Li resonance is shown in figure 4.7 alongside the three results for the central frequency. To check for consistency the Birge ratio, R, of the data points was calculated where [178]:

$$R = \frac{\sigma_{out}}{\sigma_{in}}. \tag{4.9}$$

The outer error, σ_{out} gives a measure of the fluctuation of the data around the mean value:

$$\sigma_{out} = \sqrt{\frac{\sum_i \frac{1}{\sigma_i^2}(r_i - \bar{r})}{(N-1)\frac{1}{\sum_i \frac{1}{\sigma_i^2}}}}, \tag{4.10}$$

where r_i is the ratio of the measured to the reference frequency for each point, σ_i is the error associated with the ratio r_i, N is the number of data points and $\bar{r}$ is the weighted average of r_i:

$$\bar{r} = \frac{\sum_i \frac{r_i}{\sigma_i^2}}{\sum_i \frac{1}{\sigma_i^2}}. \tag{4.11}$$

The inner error, σ_{in}, is that of this weighted sum:

$$\sigma_{in} = \sqrt{\frac{1}{\sum_i \frac{1}{\sigma_i^2}}}. \tag{4.12}$$

The error in the Birge ratio can also be calculated and scales with the root of the number of data points:

$$\sigma_R = \frac{0.4769}{\sqrt{N}}. \tag{4.13}$$

This Birge ratio gives an indication of whether or not any variance in the experimental data is due purely to statistics or if there is some unknown systematic in the data. A Birge ratio of 1 means that the data spread is purely statistical. A ratio greater than one suggests the existence of an unknown systematic e.g. a Birge ratio of 1.67 would suggest that there is

$\bar{r}$	Δ_{TITAN} (keV)	Δ_{AME03} (keV)	Δ_{SMILE} (keV)
0.7497657756(32)	20945.70(38)	20946.844(95)	20945.799(65)

Table 4.6: ^{8}Li frequency ratio and experimental value for the mass excess. The error in the frequency ratio is purely statistical, the error in the mass excess includes a 380 eV systematic. Also shown are the AME03 values for the mass excess and the result obtained using the recent SMILETRAP value for the mass of ^{7}Li

a 67% chance that the variance is not statistical in nature. A Birge ratio of less than one could suggest that the error bars have been overestimated. For the ^{8}Li data the three measurements are in good agreement with each other with a Birge ratio of 0.92(27).

Figure 4.7: A typical ^{8}Li measurement where $\nu_c = 7085960.71(7)$ Hz (left). Deviation of the three points from the weighted average of the results where the solid lines show the error in the weighted mean (right). All three results can be seen to be in good agreement.

The final result for the ^{8}Li mass excess, Δ, is given in table 4.6 alongside the AME value [24]. The AME mass of ^{8}Li was obtained from the Q-vlaue derived from the reaction ^{7}Li(n, γ)^{8}Li which was then added to the ^{7}Li mass. Also listed is the mass of ^{8}Li calculated using the recent SMILE-TRAP ^{7}Li mass measurement. The error in the given value of $\bar{r}$ is purely statistical whereas the error in the mass excess includes a systematic error of 380 eV ($\delta m/m = 5 \times 10^{-8}$). The 1 keV deviation from the AME value is not surprising and is due to the recently discovered 1 keV correction to the mass of ^{7}Li [91], this is reflected in the good agreement with the mass excess calculated using the new SMILETRAP result. It is of note that the value for the mass excess shows a shift of 100 eV when compared to the SMILETRAP result. This is larger than the statistical error bar. Like the

[7]Li result this again corresponds to the lower limit of the mass dependant shift as calculated using the ^{12}C data.

[9]Li Measurements

Six separate measurement of the mass of [9]Li where made over a period of eight hours. The Penning trap was run at a frequency of $2\,\mathrm{Hz}$, again with an excitation time of $498\,\mathrm{ms}$. The half-life of [9]Li is only $178\,\mathrm{ms}$, however the ISAC beam current was more than sufficient to compensate for any losses due to radioactive decay. Data was collected at forty one frequency steps in the range $6297542 \pm 5\,\mathrm{Hz}$. Before analysis the [9]Li data was selected inside the time of flight window $30\,\mu\mathrm{s}$ to $80\,\mu\mathrm{s}$. A typical [9]Li resonance is shown in figure 4.8 alongside the six results. The Birge ratio for all six results is $1.74(19)$ suggesting a 74% probability that the spread in the data is not statistical. However, removal of data taken after the RFQ gas bottle was exchanged reduces the Birge ratio to $1.38(23)$. The results both with and without the two data points taken after the gas bottle ran out are shown in table 4.3. The errors in the numbers are purely statistical except for the final value for the mass excess which includes a systematic error or $600\,\mathrm{eV}$ $(\delta m/m = 7 \times 10^{-8})$. The truncated data set gives a result which is $49\,\mathrm{eV}$ higher than the full data set. This is on the limit of its statistical one sigma error bar. Due to the improved Birge ratio of the truncated set the final value was taken as this result. The $49\,\mathrm{eV}$ difference between the two values was then added linearly into the final error.
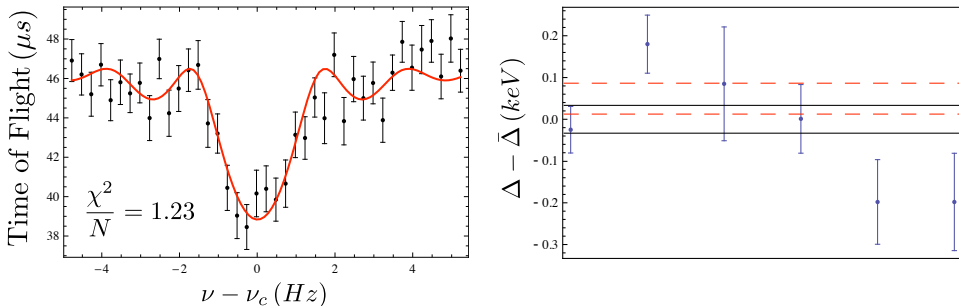
Figure 4.8: A typical [9]Li measurement where $\nu_c = 6297541.77(8)\,\mathrm{Hz}$. Deviation of the six points from the weighted average of the results where the solid lines show the error in the weighted mean (right). The dashed lines show the limits on the weighted mean calculated excluding the last two data points. The last two values appear to sit too low, this in turn pulls the weighted average down.

115

	R	$\bar{r}$	$\Delta\,(\text{keV})$
All Points	1.75(19)	0.6663431578(26)	24954.754(46)
Truncated Set	1.38(23)	0.6663431539(29)	24954.803(49)
Final		0.6663431539(68)	24954.80(60)
AME03			24954.3(19)

Table 4.7: Results for the frequency ratio and mass excess of ^{9}Li. Values are given both including and excluding data taken after the RFQ gas bottle ran out. The error in all the TITAN data is purely statistical, except for the error in the final mass excess includes a 600 eV systematic.

^{11}Li Measurements

A total of nine separate measurements of the mass of ^{11}Li were made over a fourteen hour period. Due to the short half-life, 8.8 ms, of ^{11}Li an excitation time of 18 ms was used, with the Penning trap operated with a 50 Hz repetition rate. Data was collected at 41 frequency steps in the range 5147350 ± 100 Hz. The extracted ions were detected at a rate of approximately $2000\,\text{h}^{-1}$, or $0.5\,\text{s}^{-1}$.
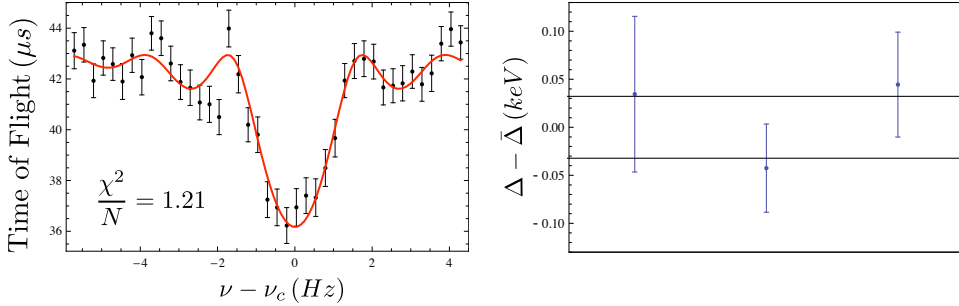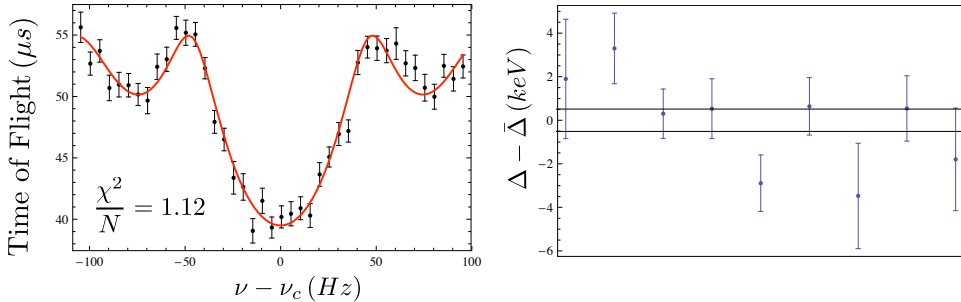

Figure 4.9: A typical ^{11}Li measurement where $\nu_c = 5147554.5(7)$ Hz. Deviation of the three point from the weighted average of the results where the solid lines show the error in the weighted mean (right).

The final results are shown in figure 4.9 alongside one of the nine resonant spectra. Only events in the time of flight window 30 to 80 μs were selected. All nine results are in good agreement with each other and have a Birge ratio of 1.26(16). The results obtained both including and excluding the four lower lying reference points are shown in table 4.8. Also shown is the value calculated by shifting the four low lying reference points up by 1 Hz. All three values agree within systematic errors and there is no significant

	R	$\bar{r}$	Δ (keV)
All Points	1.26(16)	0.544641766(27)	40728.08(52)
Truncated Set	1.16(19)	0.544641772(34)	40727.96(63)
Shifted Set	1.24(16)	0.544641741(27)	40278.55(52)
Final		0.544641766(27)	40728.1(12)
AME03			40797(19)
MISTRAL			40720.9(46)

Table 4.8: Values for the frequency ratio and mass excess of ^{11}Li. The error in all the TITAN data is purely statistical, except for the error in the final mass excess includes a 1 keV systematic.

change in the Birge ratio. The final value is just that calculated using all the unshifted data. Again, the errors in the results are purely statistical except for the final value for the mass excess which includes a systematic error or 1 keV ($\delta m/m = 1 \times 10^{-7}$). It can be seen that this new result is about four times more precise than the previous MISTRAL value. The value for the mass excess is slightly higher than the MISTRAL result but agrees with it within two of their error bars. The TITAN result shows a 70 keV difference from the AME03 value, i.e. greater than three standard deviations.

4.4 The two neutron separation energy of ^{11}Li

Using these new values for the masses of ^{9}Li and ^{11}Li a new value for the two neutron separation energy of ^{11}Li can now be calculated. This new value is shown in figure 4.10. The new TITAN result can be seen to agree with the measurements of Wouters et al. and Kobayashi et al. within one standard deviation. Agreement with the Bachelet et al., is achieved within two standard deviations. The Young et al. result is now seen to sit too low with agreement just outside of two standard deviations. The AME value is also low due to its predominant weighting on the Young et al. measurement.

In the first chapter the motivation for this new measurement of the mass of ^{11}Li was presented in terms of good metrology. It was shown that although two precision results had already been carried out, there was not good agreement between them. This is a good example of the distinction between precise and accurate results. Although both results were precise, meaning that they would both be repeatable with the same equipment, they could not both be accurate, meaning that one or both sets of equipment had

Reference	Year	Method	S_{2n} (keV)
Thibault et al. [54]	1975	Mass Spec.	170 ± 80
Wouters et al. [55]	1988	TOF	320 ± 120
Kobayashi et al. [56]	1991	$^{11}B(\pi^-, \pi^+)^{11}Li$	340 ± 50
Young et al. [57]	1993	$^{14}C(^{11}B, ^{11}Li)^{14}O$	295 ± 35
AME 2003 [24]	2003	Mass Evaluation	300 ± 20
Bachelet et al. [25]	2005	Mass Spec.	376 ± 5
TITAN	2007	Penning Trap	369.3 ± 1.3

Figure 4.10: Comparison of the newly measured value of the ^{11}Li two neutron separation energy to that of previous measurements.

some unknown systematic. With the new TITAN measurement this previous experimental discrepancy has now been resolved, with agreement between the MISTRAL and TITAN results, and a clearer picture of the mass and two neutron separation energy of ^{11}Li emerges. The impact of this measurement is then clear. The results from the charge radius measurements and the E1 transition strengths can now both be recalculated using the new mass. This will help to furnish a more consistent experimental picture of ^{11}Li which will in turn prove an excellent test of nuclear theory.

4.5 Summary

A description of the new TITAN Penning trap mass spectrometer has been given and results from the measurements of ^{8,9,11}Li presented. The masses were all found with an uncertainty equal or better than $\delta m/m = 1 \times 10^{-7}$. The limiting factor in the precision of the measurements is the mass dependant systematic uncertainty due to deviations from the ideal quadrupolar electric field. This uncertainty will be improved by further studies of the trap. The measurement of ^{11}Li sets a new record for the shortest lived isotope ever measured using Penning trap mass spectrometry with a half-life, 8.8 ms, over seven times shorter than the previous record (^{74}Rb, $t_{1/2} = 65$ ms) held by ISOLTRAP. Using the new measurements a value for the two neutron separation energy of ^{11}Li was calculated, $S_{2n} = 369.3 \pm 1.3$ keV with a precision over four times better than any previous result.

Chapter 5

Summary and Outlook

In early 2002 I first started work on the TITAN project. At this time I was charged with the initial design of a new RFQ cooler and buncher; the first stage of TITAN. In 2003 the project was officially funded by NSERC and work began on the design of the Penning trap. By late 2004 the RFQ was set-up on an off-line test stand, with full commissioning by the end of 2005. In 2006 the test set-up was dismantled and the RFQ moved to the ISAC hall. The new on-line set-up was commissioned in December 2006 using a ^{7}Li beam extracted from the ISAC source. In 2007 construction of the Penning trap was begun along with the beam-line on the TITAN platform. The first off-line beam was delivered to the Penning trap in August 2007 and the first resonance was achieved with ^{6}Li just days before the first scheduled on-line run. During this on-line run preliminary measurements of the masses of ^{8,9}Li were made. This was followed in November by a measurement of the mass of ^{8}He, using unscheduled beam obtained during testing of a new FEBIAD ion source. The measurements of ^{8,9,11}Li presented in this thesis were made in the middle of December 2007.

The RFQ beam cooler is now routinely operational on the ISAC floor and has been successfully used to cool a variety of ion beams from both on-line and off-line sources. Cooling and bunching of heavy and light ions has been demonstrated with excellent DC efficiencies. The new deceleration optics have been commissioned with beams of up to $30\,\text{keV}$ initial energy and have been proven to work effectively. However, further testing of the RFQ is still planned. An Allison type emittance meter has been built and will be used to measure the transverse emittances of the extracted ion bunches [179]. A set of attenuators has been machined and will be installed between the test ion source and the RFQ allowing for the injection and storage of very low ion currents, $I \approx 100\,\text{pA}$. With a small number of ions extracted from the RFQ, the signal induced on an MCP by each individual ion will be resolvable. Counting of these pulses will allow for measurements of the RFQ efficiency in pulsed mode. A new mode of operation for an RFQ has also recently been demonstrated whereby the injected lithium ions were stored in its lower sections. These ions were subsequently extracted and

re-accelerated back into the ISAC beam line where they were detected on an MCP. Fluorescence of these reverse-extracted, cooled ions via collinear laser spectroscopy will allow for further commissioning of the RFQ through measurements of longitudinal energy spreads as well as allowing for new studies of atomic physics.

Full systematic studies of the TITAN Penning trap are ongoing. Measurement of a range of well known masses will soon push the systematic uncertainty in online measurements below the 1×10^{-8} level. However, with the measurements presented in this thesis it has been demonstrated that high accuracy, high impact physics can already be done, only four months after the experiment came online. The advantage of carrying out such measurements at TRIUMF is also clear. The high available yields of ^{11}Li was one of the contributing factors that made this experiment possible, the shortest-lived isotope ever measured using the technique of Penning trap mass spectroscopy. This breakthrough development, the measurement of a very-short-lived isotope, now opens the door for studies on other exotic nuclei and has pushed the limits in accessible half-lives down by almost an order of magnitude. Programs to study the halo nuclei ^{6,8}He, ^{12,14}Be and ^{17,19}N are now planned for the near future. Full commissioning of TITAN including the EBIT is planned for summer of 2008 with some isotopes of calcium and potassium.

In summary the masses of the isotopes ^{8,9,11}Li have been measured to a precision of 1×10^{-7} or better using the newly commissioned TITAN Penning trap mass spectrometer. Using these new values the two-neutron separation energy of ^{11}Li has been calculated as $369.3 \pm 1.3\,\text{keV}$, the most precise measurement of this quantity to date, over 20 years after the initial discovery of ^{11}Li as a halo nucleus. Like the previous best result from the MISTRAL group the newly calculated two neutron separation energy shows more than three sigma deviation from the previously accepted atomic mass evaluation, AME2003.

Bibliography

[1] I. Tanihata *et al.*, Phys. Rev. Lett. **55**, 2676 (1985).

[2] P. G. Hansen and B. Jonson, Europhysics Letters (EPL) **4**, 409 (1987).

[3] T. Nakamura *et al.*, Physical Review Letters **96**, 252502 (2006).

[4] K. Ieki *et al.*, Phys. Rev. Lett. **70**, 730 (1993).

[5] D. Sackett *et al.*, Phys. Rev. C **48**, 118 (1993).

[6] S. Shimoura *et al.*, Physics Letters B **348**, 29 (1995).

[7] M. Zinser *et al.*, Nuclear Physics A **619**, 151 (1997).

[8] R. Sanchez *et al.*, Physical Review Letters **96**, 033002 (2006).

[9] S. C. Pieper, V. R. Pandharipande, R. B. Wiringa, and J. Carlson, Phys. Rev. C **64**, 014001 (2001).

[10] S. C. Pieper, K. Varga, and R. B. Wiringa, Phys. Rev. C **66**, 044310 (2002).

[11] K. Varga, Y. Suzuki, and I. Tanihata, Phys. Rev. C **52**, 3013 (1995).

[12] K. Varga, Y. Suzuki, and R. G. Lovas, Phys. Rev. C **66**, 041302 (2002).

[13] T. Neff, H. Feldmeier, and R. Roth, Fermi Molecular Dynamics, in *Proceeding of the 21st Winter Workshop on Nuclear Dynamics*, edited by W. Bauer, R. Bellwied, and S. Panitkin, EP Systema, 2005.

[14] M. Tomaselli *et al.*, Nuclear Physics A **690**, 298 (2001).

[15] P. Navrátil and B. R. Barrett, Phys. Rev. C **57**, 3119 (1998).

[16] P. Navrátil and W. E. Ormand, Phys. Rev. C **68**, 034305 (2003).

[17] E. Comay, I. Kelson, and A. Zidon, Atomic Data and Nuclear Data Tables **39**, 235 (1988).

[18] J. Janecke and P. J. Masson, Atomic Data and Nuclear Data Tables **39**, 265 (1988).

[19] S. Ludwig, H. von Groote, E. Hilf, A. G. W. Cameron, and J. Truran, Nuclear Physics A **203**, 627 (1973).

[20] H. Koura, M. Uno, T. Tachibana, and M. Yamada, Nuclear Physics A **674**, 47 (2000).

[21] H. Koura, M. Uno, T. Tachibana, and M. Yamada, Kuty mass formula 2005 revised version, On-line revision of previously published paper.

[22] J. Duflo and A. Zuker, Phys. Rev. C **52**, R23 (1995).

[23] X. Bai and J. Hu, Phys. Rev. C **56**, 1410 (1997).

[24] A. H. Wapstra, G. Audi, and C. Thibault, Nuclear Physics A **729**, 129 (2003).

[25] C. Bachelet *et al.*, The European Physical Journal A - Hadrons and Nuclei **25**, 31 (2005).

[26] N. Vinh Mau and J. C. Pacheco, Nuclear Physics A **607**, 163 (1996).

[27] H. Esbensen, G. F. Bertsch, and K. Hencken, Phys. Rev. C **56**, 3054 (1997).

[28] A. Cobis, D. V. Fedorov, and A. S. Jensen, Phys. Rev. C **58**, 1403 (1998).

[29] K. Ueta, H. Miyake, and G. W. Bund, Phys. Rev. C **59**, 1806 (1999).

[30] M. A. Khan, S. K. Dutta, T. K. Das, and M. K. Pal, Journal of Physics G: Nuclear and Particle Physics **24**, 1519 (1998).

[31] M. Hesse, D. Baye, and J. M. Sparenberg, Physics Letters B **455**, 1 (1999).

[32] E. Garrido, D. V. Fedorov, and A. S. Jensen, Nuclear Physics A **700**, 117 (2002).

[33] F. Barranco, P. F. Bortignon, R. A. Broglia, G. Colo, and E. Vigezzi, European Physics Journal A **11**, 385 (2001).

[34] J. C. Pacheco and N. Vinh Mau, Phys. Rev. C **65**, 044004 (2002).

[35] J. Meng and P. Ring, Phys. Rev. Lett. **77**, 3963 (1996).

[36] J. Meng, W. Paschl, and P. Ring, Zeitschrift fur Physik A Hadrons and Nuclei **358**, 123 (1997).

[37] N. Michel, W. Nazarewicz, M. Ploszajczak, and J. Rotureau, Physical Review C (Nuclear Physics) **74**, 054305 (2006).

[38] R. A. Broglia *et al.*, Nuclear field theory description of the three-body system 11li, in *International Nuclear Physics Conference INPC 2001*, edited by E. Norman, L. Schroeder, G. Wozniak, and A. M. Smith, pp. 746–750, AIP, 2002.

[39] J. C. Hardy and I. S. Towner, Physical Review C (Nuclear Physics) **71**, 055501 (2005).

[40] I. S. Towner and J. Hardy, ArXiv e-prints **710** (2007), 0710.3181.

[41] M. Brodeur, *Towards high precision mass meassurements of short-lived exotic isotopes using highly charged ions at the TITAN Penning trap system*, PhD thesis, The University of British Columbia, 2006.

[42] J. Dilling, *Direkte massenmessungen an exotischen kerne mit SHIP-TRAP und ISOLTRAP*, PhD thesis, Universitat Heidelberg, 2001.

[43] H. W. Ellis *et al.*, Atomic Data and Nuclear Data Tables **22**, 179 (1978).

[44] D. A. Dahl, International Journal of Mass Spectrometry **200**, 3 (2000).

[45] I. Tanihata *et al.*, Physics Letters B **160**, 380 (1985).

[46] R. J. Glauber, *Lectures in theoretical physics* (New York, Interscience Publishers, 1958).

[47] T. Kobayashi *et al.*, Phys. Rev. Lett. **60**, 2599 (1988).

[48] D. E. Greiner, P. J. Lindstrom, H. H. Heckman, B. Cork, and F. S. Bieser, Phys. Rev. Lett. **35**, 152 (1975).

[49] A. S. Goldhaber, Physics Letters B **53**, 306 (1974).

[50] M. V. Zhukov *et al.*, Physics Reports **231**, 151 (1993).

[51] I. Tanihata, Journal of Physics G: Nuclear and Particle Physics **22**, 157 (1996).

[52] A. S. Jensen, K. Riisager, D. V. Fedorov, and E. Garrido, Reviews of Modern Physics **76**, 215 (2004).

[53] M. J. Smith, A square-wave-driven radiofrequency quadrupole cooler and buncher for TITAN, Master's thesis, University of British Columbia, 2005.

[54] C. Thibault *et al.*, Phys. Rev. C **12**, 644 (1975).

[55] J. M. Wouters, Zeitschrift fur Physik A Hadrons and Nuclei **331**, 229 (1988).

[56] T. Kobayashi *et al.*, Spectroscopy of the exotic nucleus li-11 via pion double charge exchange reaction b-11(pi-,pi+)li-11, Prepared for International Workshop on Pions in Nuclei, Peniscola, Spain, 3-8 Jun 1991, 1991.

[57] B. M. Young *et al.*, Phys. Rev. Lett. **71**, 4124 (1993).

[58] H. Esbensen, Physical Review C **44**, 440 (1991).

[59] H. Esbensen and G. F. Bertsch, Nuclear Physics A **542**, 310 (1992).

[60] H. Esbensen, G. F. Bertsch, and C. A. Bertulani, Nuclear Physics A **581**, 107 (1995).

[61] A. Cobis, D. V. Fedorov, and A. S. Jensen, Physics Letters B **424**, 1 (1998).

[62] E. Garrido, D. V. Fedorov, and A. S. Jensen, Nuclear Physics A **708**, 277 (2002).

[63] J. M. Bang *et al.*, Physics Reports **264**, 27 (1996).

[64] I. J. Thompson *et al.*, Journal of Physics G: Nuclear and Particle Physics **24**, 1505 (1998).

[65] A. Pushkin, B. Jonson, and M. V. Zhukov, Journal of Physics G: Nuclear and Particle Physics **22**, L95 (1996).

[66] A. Bonaccorso and N. Vinh Mau, Nuclear Physics A **615**, 245 (1997).

[67] T. Myo, S. Aoyama, K. Kato, and K. Ikeda, Physics Letters B **576**, 281 (2003).

[68] Y. A. Lurie and A. M. Shirokov, Annals of Physics **312**, 284 (2004).

[69] K. Hagino and H. Sagawa, Physical Review C (Nuclear Physics) **72**, 044321 (2005).

[70] C. A. Bertulani and G. Baur, Physics Reports **163**, 299 (1988).

[71] M. S. Hussein, M. P. Pato, and C. A. Bertulani, Phys. Rev. C **44**, 2219 (1991).

[72] B. Blank *et al.*, Zeitschrift fur Physik A Hadrons and Nuclei **343**, 375 (1992).

[73] E. Arnold *et al.*, Zeitschrift fur Physik A Hadrons and Nuclei **349**, 337 (1994).

[74] Z.-C. Yan and G. W. F. Drake, Phys. Rev. A **61**, 022504 (2000).

[75] W. E. Otten, *Nuclear radii and moments of unstable nuclei* (Plenum Publishin Corporation, 1987).

[76] C. W. De Jager, H. De Vries, and C. De Vries, Atomic Data and Nuclear Data Tables **14**, 479 (1974).

[77] G. Ewald *et al.*, Physical Review Letters **93**, 113002 (2004).

[78] Z.-C. Yan and G. W. F. Drake, Phys. Rev. Lett. **91**, 113004 (2003).

[79] G. W. F. Drake, Private communication, 2006.

[80] D. Lunney, J. M. Pearson, and C. Thibault, Rev. Mod. Phys. **75**, 1021 (2003).

[81] C. F. v. Weizsacker, Zeitschrift fur Physik A Hadrons and Nuclei **96**, 431 (1935).

[82] D. R. Hartree, Proceedings of the Cambridge Philosophical Scoiety **24**, 89 (1928).

[83] D. R. Hartree, Proceedings of the Cambridge Philosophical Scoiety **24**, 111 (1928).

[84] V. Fock, Zeitschrift fur Physik A: Hadrons and Nuclei **61**, 126 (1930).

[85] S. Goriely, F. Tondeur, and J. M. Pearson, Atomic Data and Nuclear Data Tables **77**, 311 (2001).

[86] M. Samyn, S. Goriely, P. H. Heenen, J. M. Pearson, and F. Tondeur, Nuclear Physics A **700**, 142 (2002).

[87] S. Goriely, M. Samyn, P.-H. Heenen, J. M. Pearson, and F. Tondeur, Phys. Rev. C **66**, 024326 (2002).

[88] J. Dobaczewski, M. V. Stoitsov, and W. Nazarewicz, Skyrme-HFB deformed nuclear mass table, in *International Conference on Microscopic Studies of Collective Phenomena*, edited by R. Bijker, A. Frank, and R. F. Casten, pp. 51–56, AIP, 2004.

[89] G. T. Garvey and I. Kelson, Phys. Rev. Lett. **16**, 197 (1966).

[90] L. D. Faddeev, Soviet Physics JETP **12**, 1014 (1961).

[91] S. Nagy *et al.*, Physical Review Letters **96**, 163004 (2006).

[92] T. P. Heavner, S. R. Jefferts, and G. H. Dunn, Phys. Rev. A **64**, 062504 (2001).

[93] M. Kobayashi and T. Maskawa, Progress of Theoretical Physics **49**, 652 (1973).

[94] G. Savard *et al.*, Physical Review Letters **95**, 102501 (2005).

[95] T. Eronen *et al.*, Physical Review Letters **97**, 232501 (2006).

[96] K. S. Krane, *Introductory nuclear physics* (Wiley, 1987).

[97] E. Fermi, Zeitschrift fur Physik **88**, 161 (1934).

[98] G. Gamow and E. Teller, Phys. Rev. **49**, 895 (1936).

[99] D. H. Wilkinson, Journal of Physics G: Nuclear and Particle Physics **29**, 189 (2003).

[100] J. C. Hardy and I. S. Towner, Physical Review Letters **94**, 092502 (2005).

[101] W.-M. Yao *et al.*, Journal of Physics G **33**, 1+ (2006).

[102] E. F. Zganja, Acta Physica Polonica B **38**, 1179 (2007).

[103] K. Langanke, F.-K. Thielemann, and M. Wiescher, The Euroschool Lectures on Physics with Exotic Beams, Vol. I , 383 (2004).

[104] C. E. Rolfs and W. S. Rodney, *Cauldrons in the cosmos: Nuclear astrophysics* (University of Chicago Press, 2005).

[105] J. Pruet, R. D. Hoffman, S. E. Woosley, H. T. Janka, and R. Buras, The Astrophysical Journal **644**, 1028 (2006).

[106] C. Frohlich *et al.*, Physical Review Letters **96**, 142502 (2006).

[107] P. K. Ghosh, *Ion Traps* (Claredon Press, 1995).

[108] G. Graff, H. Kalinowsky, and J. Traut, Zeitschrift fur Physik A Hadrons and Nuclei **297**, 35 (1980).

[109] G. Bollen, R. B. Moore, G. Savard, and H. Stolzenberg, Journal of Applied Physics **68**, 4355 (1990).

[110] M. Konig, G. Bollen, H. J.-. Kluge, T. Otto, and J. Szerypo, International Journal of Mass Spectrometry and Ion Processes **142**, 95 (1995).

[111] L. S. Brown and G. Gabrielse, Rev. Mod. Phys. **58**, 233 (1986).

[112] H. Schnatz *et al.*, Nuclear Instruments and Methods in Physics Research Section A: Accelerators, Spectrometers, Detectors and Associated Equipment **251**, 17 (1986).

[113] Y. Penionzhkevich, Hyperfine Interactions **132**, 263 (2001).

[114] C. J. Barton *et al.*, Phys. Rev. C **67**, 034310 (2003).

[115] C. Davids *et al.*, Hyperfine Interactions **132**, 133 (2001).

[116] H. Savajols, Hyperfine Interactions **132**, 243 (2001).

[117] D. Bazin, J. A. Caggiano, B. M. Sherrill, J. Yurkon, and A. Zeller, Nuclear Instruments and Methods in Physics Research Section B: Beam Interactions with Materials and Atoms **204**, 629 (2003).

[118] D. Lunney and G. Bollen, Hyperfine Interactions **129**, 249 (2000).

[119] J. Stadlmann *et al.*, Physics Letters B **586**, 27 (2004).

[120] Y. Litvinov *et al.*, Hyperfine Interactions **132**, 281 (2001).

[121] W. Shi, M. Redshaw, and E. G. Myers, Physical Review A (Atomic, Molecular, and Optical Physics) **72**, 022510 (2005).

[122] S. Rainville, J. K. Thompson, and D. E. Pritchard, Science **303**, 334 (2004), http://www.sciencemag.org/cgi/reprint/303/5656/334.pdf.

[123] R. Van Dyck, S. Zafonte, and P. Schwinberg, Hyperfine Interactions **132**, 163 (2001).

[124] E. Kugler *et al.*, Nuclear Instruments and Methods in Physics Research Section B: Beam Interactions with Materials and Atoms **70**, 41 (1992).

[125] G. Bollen *et al.*, Nuclear Instruments and Methods in Physics Research Section A: Accelerators, Spectrometers, Detectors and Associated Equipment **368**, 675 (1996).

[126] K. Blaum *et al.*, Nuclear Instruments and Methods in Physics Research Section B: Beam Interactions with Materials and Atoms **204**, 478 (2003).

[127] A. Kellerbauer *et al.*, Physical Review C (Nuclear Physics) **76**, 045504 (2007).

[128] H. Penttila *et al.*, Nuclear Instruments and Methods in Physics Research Section B: Beam Interactions with Materials and Atoms **126**, 213 (1997).

[129] S. Rinta-Antila *et al.*, Physical Review C (Nuclear Physics) **70**, 011301 (2004).

[130] I. Bergstrom *et al.*, Nuclear Instruments and Methods in Physics Research Section A: Accelerators, Spectrometers, Detectors and Associated Equipment **487**, 618 (2002).

[131] S. Hofmann and G. Münzenberg, Rev. Mod. Phys. **72**, 733 (2000).

[132] G. Sikler *et al.*, Nuclear Instruments and Methods in Physics Research Section B: Beam Interactions with Materials and Atoms **204**, 482 (2003).

[133] M. Block *et al.*, Hyperfine Interactions **173**, 133 (2006).

[134] C. Rauth *et al.*, Physical Review Letters **100**, 012501 (2008).

[135] G. Savard *et al.*, Nuclear Physics A **626**, 353 (1997).

[136] J. A. Clark *et al.*, Physical Review Letters **92**, 192501 (2004).

[137] G. Bollen and S. Schwarz, Journal of Physics B: Atomic, Molecular and Optical Physics **36**, 941 (2003).

[138] D. J. Morrissey, B. M. Sherrill, M. Steiner, A. Stolz, and I. Wiedenhoever, Nuclear Instruments and Methods in Physics Research Section B: Beam Interactions with Materials and Atoms **204**, 90 (2003).

[139] R. Ringle *et al.*, Physical Review C (Nuclear Physics) **75**, 055503 (2007).

[140] G. Bollen *et al.*, Physical Review Letters **96**, 152501 (2006).

[141] P. Schury *et al.*, Physical Review C (Nuclear Physics) **75**, 055801 (2007).

[142] P. Delheij *et al.*, Hyperfine Interactions **173**, 123 (2006).

[143] G. Bollen, Nuclear Physics A **693**, 3 (2001).

[144] M. Froese *et al.*, Hyperfine Interactions **173**, 85 (2006).

[145] J. A. Richards, R. M. Huey, and J. Hiller, International Journal or Mass Spectrometry and Ion Physics **12**, 317 (1973).

[146] P. H. Dawson, *Quadrupole mass spectrometry and its applications* (Springer, 1995).

[147] J. V. Vaz, *Precision mass measurements of some isotopes of platinum*, PhD thesis, The University of Manitoba, 2002.

[148] M. Sudakov and E. Nikolaev, European Journal of Mass Spectrometry **8**, 191 (2002).

[149] L. Ding, M. Sudakov, F. L. Brancia, R. Giles, and S. Kumashiro, Journal of Mass Spectrometry **39**, 471 (2004).

[150] L. Ding, M. Sudakov, and S. Kumashiro, International Journal of Mass Spectrometry **221**, 117 (2002).

[151] M. J. Barnes and G. D. Wait, Pulsed Power Conference, 2003. Digest of Technical Papers. PPC-2003. 14th IEEE International **2**, 1407 (15-18 June 2003).

[152] E. D. Courant and H. S. Snyder, Annals of Physics **3**, 1 (1958).

[153] E. Meissner, Schweizer Bauzeitung **72**, 9598 (1918).

[154] G. Floquet, Annales Scientifiques de l'École Normale Supérieure **12**, 47 (1883).

[155] L. A. Pipes, Journal of Applied Physics **24**, 902 (1953).

[156] R. B. Moore, O. Gianfrancesco, R. Lumbo, and S. Schwarz, International Journal of Mass Spectrometry **251**, 190 (2006).

[157] T. Kim, *Buffer gas cooling of ions in a radiofrequency quadrupole ion guide*, PhD thesis, McGill University, 1997.

[158] E. W. McDaniel and E. A. Mason, *The mobility and diffusion of ions in gases* (John Wiley and Sons, 1973).

[159] F. Herfurth *et al.*, Nuclear Instruments and Methods in Physics Research Section A: Accelerators, Spectrometers, Detectors and Associated Equipment **469**, 254 (2001).

[160] A. Nieminen *et al.*, Nuclear Instruments and Methods in Physics Research Section A: Accelerators, Spectrometers, Detectors and Associated Equipment **469**, 244 (2001).

[161] H. Wolnik, *Optics of charged particles* (Academic Press Inc., 1987).

[162] S. Humphries, *Charged particle beams* (John Wiley and Sons, 1990).

[163] J. P. Blewett and E. J. Jones, Phys. Rev. **50**, 464 (1936).

[164] J. Baartman, R.; Welz, Particle Accelerator Conference, 1997. Proceedings of the 1997 **3**, 2778 (12-16 May 1997).

[165] O. Hadary, M. Barnes, and G. Wait, TRIUMF Report No. TRI-DN-04-26, 2004 (unpublished).

[166] J. L. Wiza, Nuclear Instruments and Methods **162**, 587 (1979).

[167] D. Rodriguez *et al.*, Nuclear Instruments and Methods in Physics Research Section A: Accelerators, Spectrometers, Detectors and Associated Equipment **565**, 876 (2006).

[168] R. Ringle, *High-precision mass measurement of ^{38}Ca and development of the lebit 9.4-T Penning trap system*, PhD thesis, Michigan State University, 2006.

[169] R. Ringle *et al.*, International Journal of Mass Spectrometry **263**, 38 (2007).

[170] D. R. Lide, editor, *Handbook of Chemistry and Physics*, 88th ed. (Taylor and Francis, 2007).

[171] P. W. Anderson, Phys. Rev. Lett. **9**, 309 (1962).

[172] P. W. Anderson and Y. B. Kim, Rev. Mod. Phys. **36**, 39 (1964).

[173] R. S. Van Dyck, D. L. Farnham, and P. B. Schwinberg, Journal of Modern Optics **39**, 243 (1992).

[174] V. Ryjkov, *Private Communication*, 2007.

[175] M. Brodeur, *Private Communication*, 2007.

[176] G. Bollen *et al.*, Phys. Rev. C **46**, R2140 (1992).

[177] A. Kellerbauer *et al.*, The European Physical Journal D **22**, 53 (2003).

[178] R. T. Birge, Phys. Rev. **40**, 207 (1932).

[179] P. W. Allison, J. D. Sherman, and D. B. Holtkamp, IEEE Transcripts Nuclear Science **NS-30**, 2204 (1983).

[180] R. C. Tolman, *The principles of statistical mechanics* (Oxford University Press, 1967).

[181] J. D. Lawson, *The physics of charged particle beams* (Clarendon Press, 1977).

[182] M. Dombsky, P. Bricault, T. Hodges, A. Hurst, and P. Schmor, Nuclear Physics A **701**, 486 (2002).

[183] P. Bricault, K. Jayamanna, D. H. L. Yuan, M. Olivo, and P. Schmor, Recent results with the 2.45 GhZ ECRIS at TRIUMF-ISAC, in *16th International Workshop on ECR Ion Sources ECRIS'04*, edited by M. Leitner, pp. 143–146, AIP, 2005.

Appendix A

Emittance and acceptance

A.1 The Concept of Emittance

The quality of an ion beam is best described using the concept of emittance. The ideal ion beam is a group of identical particles all travelling with the same velocity, i.e. in a common direction of motion. However, in reality such an ideal beam is not achievable. Instead the ions will have a small spread in energy, (for on-line facilities typically 1 to $100\,\mathrm{eV}$) which is characteristic of the ion production and acceleration method, as well as having small angular divergences (typically 1 to $100\,\mathrm{mrad}$) from the common direction of motion.

In order to quantify how the properties of a beam differ from the ideal case we can define three emittances as the areas that the beam occupies in momentum-position phase space with respect to three cartesian coordinate axes. The ideal beam has zero emittance. The larger the emittance of the beam the further it deviates from the ideal case. If we define the z- axis as the common direction of motion of our beam it is usual to denote the area occupied in the (x, p_x) and the (y, p_y) phase spaces as the transverse emittances and the area in the (z, p_z) phase space as the longitudinal emittance. Using the small angle approximation it is easy to show that the transverse velocities of the ions are proportional to their angular divergences. Hence, it is common to give transverse emittances as the area occupied in the (x, θ_x) and (y, θ_y) spaces in units of $\pi \cdot \mathrm{mm} \cdot \mathrm{mrad}$. It is also common practice to give the longitudinal emittance as the area of the beam in energy-time phase space, in units of $\mathrm{eV} \cdot \mu\mathrm{s}$.

An ion beam can be considered to be a cloud of point-like particles in six dimensional phase space, (x, y, z, p_x, p_y, p_z), with each of the individual particles following its own unique temporal evolution. According to Liouville's theorem, the volume of such a cloud will remain constant as a function of time under the application of conservative forces even though the shape of the cloud will, in general, change [180]. If, as is generally the case, the forces acting in the x-, y- and z- directions are independent of each other then the areas of the three individual sub-spaces, (x, p_x), (y, p_y) and (z, p_z), must also be conserved even though the shape of their boundaries can change

with time. Therefore according to Liouville's theorem the three emittances of an ion beam are constant under the application of conservative forces.

A.2 The Concept of Acceptance

When designing electromagnetic devices to transport, manipulate and analyze ion beams, it is important to ensure that the devices make efficient use of the beam. This is even more so when operating with radioactive nuclei where production methods are fairly cumbersome and often only small production yields can be achieved.

Consider the simple example of a narrow drift tube; if the beam entering the tube is too wide the edges of the beam will be lost (see figure A.1a) and if the beam entering the tube is too divergent then it will hit the walls (see figure A.1b). From this simple example we can see that the tube has an acceptance profile in position-momentum phase space, in order for the beam to be transported through the tube without losses it is necessary for the transverse emittance of the beam to overlap completely with this acceptance profile.

Figure A.1: (a) A wide parallel beam enters a narrow tube. A large proportion of the beam is lost. (b) A narrow diverging beam enters a narrow tube. Again a large proportion of the beam is lost.

Consider the example of an electrostatic barrier with an ion beam incident on it. If the height of the barrier is set equal to the mean kinetic energy of the incoming beam then all the ions with kinetic energies less than the mean will be stopped whereas ions with kinetic energies greater than the mean can pass the barrier. Now, consider a voltage supply used to bias the potential barrier with an inherent ripple such that the barrier height oscillates between a value slightly less than the lowest energy of the beam and a value slightly higher than the highest energy of the beam, in this case the number of ions passing the barrier will oscillate as a function of time (see

figure A.2). This system has an acceptance in energy-time phase space and again for a beam to pass through the system without losses its longitudinal emittance must completely overlap with this acceptance.
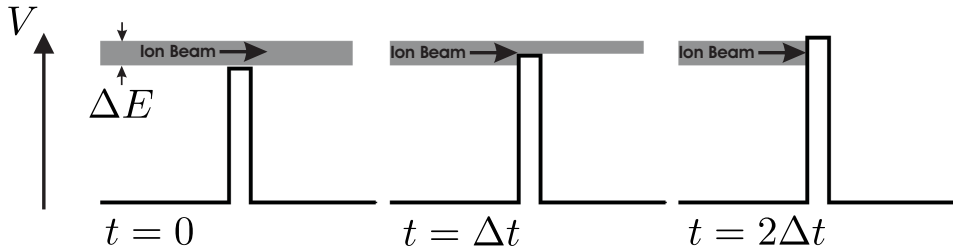

Figure A.2: A beam with energy spread ΔE impinges on a electrodynamic barrier. At time $t = 0$ all the beam passes above the barrier whereas at time $t = 2\,\Delta t$ the whole beam is stopped.

In general, we conclude that all physical systems have an acceptance in six dimensional phase space. Efficient transport of an ion beam through a system relies on the matching of the beam emittance to the system's acceptance. If the beam's volume in phase space completely overlaps with the system's acceptance then the beam will be transported without loss.

A.3   Mathematical Description of Emittance

The definition of emittance presented here is that typically used for lower energy non-relativistic beams. This definition is not normalised, meaning that direct comparisons between the emittances of beams with different energies should not be made. For a good overview of the material presented see [181].

In practice the best ion beams achievable are produced with Gaussian profiles in both position and velocity. This means that the distribution of particles in position-momentum space can be described by a two dimensional Gaussian with the rms emittance defined as the area, A, of the ellipse bounding the distribution at one standard deviation divided by π (see figure A.3):

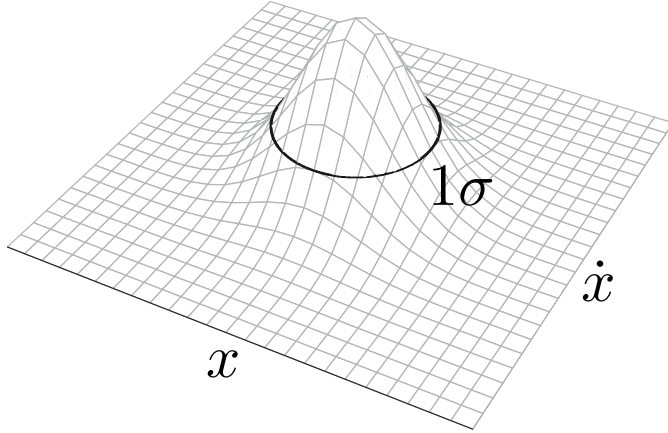$$\varepsilon_{rms} = \frac{A}{\pi},\tag{A.1}$$

Figure A.3: The rms emittance is defined as the area of the ellipse bounding the normal distribution at one standard deviation divided by π.

Such an ellipse is typically defined using the Twiss parametrization where:

$$\varepsilon_{rms} = \gamma x^2 + 2\alpha x \dot{x} + \beta \dot{x}^2, \tag{A.2}$$

and:

$$x_{max} = \sqrt{\varepsilon_{rms}\beta}, \tag{A.3}$$

$$\dot{x}_{max} = \sqrt{\varepsilon_{rms}\gamma}, \tag{A.4}$$

$$x' = \alpha(\varepsilon_{rms}/\gamma)^{\frac{1}{2}}, \tag{A.5}$$

$$\dot{x}' = \alpha(\varepsilon_{rms}/\beta)^{\frac{1}{2}}, \tag{A.6}$$

$$\beta\gamma - \alpha^2 = 1, \tag{A.7}$$

where x_{max}, $\dot{x}_{max}$, x' and $\dot{x}'$ are defined as shown in figure A.4).

The sigma matrix is also another common representation of the emittance where:

$$\sigma = \varepsilon_{rms} \begin{pmatrix} \beta & -\alpha \\ -\alpha & \gamma \end{pmatrix} = \begin{pmatrix} \sigma_{11} & \sigma_{12} \\ \sigma_{12} & \sigma_{22} \end{pmatrix}, \tag{A.8}$$

$$\sigma_{11} = x_{max}^2, \tag{A.9}$$

$$\sigma_{22} = \dot{x}_{max}^2. \tag{A.10}$$

The emittance is given by:

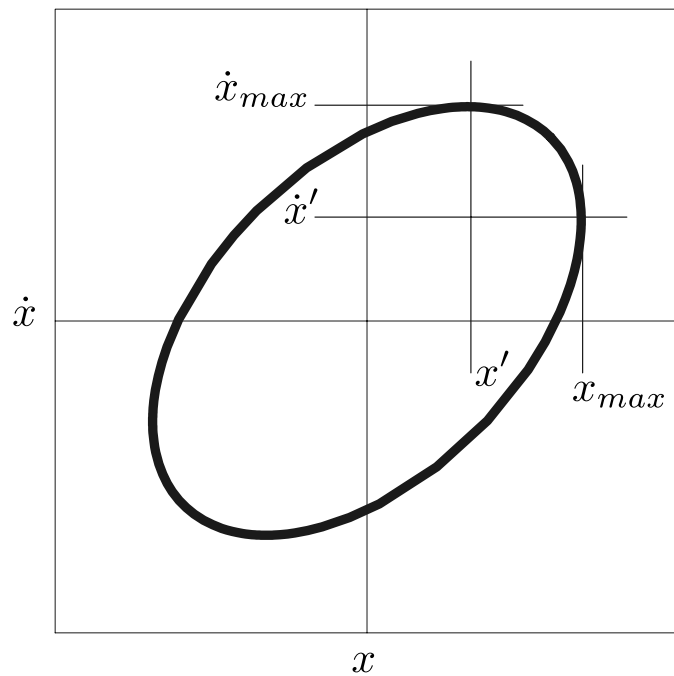$$\varepsilon_{rms} = \sqrt{|\sigma|} = \sqrt{\sigma_{11}\sigma_{22} - \sigma_{12}^2}. \tag{A.11}$$

Figure A.4: The Twiss parameters of an ellipse can be related to the points shown (see equations A.3, A.4, A.5 and A.6).

In the field of optics lenses, prisms and mirrors are used to control the passage of light through a system. In ion optics electromagnetic fields are used to control the passage of charged particles through a system. In analogy to the well know matrix method in optics it is possible to define a transfer matrix, $\boldsymbol{M}$, for a system of ion optics such that:

$$\begin{pmatrix} x \\ \dot{x} \end{pmatrix}' = \boldsymbol{M} \begin{pmatrix} x \\ \dot{x} \end{pmatrix} = \begin{pmatrix} m_{11} & m_{12} \\ m_{21} & m_{22} \end{pmatrix} \begin{pmatrix} x \\ \dot{x} \end{pmatrix}. \tag{A.12}$$

If the transfer matrix for a system is know the transformation of the beams sigma matrix as it passes through the system can be calculated as:

$$\sigma' = \boldsymbol{M}\sigma\boldsymbol{M}^T \tag{A.13}$$

where $\boldsymbol{M}^T$ is the transpose of the matrix $\boldsymbol{M}$. Expansion of this product leads to the useful relationship:

$$\sigma'_{11} = m_{11}^2\sigma_{11} + 2m_{11}m_{12}\sigma_{12} + m_{12}^2\sigma_{22}, \tag{A.14}$$

which relates the three parameters of the sigma matrix before an optical element to a single element after the element. Hence, measurement of the beam width as a function of voltage applied on an optical element can be used to calculate the emittance of a beam as long as the transfer matrix is known.

The Gaussian density distribution of the beam in position-momentum phase space can be expressed in terms of the sigma matrix coefficients as:

$$\rho(x,\dot{x}) = \frac{1}{2}\pi\varepsilon_{rms}\exp[-\frac{1}{2}\vec{x}^T\sigma^{-1}\vec{x}], \tag{A.15}$$

where:

$$\vec{x} = \begin{pmatrix} x \\ \dot{x} \end{pmatrix}. \tag{A.16}$$

Hence, if the density distribution of the particles is measured, the emittance can be found by fitting a Gaussian to it. Alternatively the emittance can be calculated using the relationship:

$$\varepsilon_{rms} = \sqrt{\langle x^2\rangle\langle \dot{x}^2\rangle - \langle x\dot{x}\rangle^2}, \tag{A.17}$$

where the angle brackets, $\langle\rangle$, denote the average of the values over the two dimensional phase space.

The rms emittance of a beam encompasses around 39% of its ions. Different definitions of emittance in common use give the area in phase space

$\varepsilon/\varepsilon_{rms}$	1/4	1	4	6	9
Percentage of particles enclosed	15	39	87	95	99

Table A.1: Scaling factors to convert rms emittance into other commonly used forms.

containing other percentages of the beam. For a Gaussian beam the rms emittance can be easily converted to the emittance containing any percentage of the beam by multiplication of a scaling factor. Some typical scaling factors are given in table A.1.

Appendix B

The ISAC Facility at TRIUMF

The ISAC (Isotope Separator and ACcelerator) facility produces radioactive ions for use in a variety of different experiments using the ISOL (Isotope Separator On Line) method [182]. The proton beam produced by the TRIUMF (TRI-University Meson Facility) cyclotron ($I \leq 100\,\mu\text{A}$, $E = 500\,\text{MeV}$) impinges on a solid target. At these energies nuclear reactions such as spallation and fragmentation take place and radioactive species are produced. These nuclei diffuse out of the target, are ionised, and are subsequently electrostatically accelerated to an energy between 12 and $60\,\text{keV}$. A two stage magnetic dipole separator is then used to select ions with a specific charge-to-mass ratio which are delivered to the experimental area.

The ISAC facility uses a number of different targets in order to provide a large variety of different species of radioactive ions. The facility is designed to deliver beams with $A \leq 235$ to the low energy, $E \leq 60\,\text{keV}$, experimental area. Further acceleration of the beam is achieved using a $35.4\,\text{MHz}$ RFQ linear accelerator which can accelerate beams with $A/q \leq 30$ from an energy of $2\,\text{keV}/u$ to $153\,\text{keV}/u$ and an addition $106\,\text{MHz}$ variable energy Drift Tube Linac (DTL) which can accelerate beams with $3 \leq A/q \leq 6$ to energies of $1.8\,\text{MeV}/u$. The TITAN experiment is installed in the low energy experimental area.

The TRIUMF cyclotron produces a continuous proton beam, hence the ion-beam produced at ISAC is also continuous. The emittance of the beam depends on the method of ionisation. At the present time most ISAC beams are created using a surface ion source whereby atoms with a low ionisation potential are converted into singly charged ions on contact with a metal surface of high work function. This method results in fairly low emittance beams, $\epsilon_{99\%} \approx 10\,\pi\,\text{mm}\,\text{mrad}$ at $40\,\text{keV}$, with a longitudinal energy spread on the order of a few electron-volts. However, for ions with higher ionisation potentials other methods must be used. Two methods are currently under development using laser and plasma ion sources.

Laser ionisation produces ion beams with properties comparable to sur-

face ionisation. Further, because the laser used is tuned exactly to the energy of the first ionisation potential of the species of interest a beam that is isotopically very pure is produced. This method has the disadvantage that a new laser scheme must be developed for ionisation of every species of interest.

There are two types of plasma ion source Forced Electron Beam Ion Arc Discharge (FEBIAD) and Electron Cyclotron Resonance (ECR). In a FEBIAD gaseous atoms are loaded into a chamber whereby ionisation occurs via collisions with a electrons produced with a hot filament. This kind of source produces beams with longitudinal energy spreads comparable to surface ion sources with transverse emittances on the order of $\epsilon_{99\%} \approx 20\,\pi\,\mathrm{mm}\,\mathrm{mrad}$ at $40\,\mathrm{keV}$. In an ECR source ionisation also occurs via collisions with an electron beam. However, the beam is caused to oscillate through the atomic gas by the application of a resonant microwave field. The advantage of this method is that the electrons can be accelerated to very high energies by the microwave field and hence highly charged ions can be produced. Recent tests of the ECR source at TRIUMF showed it produced beams with transverse emittances from $20\,\mathrm{to}\,50\,\pi\,\mathrm{mm}\,\mathrm{mrad}$ at $40\,\mathrm{keV}$ [183].